Tunability of Vertical-Cavity Surface-Emitting Lasers Using Liquid Crystal

Afstembaarheid van oppervlakte-emitterende lasers met vloeibaar kristal

Yi Xie

Promotoren: prof. dr. ir. J. Beeckman, prof. dr. ir. K. Neyts
Proefschrift ingediend tot het behalen van de graad van
Doctor in de Ingenieurswetenschappen: Elektrotechniek

Vakgroep Elektronica en Informatiesystemen
Voorzitter: prof. dr. ir. R. Van de Walle
Faculteit Ingenieurswetenschappen en Architectuur
Academiejaar 2014 - 2015

UNIVERSITEIT
GENT

ISBN 978-90-8578-762-4
NUR 959, 926
Wettelijk depot: D/2015/10.500/6

Promotors:

prof. Jeroen Beeckman	Ghent University, ELIS
prof. Kristiaan Neyts	Ghent University, ELIS

Examination committee:

prof. Jeroen Beeckman	Ghent University, ELIS
prof. Kristiaan Neyts	Ghent University, ELIS
prof. Krassimir Panajotov	Free University Brussels, Applied Physics and Photonics
prof. Geert Morthier	Ghent University, INTEC
prof. Christophe Levallois	Université Européenne de Bretagne
prof. Geert Van Steenberge	Ghent University, ELIS
prof. Patrick De Visschere	Ghent University, ELIS

Universiteit Gent
Faculteit ingenieurswetenschappen en Architectuur
vakgroep Elektronica en Informatiesystemen (ELIS)
Sint-Pietersnieuwstraat 41
B-9000 Gent
België
T: +32 (0)92 64 89 51
F: +32 (0)92 64 35 94

This work was supported in part by the IAP Project Photonics@be funded by the Belgian Science Policy and in part by the FWO Project under Grant G.0656.09N.

Acknowledgements

First of all, I would like to thank my promoter, Prof. Jeroen Beeckman. I still clearly remember your phone call to me before I came to our group. I was impressed by your honest and warm which attract me to work here. Your excellent scientific ideas and solid physics background inspired me and further raised my interests of my research topic. From the beginning, I have settled my goal to pursue your outstanding achievement in your PhD in the next four years. This provides me the motivation and active force to succeed.

As well, I want to thank my promoter, Prof. Kristiaan Neyts. I cannot complete my PhD work smoothly without your brilliant guide in my research. There is a saying for teachers or coaches in Chinese: "一日为师，终身为父", which means that the teacher is respectable as the father of the student. Indeed, you like my father who let me learn not only how to do research but also how to behave. It is just like another word in Chinese "严师出高徒", your broad knowledge and more importantly your strict scientific attitude help me a lot!

Because my PhD research topic is a collaborated project, I appreciate the help from Prof. Krassimir Panajotov in Department of Applied Physics and Photonics in Vrije Universiteit Brussel. He is a famous expert in laser physics. I learn much theoretical knowledge from our discussions.

I really enjoy joining in the Liquid Crystals and Photonics group, which has a wonderful intercultural environment and interdisciplinary collaboration. All my colleagues are very friendly and feel like a big family. I got much help in academic work from them. Especially I want to thank Dr. Wouter Woestenborghs, Dr. Lieven Penninck and ir. John George. Wouter helps me a lot in the experimental setup to fabricate VCSEL cells and the Labview programming. Lieven introduces me the Matlab programs to simulate the

VCSEL device performance. John assists me to evaporate thin films structure on glass substrates. Besides, I would like to thank other members or ex-members in 'Fyselek': Patrick, Alex, Marc, Filip B., Filip S., Samira, Peter, Koen, Wout, Saso, Tom, Michiel, Toon, Oliver, Glenn, Mohammad, Masoumeh, Inge, Stijn, Caspar, Aimi, Manoj, Oksana, Serena, Varsenik, Frédérique and Pavlo.

During my PhD work, my research has been supported and awarded by both Belgian research agencies and Chinese government. The research is financially supported in part by the IAP project Photonics@be funded by the Belgian Science Policy, and in part by the Research Foundation - Flanders (FWO). I also received the grant awarded by FWO to participate the international conference SPIE Optics and Photonics held in San Diego, US in 2014. As the highest honor for Chinese students abroad, I win the 2013 Chinese Government Award for Outstanding Self-financed Students Abroad awarded by China Scholarship Council (CSC).

It is the eighth year after my coming to Belgium. Although many difficulties in my study abroad, I think I am very lucky. On one hand, I got strong support from my promoters and colleagues in research, and my results have been recognized by my country. On the other hand, I met my wife Yuanbo Feng in Belgium and have my first son Bowen born in Leuven. I got real happiness from them. Most unforgettable is that my parents came to Belgium to help us out for three times. Therefore, I have to thank my parents, my wife and all the persons who gave me support and help before!

Yi Xie

Ghent, 21 November 2014

Table of contents

Samenvatting

Vertical Cavity Surface Emitting Lasers (VCSELs) worden gebruikt als lichtbron in opto-elektronische componenten voor toepassingen zoals optische interconnecties en sensoren. In vergelijking met andere lasertypes hebben VCSELs enkele belangrijke voordelen. Aangezien ze licht uitzenden loodrecht op het substraat kunnen meerdere lasers geïntegreerd worden op één chip. Commerciële VCSELs zijn bovendien beschikbaar met grote bandbreedtes van meer dan 10 GHz. Ook zijn deze lasers vrij efficiënt in de omzetting van elektrisch vermogen naar optisch vermogen, hebben ze een lage drempel voor lasing (minder dan 1 milliampère) en zijn ze relatief goedkoop (de lasers in dit werk zijn commercieel beschikbaar voor ongeveer 2 euro per stuk). Aangezien de meeste VCSELs een vrij mooi circulair emissieprofiel vertonen kan een hoge efficiëntie bereikt worden in de koppeling met optische vezels. Deze voordelen maken van VCSELs een goede kandidaat voor toepassingen naast optische communicatie en sensoren, zoals laser printers, computer muizen biologische analyse en atoomklokken op chipniveau. De mogelijkheid om de polarisatietoestand en de emissiegolflente af te stemmen zou een aantal interessante extra mogelijkheid bieden. Vloeibare kristallen zijn optische materialen met anisotrope optische eigenschappen en worden vandaag de dag massaal gebruikt in beeldschermen. Dit materiaal zal in dit werk gebruikt worden om de emissie-eigenschappen af te stemmen van VCSELs.

Het doel van dit werk is het ontwikkelen van een elektrisch aangestuurde VCSEL met een vloeibaarkristallaag in nauw contact met het gebied waar het licht geëmitteerd wordt. Door het incorporeren van een vloeibaarkristallaag kunnen verschillende functies gerealiseerd worden: de polarisatietoestand, bundelprofiel, lasingdrempel en golflengte kunnen ofwel thermisch ofwel elektrisch gecontroleerd worden.

Algemeen kunnen er in dit werk vier verschillende types cellen onderscheiden worden. De eerste generatie wordt voorgesteld in Hoofdstuk 3 en is in feite enkel bedoeld om aan te tonen dat de technologie om een VCSEL te combineren met een vloeibaarkristallaag werkt. Het moeilijkste onderdeel van de fabricage is vooral het microscopisch positioneren van de laser chip op de substraten. De mechanische manipulaties hiervoor moeten precies gecontroleerd worden en een strikte procedure moet gevolgd worden. De resulterende elektrisch aangedreven VCSEL is bedekt met een laagje dun nematisch vloeibaar kristal dat apart kan elektrisch aangestuurd worden. Het vloeibaar kristal is gealigneerd met foto-aligneringsmateriaal. De lasereigenschappen van de VCSEL worden in dit geval niet fundamenteel veranderd omdat het vloeibaar kristal geen terugkoppeling biedt naar de VCSEL caviteit, behalve enkele zeer kleine reflecties aan de randoppervlakken. Maar de vloeibaarkristallaag biedt wel de mogelijkheid om de polarisatietoestand van het laserlicht te veranderen door het aanleggen van een elektrische spanning over the laag.

De ontwikkelde technologie wordt in de rest van het werk gebruikt voor cellen waarbij er wel een belangrijke terugkoppeling is naar de lasercaviteit. Hiermee kunnen ook andere parameters dan de polarisatie worden beïnvloed. De optische terugkoppeling wordt gerealiseerd door het gebruik van chirale vloeibare kristallen of door vloeibare kristallen met een extra reflector. In Hoofdstuk 4 worden VCSELs gedemonstreerd met chirale vloeibare kristallen als reflector. Het chirale vloeibaar kristal biedt een polarisatieselectieve optische terugkoppeling naar de VCSEL omdat enkel één bepaalde circulaire polarisatie sterk wordt gereflecteerd, terwijl de andere niet wordt gereflecteerd. Er wordt aangetoond dat de polarisatie van het licht vrijwel circulair gepolariseerd is met een mate van circulaire polarisatie die veel hoger ligt dan de mate van lineaire polarisatie bij een VCSEL zonder vloeibaar kristal. Bovendien is de laserdrempel lager en kan de golflengte thermisch veranderd worden met een grotere helling.

In het vierde hoofdstuk hebben de VCSEL cellen een externe caviteit die gevormd wordt op basis van niet-chiraal vloeibaar kristal met daarbij een metallische of dielektrische reflector (gebaseerd op periodieke lagen van SiO_2/Ta_2O_5). De golflengte van de reflectieband bij de dielektrische reflector wordt bepaald door de dikte van de lagen en de dikte wordt zo aangepast dat de golflengte van de VCSEL emissie in de reflectieband ligt. Deze reflector biedt een sterke optische terugkoppeling ongeacht de polarisatie van het licht. De lengte van de externe caviteit kan veranderd worden door de temperatuur aan te passen en de verandering gebeurt doordat mechanische

spanningen in de structuur veranderen in functie van temperatuur. De polarisatietoestand, transversaal modeprofiel en golflengte kunnen veranderd worden door de lengte van de caviteit en dus door de temperatuur.

Hoofdstuk 6 behandelt VCSEL cellen met een externe caviteit zoals in Hoofdstuk 5, maar nu met vloeibare kristallen. Door de elektrisch spanning te veranderen over de vloeibaarkristallaag wordt de optische lengte van de caviteit veranderd. Zo worden de emissie-eigenschappen van de VCSEL ook aangepast. In dit geval zien we het schakelen van de polarisatie tussen twee lineaire polarisatietoestanden met sub-milliseconde schakeltijden.

De experimentele resultaten in dit werk worden ook vergeleken met theoretische berekeningen om zo de fysische aspecten achter de verschillende experimenten te begrijpen. Hiervoor worden de optische eigenschappen van de VCSELs gesimuleerd met een Matlab programma, gebaseerd op de vlakke golf expansiemethode. Voor een bepaalde golflengte wordt de laserdrempel berekend door de optische versterking van de materialen in het actieve gebied van de laser aan te passen zodat de ‘roundtrip gain’ gelijk wordt aan één. De berekening wordt gedaan voor een reeks golflengten en de uiteindelijke lasergolflengte is degene met de laagste drempel. Voor deze drempel kan dan ook het elektrisch veld worden berekend in elke laag langs de richting van emissie. Ook kan de polarisatietoestand van het ligt dat propageert in beide richtingen berekend worden. De simulatieresultaten komen goed overeen met de experimentele resultaten.

Summary

Vertical Cavity Surface Emitting Lasers (VCSELs) have been used as light sources in optoelectronic devices in the past decade in optical interconnects and sensing applications. There are many advantages of VCSELs compared to other types of lasers. They can be integrated into two dimensional arrays and they achieve a high modulation bandwidth of more than 10 GHz. Additionally, they operate with high efficiency of light-emission, low lasing threshold (less than 1 milli ampere) and are relatively cheap (the lasers in this work are commercially available for about 2 euro per piece). Good coupling to optical fibers can be achieved due to the high quality circular spatial emission profile. These advantages make VCSELs a good candidate for broad industrial applications, not only in optical communication and sensing, but also in laser printers, computer mouse, biological analysis and chip scale atomic clocks. The ability to modify the polarization state and tune the emission wavelength could be additional interesting features of VCSELs. Liquid crystal (LC) is an interesting optical material with anisotropic refractive index and it is nowadays used in most of the flat panel displays. This material can be used to tune the emission from VCSELs.

The aim of this work is to develop an electrically driven integrated VCSEL device with an LC layer close to the emission region. By incorporating such a LC layer with a VCSEL, multiple functions can be realized: the polarization state, beam profile, threshold and wavelength can be controlled either thermally or electrically.

The devices in this thesis can be classified into four different types. The first generation is introduced in Chapter 3 and it is meant as a proof that the developed technology for integrating LC onto a VCSEL device works. The most important part in the fabrication is the microscopic positioning of the laser chip inside the device. All the mechanical manipulations in the

fabrication need to be precisely controlled and a tight production procedure needs to be followed. The resulting electrically driven VCSEL is covered with a thin nematic LC layer that can be driven separately. The LC is aligned by photo-alignment. The lasing properties of the VCSEL are not fundamentally changed because the LC layer introduces only minor reflections and no external feedback is provided to the laser cavity. The LC layer affects strongly the polarization state of the VCSEL emission due to its birefringent properties. It is observed that the polarization state of the laser emission can be controlled by the applied voltage. This technology provides a platform for the rest of the work in this PhD.

Based on this technology, other devices are realized with different functionalities. The basic idea is that the LC layers introduce optical feedback to the VCSEL cavity. The optical feedback is realized by either chiral liquid crystals (CLCs) or nematic LCs incorporated with an extra reflector. In chapter 4, VCSELs with CLCs as an external cavity will be demonstrated. CLC is provides polarization selective optical feedback to the VCSEL, because one circular polarization mode with the same handedness of the CLC helix is effectively reflected due to the photonic band structure of CLC. It is shown that the polarization of the emission is almost purely circularly polarized and the polarization purity is much better than the degree of linear polarization of the stand-alone VCSEL. Additionally the threshold is further decreased and the wavelength can be thermally tuned with larger slope efficiency.

The third generation of the VCSEL device has an external cavity that is formed by an extra reflector, based on a metallic or a dielectric layer (consisting of periodic bi-layers of SiO_2/Ta_2O_5), which can provide optical feedback for all types of polarization. The reflection band position of the dielectric layers is determined by the refractive index of the materials and the thickness of the layers. In order to make effective optical feedback, this band gap is suitably designed so that the emission wavelength of the VCSEL is located inside the band. This is the subject of Chapter 5. The external cavity length can be changed by temperature due to the thermal expansion of the whole mechanical structure. The emission properties, including polarization state, transverse mode and longitudinal mode, can be tuned by changing the external cavity length. Therefore, the emission of the device is thermally tunable.

The last type of LC-VCSEL device includes nematic LCs incorporated with a dielectric reflector. This is described in Chapter 6. By changing the voltage across the LC layer, the optical length in the external cavity can be tuned.

Therefore, the emitting properties of the LC-VCSEL can be controlled by the voltage applied on the LC layer. Stable and reproducible polarization switching between two orthogonal linear polarization states is realized with sub-millisecond switching times.

The experimental results in this thesis are compared to theoretical simulations, in order to understand the physics behind the observed effects. For this purpose, the optical properties of the LC-VCSEL system are simulated using a Matlab program based on the plane wave expansion method. For a certain wavelength, the lasing threshold is calculated by increasing the optical gain of the active region until the roundtrip gain reaches one. This calculation is performed for a range of wavelengths and the lasing wavelength is found as the one that corresponds to the lowest threshold. For this threshold gain, the electric field vectors (either the moving field or the total field) in each layer along the emission direction can be calculated. Consequently, the polarization state of the light propagating in both directions (forwards or backwards) can be derived. The simulation results match well with the experimental results.

List of figures

List of tables

List of symbols and abbreviations

Symbols

α	Azimuth angle of quarter wave plate
φ	Azimuth angle of linear polarizer
P	Optical power
I_{VCSEL}	Operating current of VCSEL
S	Stokes parameter
p	Degree of polarization
T_x	Transmission in x direction
T_y	Transmission in y direction
θ	Radius incident angle
Φ	Polar incident angle
n_o	Ordinary refractive index
n_e	Extraordinary refractive index
Im{n}	Imaginary part of refractive index in the active layer
G_{th}	Threshold gain
λ	Wavelength
λ_{res}	Resonance wavelength
Γ	Confinement factor
E_x	Electric field component in x direction
E_y	Electric field component in y direction
Φ_x-Φ_y	Phase difference between E_x and E_y
I	Optical intensity

k	Wave number
$\boldsymbol{k}$	Wave vector
κ	Propagation constant
p	Pitch of chiral liquid crystal
z	Propagation distance
d	Thickness of liquid crystal layer
V_{LC}	Voltage applied across liquid crystal layer

Abbreviations

CLC	Chiral Liquid Crystal
CP	Circular Polarization
CW	Continuous Wave
DBR	Diffractive Bragg Reflector
DE	Dielectric reflector
FWHM	Full Width at Half Maximum
ITO	Indium Tin Oxide
IR	Infra-Red
LC	Liquid Crystal
LCP	Left-handed Circular Polarization
LED	Light Emitting Diode
LH	Left-handed Helix
LLS	Linear Least Squares
LM	Longitudinal Mode
LP	Linear Polarization
MM	Multi Mode
NLC	Nematic Liquid Crystal
PA	Photo Alignment
PBG	Photonics Band Gap
PWE	Plane Wave Expansion
QW	Quantum Well
RCP	Right-handed Circular Polarization
RH	Right-handed Helix
SL	Semiconductor Laser
SM	Single Mode
TC	Threshold Current
TM	Transverse Mode
TMC	Temperature Controller
UV	Ultra-Violet
VCSEL	Vertical-Cavity Surface-Emitting Laser

List of Publications

International Journals (ISI)

[1] Y. Xie, J. Beeckman, L. Frasunkiewicz, K. Panajotov, and K. Neyts, "Vertical-Cavity Surface-Emitting Laser With Temperature-tunable External Cavity," Optics Communications (submitted).

[2] Y. Xie, J. Beeckman, K. Panajotov, and K. Neyts, "Vertical-Cavity Surface-Emitting Laser With a Liquid Crystal External Cavity," Optics Letters **39** (22), 6494-6497 (2014).

[3] Y. Xie, J. Beeckman, K. Panajotov, and K. Neyts, "Vertical-Cavity Surface-Emitting Laser With a Chiral Nematic Liquid Crystal Overlay," IEEE Photonics Journal **6** (1), 1500010 (2014).

[4] K. Panajotov, M. Dems, C. Belmonte, H. Thienpont, Y. Xie, J. Beeckman, and K. Neyts, "Vertical-Cavity Surface-Emitting Laser With Cholesteric Liquid Crystal Overlay," Journal of Lightwave Technology **32** (1), 20-26 (2014).

[5] K. Panajotov, Y. Xie [co-first author], M. Dems, C. Belmonte, H. Thienpont, J. Beeckman, and K. Neyts, "Vertical-Cavity Surface-

Emitting Laser Emitting Circularly Polarized Light," Laser Physics Letters **10** (10), 105003 (2013).

[6] Y. Xie, J. Beeckman, W. Woestenberg, K. Panajotov, and K. Neyts, "VCSEL With Photo-Aligned Liquid Crystal Overlay," IEEE Photonics Technology Letters **24**, 1509 (2012).

International Conferences

[7] Y. Xie, J. Beeckman, K. Panajotov, and K. Neyts, "Vertical cavity surface emitting laser with liquid crystal external cavity," Proceedings of SPIE **9182**, 918203, SPIE Optics and Photonics, San Diego, United States (2014).

[8] K. Neyts, O. Willekens, I. Nys, Y. Xie, M. Mohammadimasoudi, and J. Beeckman, "Liquid crystal patterns originating from structured alignment," 1st International Conference on Photoalignment and Photopatterning in Soft Materials, Hong Kong, China (2014).

[9] J. Beeckman, Y. Xie, I. Nys, and K. Neyts, "Voltage and temperature tuning of laser properties using liquid crystals," 2nd International Symposium on optics and its applications, Yerevan and Ashtarak, Armenia (2014).

[10] K. Neyts, Y. Xie, M. Callens, I. Nys, P. De Visschere, and J. Beeckman, "Spontaneous emission and tunable lasing from planar cavities containing liquid crystals," 5th Workshop on Liquid Crystals for Photonics, Erice, Italy (2014).

[11] K. Neyts, L. Penninck, Y. Xie, I. Nys, P. De Visschere, and J. Beeckman, "Spontaneous and stimulated light emission from devices with anisotropic materials," 25th International Liquid Crystal Conference, Dublin, Ireland (2014).

[12] Y. Xie, J. Beeckman, K. Panajotov, and K. Neyts, "Vertical cavity surface emitting laser with tunable liquid crystal external cavity," 12th European Conference on Liquid Crystals, Rhodes, Greece (2013).

[13] Y. Xie, J. Beeckman, K. Panajotov, and K. Neyts, "VCSEL with liquid crystal tunable external cavity," 6th European VCSEL Day, Lausanne, Switzerland (2013).

[14] Y. Xie, J. Beeckman, W. Woestenberg, K. Panajotov, and K. Neyts, "Vertical cavity surface emitting laser with nematic and chiral liquid crystal overlay," Proceedings of SPIE **8639**, 86390E, San Francisco, United States (2013).

[15] K. Panajotov, M. Dems, C. Belmonte, H. Thienpont, Y. Xie, J. Beeckman, and K. Neyts, "VCSELs with nematic and cholesteric liquid crystal overlays," Proceedings of SPIE **8639**, 86390A, San Francisco, United States (2013).

[16] Y. Xie, W. Woestenberg, J. Beeckman, K. Panajotov, and K. Neyts, "VCSEL With Photo-Aligned Liquid Crystal Overlay," 24th International Liquid Crystal Conference, Mainze, Germany (2012).

[17] Y. Xie, W. Woestenberg, J. Beeckman, K. Panajotov, and K. Neyts, "Vertical cavity surface emitting laser with photo-aligned liquid crystal overlay," 13th International Symposium on Colloidal and Molecular Electrooptics, Ghent, Belgium (2012).

[18] V. Nair, K. Panajotov, M. Petrov, H. Thienpont, Y. Xie, J. Beeckman, and K. Neyts, "850nm VCSEL with a liquid crystal overlay," Proceedings of SPIE **8432**, 84321X, Semiconductor Lasers and Laser Dynamics V, Brussels, Belgium (2012).

[19] Y. Xie, W. Woestenberg, J. Beeckman, K. Panajotov, and K. Neyts, "Light emitting properties of VCSEL chips in liquid crystal cell," Proceedings of the 16th Symposium of the IEEE Photonics Society Benelux Chapter, 53-56, Ghent, Belgium (2011).

[20] Y. Xie, W. Woestenberg, J. Beeckman, K. Panajotov, and K. Neyts, "Fabrication and characterization of VCSELs with liquid crystal overlay," 2nd International Symposium on Liquid Crystals, Changzhou, China (2011).

Scientific Awards

[1] The 2013 Chinese Government Award for Outstanding Self-financed Students Abroad was granted by China Scholarship Council (CSC). This honor is the highest award for Chinese PhD students abroad with a cash prize of 6000 USD. The Chinese Ambassador to Belgium, Mr. Liqiang Liao, awarded the certificates to the winners on May 18th 2014 in the Chinese Embassy in Brussels.

[2] The participation of the international conference SPIE Optics and Photonics 2014, held in San Diego, United State, was selected to be funded by the Research Foundation – Flanders (FWO). This grant (K1A0714N) covered the cost of flight transport between Belgium and the United State.

[3] The article "Vertical-cavity surface-emitting laser emitting circularly polarized light" authored by Krassimir Panajotov, Yi Xie, Maciej Dems, Carlos Belmonte, Hugo Thienpont, Jeroen Beeckman and Kristiaan Neyts, has been selected for the 2013 highlights of Laser Physics Letters: http://iopscience.iop.org/1612-202X/page/Highlights-of-2013 by the Institute of Physics (IOP). The work results from collaboration between the Liquid Crystals and Photonics (LCP) group

at Ghent University and the Brussels Photonics Teams (B-PHOT) group at Vrije Universiteit Brussel (VUB).

Chapter 1

Introduction

The topic of this thesis is tuning the light emitting properties of Vertical-Cavity Surface-Emitting Lasers (VCSELs) by combining VCSELs with a thin layer of liquid crystal (LC). In order to better understand the scientific results detailed further on, some basic properties of VCSELs and LCs are introduced in this chapter. For VCSELs, the characteristics are compared to other light sources, such as light emitting diodes (LEDs) and edge-emitting lasers (EELs).

1.1 Vertical-cavity surface-emitting lasers

The semiconductor industry has now progressed for more than half a century. The integration intensity of semiconductor devices have gradually increased as predicted by Gordon E. Moore [1]. However, due to quantum confinement effects of the electrons, the size of silicon transistors cannot be reduced infinitely and has certain physical limitations which are now within reach [2]. In addition there are limitations to the length of electrical interconnections, which confirms the need for development of new opto-electronic integration.

The first Vertical-Cavity Surface-Emitting Laser (VCSEL) was presented by Soda, Iga, Kitahara and Suematsu in 1979 [3]. Koyama [4] reported the first VCSEL devices for continuous wave (CW) operation at room temperature in 1988. Axel Scherer and Jack Jewell [5], two scientists at AT&T Bell Laboratories, invented the first VCSEL using semiconductor DBR in 1994.

Since then, VCSELs have been used as light sources in optoelectronic devices [6-9].

1.1.1 Structure

Similar to EELs, VCSELs are semiconductor diode lasers. Typically a VCSEL comprises a quantum wells active region and two Distributed Bragg Reflectors (DBRs) at top and bottom. Figure 1.1 shows the basic structure of a GaAs based VCSEL along with the structure of an edge-emitting laser for comparison. The semiconductor layers are epitaxially grown on a substrate. This 'wafer' is then processed to produce individual devices. In the case of edge emitters, these devices need to be cleaved so that dielectric mirrors can be deposited on the exposed facets. As shown in Figure 1.1 *right*, the light oscillates along the epitaxial layers and exits at the coated facets in a elliptical beam with high divergence in the vertical direction. In the case of VCSELs, however, the mirrors are created during the growth phase, and the light oscillates and exits normally to the epitaxial layers in a circular, low-divergence beam (Figure 1.1 *left*). The beam quality is typically much better than for an EEL. Therefore, operation of individual laser devices can be achieved without the need to cleave and separate. This is particularly advantageous for fabricating large monolithic 2D arrays of single VCSELs. By contrast, edge-emitting lasers are limited to 1D arrays.

VCSELs for wavelengths from 650 nm to 1300 nm are typically based on gallium arsenide (GaAs) wafers with DBRs consisting of GaAs and aluminum gallium arsenide ($Al_xGa_{(1-x)}As$). The GaAs–AlGaAs system is favored for constructing VCSELs because the lattice constant of the material does not vary strongly as the composition is changed, permitting multiple "lattice-matched" epitaxial layers to be grown on a GaAs substrate. In addition, the refractive index of AlGaAs varies strongly as the Al fraction is increased, minimizing the number of layers required to form an efficient Bragg mirror, compared to other candidate material systems. Furthermore, at high aluminum concentrations, an oxide can be formed from AlGaAs, which can be used to restrict the current in a VCSEL, enabling very low threshold currents.

Longer wavelength devices, from 1300 nm to 2000 nm, have been demonstrated with an active region made of indium phosphide (InP). VCSELs at even higher wavelengths are experimental and usually optically pumped. VCSELs at 1310 nm are desirable as the dispersion of silica-based optical fiber is minimal in this wavelength range.

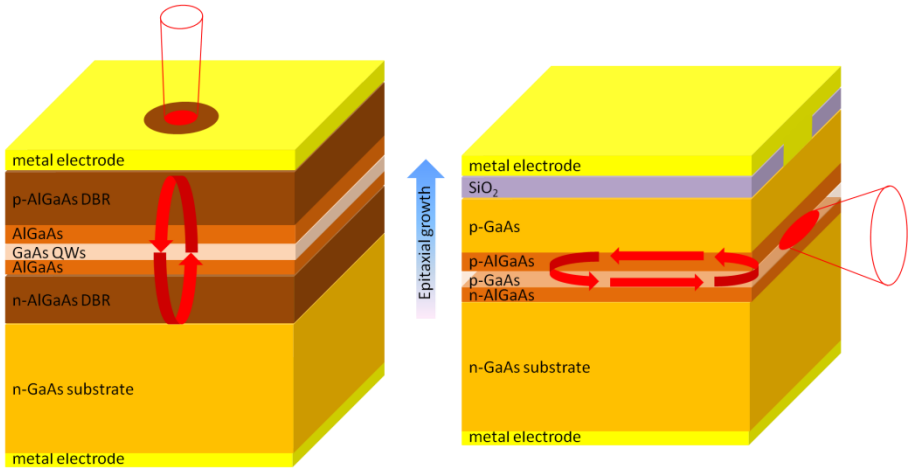

Figure 1.1: Schematic structure of VCSEL (*left*) and EEL (*right*). In a VCSEL, the light oscillates and exits perpendicularly to the epitaxial layers in a circular, low-divergence beam. In EEL, the light is oscillating along the epitaxial layers and exits at the coated facets in a high-divergence elliptical beam.

1.1.2 Parameters

The threshold current is the minimal driving current at which lasing can be achieved. In measurements, the threshold current is determined by searching the intersection point on the current-axis using least-squares linear regression for the linear part of the optical power versus driving current curve. The typical threshold current is in the order of mA. The threshold varies from 0.4 mA to 0.6 mA for the samples used in this work. The chips reach a maximal optical output power of 0.5 mW at a driving current of 1.8 mA. In this work we only consider single-mode VCSELs. Higher output powers are possible when using multi-mode VCSELs.

The polarization state of the emission is close to linear polarization. Besides this dominant emission, there is also an intrinsic emission in the orthogonal axis. If the operating condition, such as temperature or driving current, changes, this polarization can switch to its orthogonal mode. By using a certain technology (e.g. surface grating), the polarization mode can be stabilized for fluctuating temperature and operating current, as will be discussed later in this chapter.

The emitted wavelength of a VCSEL can be designed for application purposes. Many applications require low distraction level or low visibility

for the human eye, so the emission should be in the infra-red (IR) range (>815 nm). Due to the high cost of semiconductor detectors in the long wavelength range (>900 nm), the emission wavelength should be lower than this value to limit the system cost. Therefore, the wavelength is chosen as 850 nm to meet both requirements. The emission wavelength of the VCSEL used in this thesis work varies from 849 nm to 851 nm for different laser chips. The full width at half maximum (FWHM) of the spectrum is in the order of nanometer, which is much less than for IR LEDs (in the order of tens of nanometers). It is an intrinsic property that the emission wavelength red-shifts with increasing temperature. This is due to the refractive index change of the semiconductor materials with changing temperature. The wavelength-to-temperature slope is about 0.04 nm/K which is much smaller than for IR LEDs and EELs (around 0.5 nm/K). The reason is that for IR LED and EEL, the red shift is related to the red shift of the material gain with temperature.

The intensity of the laser beam of the VCSEL has a quasi-Gaussian distribution profile. The divergence angle varies from 10° to 12° for different samples.

Besides the parameters above, some additional technical parameters of IR VCSELs are compared to other IR light sources to show the advantages (Figure 1.2). Note that for this table high power IR VCSELs are considered which are not single mode. The other two commonly used IR emitters are LED and EEL. Similar to the VCSEL, they also use semiconductor GaAs as the basic material. From the comparison, it is observed that the IR VCSEL has certain advantages over alternative illuminators in terms of integration and spectral properties as well as temperature stability.



Parameters	High power IR VCSEL array	High power IR LED	IR EEL
Low cost	+	++	-
Ease of packaging	+	+	-
Output power	+	-	++
Modulation speed	+	-	+
Reliability	+	+	Neutral
Emission beam	+	-	-
Monochromaticity	++	-	+
Temperature stability	+	-	-

Figure 1.2: Comparison of IR VCSEL, IR LED and IR EEL [10].

1.1.3 Applications

Thanks to their interesting properties, VCSELs have been used in many areas. The well-developed technology of VCSEL fabrication and integration makes this laser a good candidate for many applications where low cost, high beam quality, and high transmission efficiency are needed. Because the VCSEL fabrication can be processed and tested on wafer level, the cost is much lower than for EEL. Additionally, the VCSEL chips can be easily integrated into an array which has a higher output power and arbitrary beam patterns. These advantages make VCSELs good candidates for broad industrial applications, not only in optical communication and sensing, but also in laser printers, computer mice, biological analysis and chip-scale atomic clocks. Some popular products on the market today are shown in Figure 1.3. It is clear that VCSELs are present in our everyday life, from personal computers to airplanes.

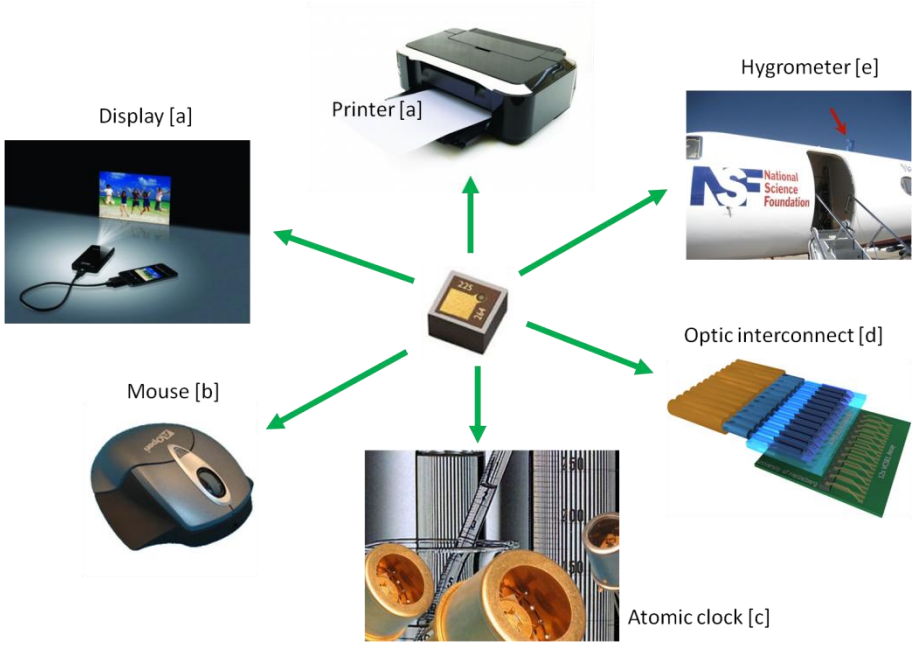

Figure 1.3: Some commercial products which make use of VCSELs. Picture sources: (a) CompoundSemiconductor [11], (b) AOPEN [12], (c) Lasercomponents [13], (d) Heidelberg University [14], (e) NCAR-EOL [15].

Although VCSELs have been successfully integrated in many applications, there is still room for improvement in order to realize novel, more challenging applications. For example, if the polarization state and emitting wavelength of the VCSEL emission can be tuned or controlled, VCSELs can be used in intelligent devices and function as 'smart' light sources, which would allow for a broader application range.

1.2 Liquid crystals

The basic physical properties of LCs will be introduced in this section. LC is a material with anisotropic optical properties, which means that the optical refractive indices are different along its long and short axis. Thanks to this anisotropy, LC has been applied with great success in displays. Additionally, LC has been used in lasing, imaging and other optical applications. This section will introduce the basic concepts required to understand the material discussed in this work. We refer to other works for a broader introduction of LC, including its physical properties [16-21] and applications [22-25].

1.2.1 Nematic liquid crystals

The two LC phases that are applied in this thesis work are illustrated in Figure 1.4. The molecules of nematic LC are longer in one direction, are randomly distributed and move as in a liquid, but they have long-range directional order. The nematic phase is uniaxial: there is one axis along the preferred direction for the long shaped molecules, while the other two axes are equivalent (due to the easy rotation of the molecules along their long axis). Nematic LC molecules can be aligned by an external electric field or by surface alignment technologies, which will be introduced in section 1.3. Nematic LC exhibits LC behavior in a limited temperature range. If the temperature is too low, the molecules are fixed in a lattice and the material is in the solid phase. If the temperature is higher than the melting point but lower than the clearing point, molecules tend to orient along a common direction, and form a nematic phase. When the temperature is higher than the clearing point, all molecules orient randomly, this is the liquid phase. The phase transitions of nematic LC are presented in Figure 1.5 by illustrating the orientation of the molecules. Different kinds of nematic LCs have different clearing point and melting point. Two commonly used nematic LC materials in this thesis work are E7 and 5CB. The nematic phase temperature range is from -10˚C to 60˚C for E7, and from 18˚C to 35˚C for 5CB.

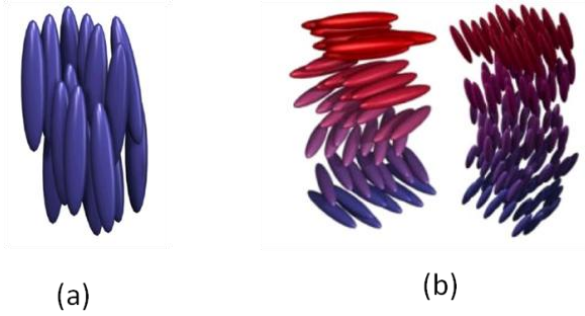

Figure 1.4: Schematic representations of LC phases: (a) nematic, (b) chiral. Original figure from [26].

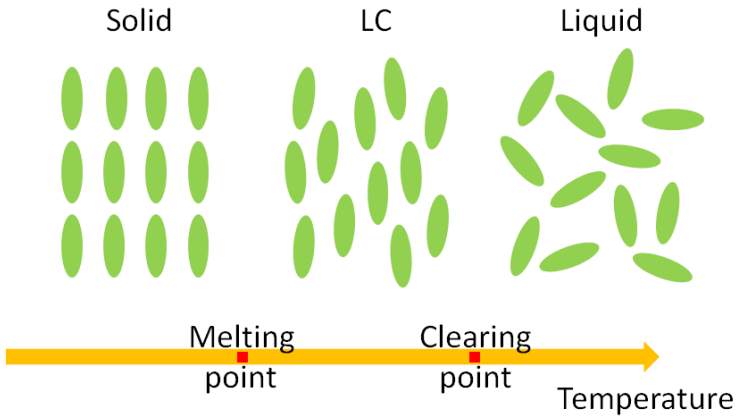

Figure 1.5: Illustration of phase transition of LC material.

1.2.1.1 Alignment

To achieve the best effect of nematic LC reorientation in applications, nematic LC molecules are typically aligned using alignment technologies. Commonly used technologies are rubbing [27] and photo-alignment [28, 29]. Both technologies have their advantages and special application areas.

1.2.1.1.1 Rubbing

Rubbing is a technique using a mechanical force on the surface of polymers to reorient the polymer molecules in a common direction. Rubbing results in a very uniform alignment of LC molecules which is the reason why it is widely used in LC displays. However, this technique needs mechanical contact on the substrate surface, which could influence or damage the fine structure that is deposited on the surface. For example, in our VCSEL devices, there are complex structures (either coated electrodes or evaporated reflectors) on the top substrate which can be influenced by the rubbing process. Furthermore, rubbing defines the alignment before the construction of the cell, in other words, the alignment direction cannot be changed after the cell is completed. But in the VCSEL cell fabrication procedure, the alignment direction is determined only after the cell has been completed. Therefore, rubbing techniques are not suitable for VCSEL applications. Another method is photo-alignment which avoids the two disadvantages mentioned above.

1.2.1.1.2 Photo-alignment

The orientation of the average molecular axis (director) of LCs relative to a surface plane of a substrate is critically determined by the nature of the surface [30]. There are two extremes for LC orientation: homeotropic alignment, where the LC director is perpendicular to the substrate, and planar alignment, where the LC director is parallel to the substrate. When a substrate surface is modified with photochromic molecules to alter the chemical structures and molecular orientation of the uppermost surface in molecular levels, the alignment of nematic LC is controlled reversibly by alternate irradiation patterns [31, 32]. This kind of photo triggered control of LC alignment was first reported in 1988 [33]. The photoalignment is realized by depositing photochromic molecules on a substrate with surface density of 1 unit/nm^2 or less [33, 34]. Each photochromic molecule can command the reversible alignment of about 10^4 LC molecules [31-35].

In our research, a thin layer of photochromic material is spin-coated on the glass substrate. It is transparent and homogeneous. The alignment is determined by the polarization of the exposed UV light source. Under linearly polarized UV light, the molecules in the photo-alignment material reorient in order to make their absorption oscillator perpendicular to the polarization direction of the UV light. LC molecules reorient following the molecules under the influence of strong anchoring energy. As a consequence the liquid crystal molecules align perpendicular to the polarization direction of the UV light. This process is shown in Figure 1.6. Two cases are shown here: alignment of LC director is parallel to the substrate surface (Figure 1.6A2) or with a certain pre-tilt angle to the substrate surface (Figure 1.6B2). The former case uses one step of UV exposure shown in Figure 1.6A1 and is the method used in this thesis work. While, the latter case uses two steps of UV exposure (Figure 1.6A1 followed by 1.6B1). The advantage of photo-alignment is that it does not need any mechanical process and there is no damage of the surface. Another advantage is that the layer can be patterned easily, leading to spatially varying LC orientation. Applications of such spatially varying alignment are improved display characteristics, switchable holographic gratings and improved tunable photonic devices (e.g. waveguides).

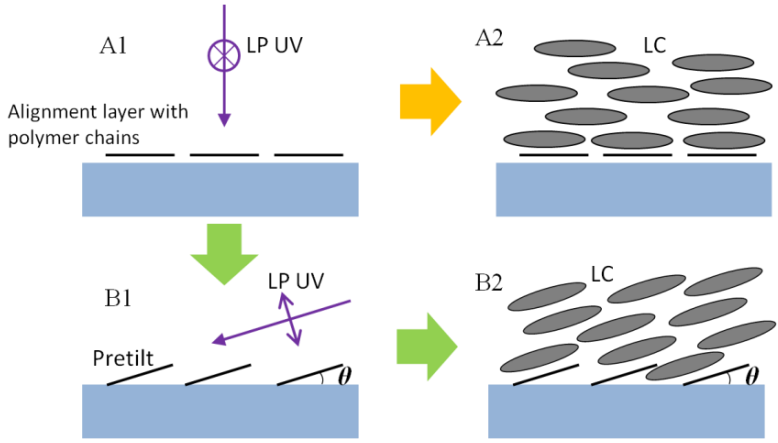

Figure 1.6: (A1) linearly polarized UV light illuminates perpendicular to the substrate and introduces alignment of polymer chains (perpendicular to the polarization plane of the UV light); (A2) LC director aligns parallel to the polymer following the step of A1 and forms a planar alignment; (B1) after step A1, another linearly polarized UV light is exposed with an angle θ to the substrate, so the polymer chains tilt to align perpendicular to the polarization director; (B2) LC director aligns parallel to the polymer following the step of B1 and forms a pre-tilted alignment.

1.2.1.2 Electrical reorientation of nematic liquid crystal molecules

For an aligned planar nematic LC layer, the LC director can reorient in response to an applied electric field across the layer. This basic effect is called electrically controlled birefringence [36]. Figure 1.7 shows a planar texture of nematic LC between two substrates that have transparent ITO electrodes. The director is indicated in the coordinate system. The director orientation can be described by the tilt angle θ. In the "field off" state θ is determined by the alignment technology and can have a pre-tilt angle.

When a voltage is applied across the LC layer, the LC with positive dielectric anisotropy is reoriented and its tilt angle is changed towards the direction of the created electric field. Important to note is that the tilt angle $\theta(z)$ is a function of z and depends on the applied voltage. The distribution of the director tilt angle is a result of a balance between electric forces and elastic restoring forces. The elastic restoring force is given by the elastic constants of the LC and the type of deformation. For a planar LC cell with identical alignment at the top and at the bottom, the elastic energy density can be written as [21]

$$u_{elastic} = \frac{1}{2}(K_1 \cos^2\theta + K_3 \sin^2\theta)(\frac{d\theta}{dz})^2, \qquad (1.1)$$

where θ is the tilt angle, K_1 the splay, and K_3 the bend elastic constants. The change of electrostatic energy due to the reorientation of the director can be written as

$$\Delta u_{electric} = \frac{1}{2\varepsilon_0} \frac{D_z^2}{\varepsilon_p \cos^2\theta + \varepsilon_s \sin^2\theta} - \frac{D_z^2}{2\varepsilon_0 \varepsilon_s}, \qquad (1.2)$$

where D_z is the z-component of the dielectric displacement field vector. The dielectric constants are measured at low frequencies, typically 1 kHz. Distortion occurs if the voltage is higher than a critical voltage:

$$V_{threshold} = E_{threshold} d = \pi \sqrt{\frac{K_1}{\Delta\varepsilon\varepsilon_0}}. \qquad (1.3)$$

where d is the thickness of the LC cell. The LC transition behavior with a threshold voltage is called the Fredericks transition. The tilt angle profile can be simulated and is presented in Figure 1.8 for different voltages applied across the LC layer.

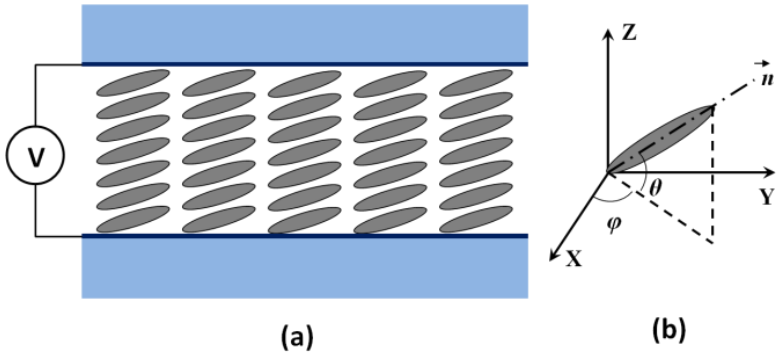

Figure 1.7: (a) schematic drawing of a LC layer, across which a voltage can be applied; (b) one LC molecule and the director are shown in the coordinates: ***n*** is the director, θ is the tilt angle, φ is the azimuth angle of LC director with respect to the *x* axis.

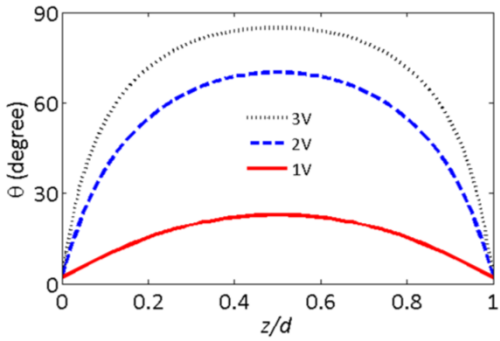

Figure 1.8: Simulation of the tilt angle of LC director as a function of z. Different voltages are applied over the LC layer.

1.2.1.3 Propagation of polarized light in nematic liquid crystal layers

The propagation of polarized light in LC layers is theoretically represented by the Jones matrix formalism [37] and discussed in Appendix B. Assume the light is propagating in the z-direction in the coordinate system shown in Figure 1.7. Considering the Jones vector of the light in the *x* and *y* directions $\begin{bmatrix} A_x \\ A_y \end{bmatrix}$, the optical axis of the LC needs to be rotated to coincide with the *x* axis using the rotation matrix $\boldsymbol{R}(\varphi)$:

$$\boldsymbol{R}(\varphi) = \begin{bmatrix} \cos\varphi & \sin\varphi \\ -\sin\varphi & \cos\varphi \end{bmatrix}. \tag{1.4}$$

Then the expression for light propagation through the LC cell is

$$\boldsymbol{A}_{out} = \boldsymbol{R}(-\varphi)\boldsymbol{J}_{LC}\boldsymbol{R}(\varphi)\boldsymbol{A}_{in}, \tag{1.5}$$

where $\boldsymbol{J}_{LC}$ is the Jones matrix of the LC layer and φ is the azimuth angle of LC director with respect to *x* axis indicated in Figure 1.7(b).

$\boldsymbol{J}_{LC}$ is defined as

$$\boldsymbol{J}_{LC} = \begin{bmatrix} e^{-i\frac{\Gamma}{2}} & 0 \\ 0 & e^{i\frac{\Gamma}{2}} \end{bmatrix}. \tag{1.6}$$

Considering the electrical reorientation of the LC, as explained in the previous section, a phase retardation due to the LC cell can be expressed as

$$\Gamma = \frac{2\pi}{\lambda}\int_0^d \left(n_{eff}(z) - n_o\right)dz \tag{1.7}$$

where, d is the thickness of the LC layer. The effective refractive index is given by

$$n_{eff}(z) = \frac{n_e n_o}{\sqrt{n_e^2 \sin^2 \theta(z) + n_o^2 \cos^2 \theta(z)}} \qquad (1.8)$$

where $\theta(z)$ is the tilt angle of LC director which is a function of z and depends on the applied voltage, as demonstrated in Figure 1.8.

The phase retardation as a function of the voltage applied over the LC layer is simulated and shown in Figure 1.9.

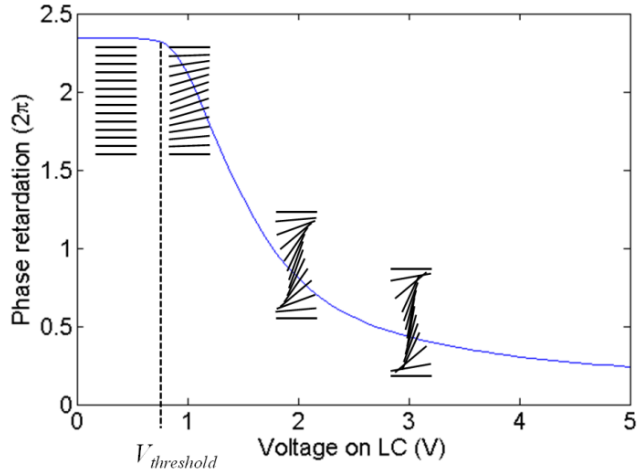

Figure 1.9: Simulated retardation of a planar aligned LC layer (thickness of 10 μm). The LC director configuration is shown for different voltage values.

Therefore, the Jones vector of the light transmitted through the LCs in the x and y direction $\begin{bmatrix} A_x^{out} \\ A_y^{out} \end{bmatrix}$ are related to the Jones vector of the incoming light $\begin{bmatrix} A_x^{in} \\ A_y^{in} \end{bmatrix}$ by Equation (1.5):

$$\begin{bmatrix} A_x^{out} \\ A_y^{out} \end{bmatrix} = \begin{bmatrix} \cos\varphi & -\sin\varphi \\ \sin\varphi & \cos\varphi \end{bmatrix} \begin{bmatrix} \exp(-i\frac{\pi}{\lambda}\int_0^d (n_{eff}(z)-n_o)dz) & 0 \\ 0 & \exp(i\frac{\pi}{\lambda}\int_0^d (n_{eff}(z)-n_o)dz) \end{bmatrix} \begin{bmatrix} \cos\varphi & \sin\varphi \\ -\sin\varphi & \cos\varphi \end{bmatrix} \begin{bmatrix} A_x^{in} \\ A_y^{in} \end{bmatrix} \quad (1.9)$$

1.2.2 Chiral liquid crystals

Nematic LC can be doped with chiral dopant in order to obtain a chiral liquid crystal (CLC) material which has a helical arrangement of the molecules [23]. The concentration of the chiral dopant can be adjusted such that the material exhibits a photonic reflection band for visible or near-infrared light for one circular polarization (either right- or left-handed depending on the chiral dopant). The orientation of the CLC directors and the electric vectors of circularly polarized light are visualized in Figure 1.10. The director of CLC rotates 360˚ over a certain distance, called the pitch (p), making the structure periodic. Circularly polarized light which has its wavelength inside of the reflection band of the CLC ($p \times n_o < \lambda < p \times n_e$) and has the same handedness of CLC helix will be reflected back. Circularly polarized light with the opposite handedness will be transmitted through the CLC. There are many applications based on this optical property of CLC, for example lasing and spontaneous light emission [38-40].

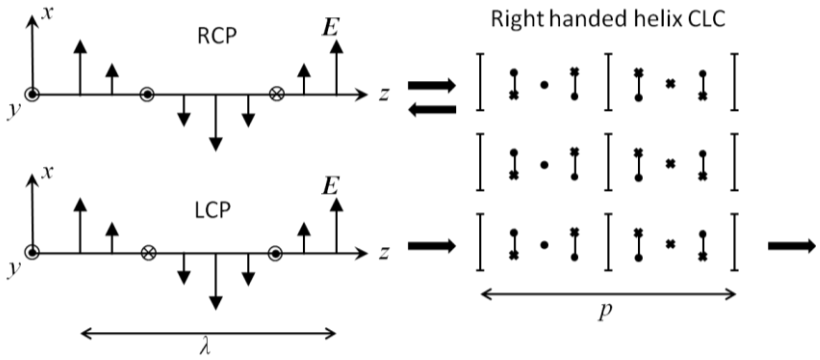

Figure 1.10: Electric field vectors for right-handed circular polarization (RCP) and left-handed circular polarization (LCP) at a certain time, as a function of the coordinate (*left*). Right handed helical chiral LC director orientation (*right*). One pitch is shown. If the wavelength and handedness of the circularly polarized light match with the pitch (in between the productions of pitch and the two refractive index of LC, respectively) and the handedness of the CLC, the light will be reflected.

1.3 Review on recent VCSEL advances

In this section, the literature of VCSEL research is studied and summarized. The statistics of the publications and citations on the VCSEL topic is illustrated in Figure 1.11. The number of citations clearly shows that the VCSEL research attracts more and more interest since 1990's. This increasing trend seems to continue in the future.

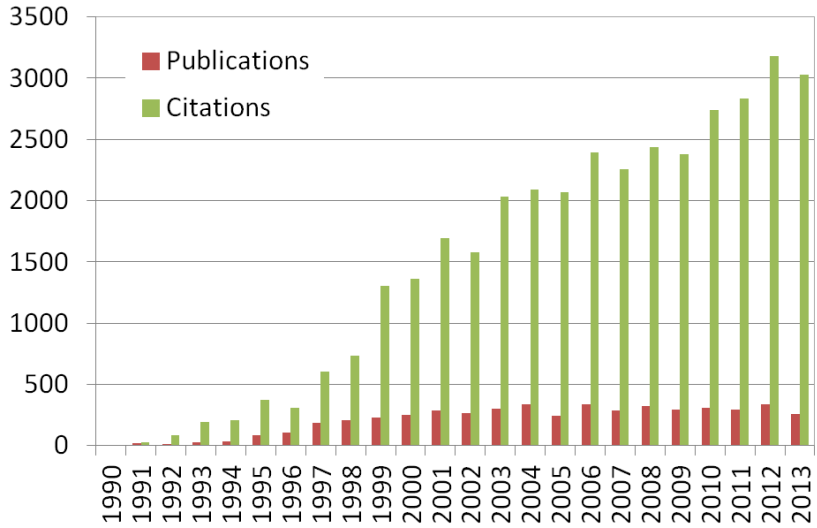

Figure 1.11: Statistics of the publications and citations of VCSEL research in the past two decades. The data come from Web of Science.

The research topics on VCSELs cover broad areas, from fabrication materials to emission properties. We select a few topics, including polarization stabilization and switching, transverse modes control and emission wavelength tuning, which are related to this thesis work and present them as below.

1.3.1 Polarization stabilization

The two modes of the cavity are linearly polarized, and due to the crystallinity, their electric fields are along the [011] or the [$0\bar{1}1$]

crystallographic directions parallel to the epitaxial layers [41-43]. The polarization of the lasing can switch between these two directions because of temperature, injection current, or optical feedback effects. This polarization instability restricts the application of VCSELs in polarization-sensitive areas, such as light sources, optical interconnects, and optical communication. Many efforts have been made to stabilize the polarization directions of VCSELs by using anisotropic aperture geometries [44-46], surface gratings [47-49], extremely short external cavities [50], asymmetric current injections [51, 52], misoriented substrates [53] or anisotropic active layers [54].

1.3.2 Polarization switching

Beyond stabilization, robust control or selection of the polarization is also interesting for applications. A lot of work has been done to switch the polarization between the two orthogonal linear modes in a controlled way [55-63]. Controlled polarization switching is realized by using optical feedback [55-59], RF frequency modulation [60], optical injection [61, 62], and thermal-optic effect [63]. In one popular strategy, an external reflector is introduced to reflect the laser light back into the VCSEL (optical feedback), which forms an external cavity. The polarization can be controlled by modulating the optical feedback (as shown in Figure 1.12 and 1.13). By changing the optical length of the external cavity, the reflectivity for a certain wavelength is changed. Since the wavelength of the two polarizations is slightly different, the external cavity length will modulate the gain of lasing for the two polarizations in a different way, and determine which polarization will have the lower lasing threshold. In this work, we use optical feedback to switch the polarization. In Chapter 5, the external cavity is built up by using a metal or dielectric reflector, which length can be tuned by temperature. The polarization switches between two orthogonal modes by changing device temperature. In Chapter 6, the optical feedback is electrically controlled by the LC layer between the VCSEL and a dielectric mirror. Fast and stable polarization switching is realized by applying suitable voltage signals over the LC layer.

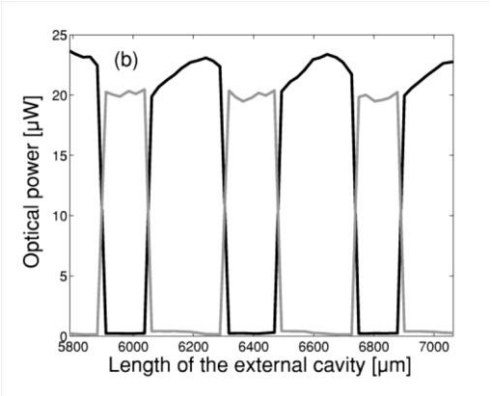

Figure 1.12: Polarization switching by tuning the length of the external cavity (Figure 3b in [56]).

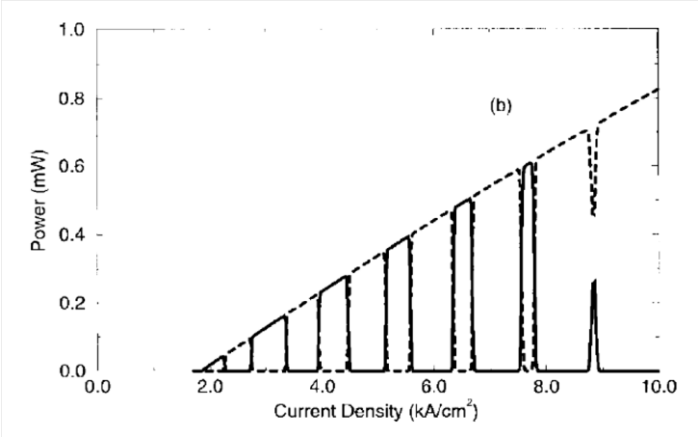

Figure 1.13: Polarization switching by current induced external cavity phase change (Figure 1b in [58]).

1.3.3 Transverse mode modulation

Due to the relatively large transverse size in combination with a symmetric geometry and isotropic material properties, the VCSEL tends to lase in several transverse modes with an unpredictable state of polarization. In order to meet the requirement for applications, the transverse mode should be under control. The transverse mode can be modulated using different dynamics [64-66]. The transverse mode in a multimode VCSEL can be controlled by injected current density [64, 65] (shown in Figure 1.14),

aperture size [65], or optical feedback [66]. In this thesis work, the transverse beam profiles can be modulated by a thermally tunable external cavity of the VCSEL. The external cavity is formed by an extra reflector deposited on the top substrate of the device and the air gap in between this reflector and the VCSEL. When the device temperature increases, the external cavity length increases as a result of thermal expansion effect of the whole device. Therefore, the transverse mode of the emission changes due to the optical feedback. The fundamental mode and higher-order modes are observed in the far field images of the VCSEL device at different temperatures. The experimental results agree with theoretical simulations very well.

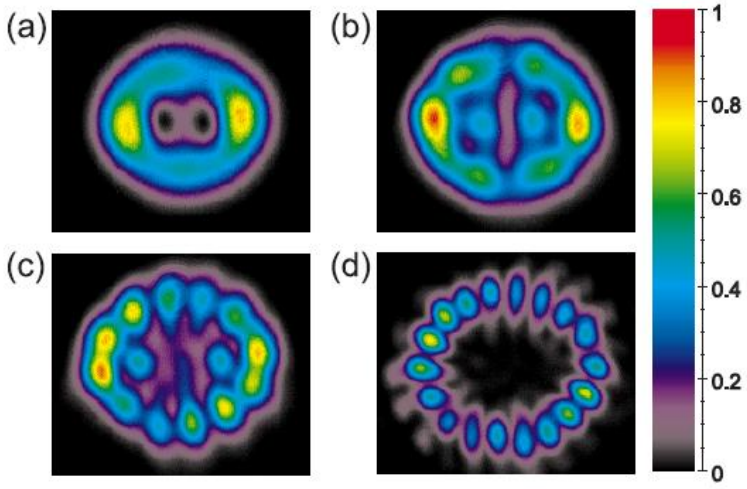

Figure 1.14: Near field images of the VCSEL at different injected currents: (a) 8.8 mA, (b) 15.5 mA, (c) 23 mA and (d) 29.9 mA. (Figure 5 in [63])

1.3.4 Wavelength tuning

Researchers aim to tune the emission wavelength of VCSELs [6, 67-74]. Many technologies have been developed for this purpose. One method to tune the VCSEL wavelength is using micro-electronic mechanic system (MEMS) DBR as the top reflector of the laser, which is intensively studied recently. In this method, the fixed epitaxial top mirror of a standard VCSEL is replaced by a movable mirror membrane. This MEMS-VCSEL is typically prepared by combining a MEMS dielectric membrane and a “half-VCSEL”,

which has only a bottom DBR. This "two-chip" design avoids the need of making disadvantageous compromises for neither the micromechanics nor the VCSEL amplifier. The air gap between the MEMS layer and the top of the half-VCSEL determines the cavity length. The MEMS layer can be tuned by electrostatic actuation. Under actuator voltage change of tens of volts, the deflection of the MEMS layer can reach to a few micrometers. The cavity length and consequently the emission wavelength can be tuned by the mechanical movement of the MEMS layer. The realized continuous wavelength tuning range of a single mode MEMS-VCSEL based on GaAs or indium phosphate (InP) is about 30 nm or 80 nm [72-74], respectively.

Another novel approach is to utilize liquid crystals (LCs) in the VCSEL geometry to modulate the optical properties of the emission, because LC has anisotropic optical properties [6, 67]. In [67], a tunable VCSEL with an intracavity layer of nematic liquid crystal is fabricated. It has a continuously tunable single-mode laser emission in the telecom wavelength range and the tuning range is wider than 30 nm for less than 3 V applied voltage. In [6], a nano-polymer dispersed LC (nano-PDLC) layer is fabricated in between the active layer and the top DBR inside a long-wavelength VCSEL. This nano-PDLC plays as an electro-optic index modulator. By tuning the voltage (0 – 170 V) applied between the top and the bottom DBR, the emission peak wavelength can be tuned by 10 nm (shown in Figure 1.15). In this thesis work, the realized wavelength tuning of the integrated LC-VCSEL device is around 1~2 nm (presented in chapter 4, 5 and 6). However, we are able to increase this tuning range up to more than 10 nm by using a VCSEL without top DBR (half-VCSEL) in our integrated device as expected from theoretical simulations (see section 7.2). It is interesting that this wavelength tunability would be comparable with that of MEMS-VCSELs which are based on the same GaAs materials.

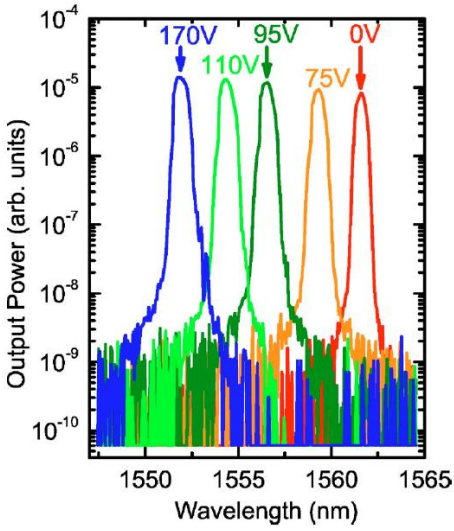

Figure 1.15: Emission spectra of nano-PDLC VCSEL at different tuning voltage values. (Figure 2 in [6])

In this work, we describe our new technology to fabricate an electrically driven integrated LC-VCSEL device which has multiple functions: polarization, beam profile, threshold and wavelength can be controlled thermally or electrically [75-78].

Chapter 2

Simulation Method

In this chapter, the theoretical simulation method used in this work will be introduced. The simulations are based on the plane wave expansion theory, which is discussed in section 2.1. To show how this method works for the combination of VCSEL and LC, some simple calculation results for a bare VCSEL and a CLC thin layer are presented in section 2.2. In the later chapters of this work, the simulation method is applied to different types of VCSEL devices to investigate the physics behind the experimental results. By comparing the simulations with the measurements, the advanced device properties can be better understood.

2.1 Plane wave expansion theory

A plane wave is an electromagnetic wave that extends over all directions with constant amplitude. The propagation of a plane wave is illustrated in Figure 2.1. The electric field of a plane wave can be written as:

$$\boldsymbol{E}(x,y,z,t) = \boldsymbol{E}_0 e^{-i(k_x x + k_y y + k_z z - \omega t)} \tag{2.1}$$

At a fixed time point, the phase of the plane wave is constant in a certain infinite plane normal to the propagating direction (a phasefront).

The plane wave is characterized by its wave-vector $\boldsymbol{k}$:

$$\boldsymbol{k} = [k_x \quad k_y \quad k_z] \tag{2.2}$$

The magnetic field $\boldsymbol{H}$ can be calculated by using $\nabla \times \boldsymbol{E} = -i\omega\mu\boldsymbol{H}$.

$$\boldsymbol{H}(x,y,z,t) = \frac{\boldsymbol{k}\times\boldsymbol{E}_0}{\omega\mu} e^{-i(k_x x + k_y y + k_z z - \omega t)} \tag{2.3}$$

The power flux carried by the plane wave is given by Poyntings vector:

$$\boldsymbol{S} = \frac{1}{2} Re[\boldsymbol{E} \times \boldsymbol{H}^*] \tag{2.4}$$

The plane wave can be also characterized by angles θ and φ, defined in the coordinate system in Figure 2.1. The in-plane wave vector $\boldsymbol{\kappa}$ is the projection of $\boldsymbol{k}$ in the x-y plane.

$$\kappa = \sqrt{k^2 - {k_z}^2} = k\cos\theta \tag{2.5}$$

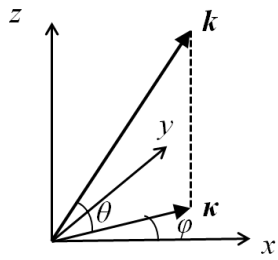

Figure 2.1: The propagation of a plane wave is defined by its wave vector $\boldsymbol{k}$ or by angles θ and φ.

2.1.1 Emission in anisotropic cavities

Based on plane wave decomposition, a model for dipole radiation in an infinite medium has been developed [79]. This model can be applied to anisotropic cavities by considering different refractive index in different axis directions and the interference effects [80]. The plane wave fields can be decomposed into transverse electric (TE) and transverse magnetic (TM) polarization in isotropic media, but should be decomposed to ordinary (o) and extraordinary (e) waves in anisotropic media. Because the o- and e-waves are coupled when reflection or transmission at an interface takes place in anisotropic media, the reflection coefficients have to be replaced by the

reflection matrices ($\boldsymbol{A}^{+}$ or $\boldsymbol{A}^{-}$). The reflected waves are presented in Figure 2.2. The electric field in an infinite medium ($E_{\infty,o/e}^{+/-}$) should be altered by the interference induced by the reflections in the cavity. The multiple beam interference can be expressed by $1-\boldsymbol{A}^{-/+}\boldsymbol{A}^{+/-}$, the wide angle interference can be expressed by $\boldsymbol{E}_{\infty}^{+/-}+\boldsymbol{A}^{-/+}\boldsymbol{E}_{\infty}^{-/+}$.

Therefore, the field amplitudes of the decomposed waves are:

$$\begin{bmatrix} E_{cav,o}^{+} \\ E_{cav,e}^{+} \end{bmatrix} = (1-\boldsymbol{A}^{-}\boldsymbol{A}^{+})^{-1}\left(\begin{bmatrix} E_{\infty,o}^{+} \\ E_{\infty,e}^{+} \end{bmatrix} + \boldsymbol{A}^{-}\begin{bmatrix} E_{\infty,o}^{-} \\ E_{\infty,e}^{-} \end{bmatrix}\right) \tag{2.6}$$

$$\begin{bmatrix} E_{cav,o}^{-} \\ E_{cav,e}^{-} \end{bmatrix} = (1-\boldsymbol{A}^{+}\boldsymbol{A}^{-})^{-1}\left(\begin{bmatrix} E_{\infty,o}^{-} \\ E_{\infty,e}^{-} \end{bmatrix} + \boldsymbol{A}^{+}\begin{bmatrix} E_{\infty,o}^{+} \\ E_{\infty,e}^{+} \end{bmatrix}\right) \tag{2.7}$$

E_{cav} or E_{∞} stands for the field in the cavity or in an infinite medium. $\boldsymbol{A}^{+}$ or $\boldsymbol{A}^{-}$ is a 2×2 reflection matrix which describes the coupling between the ordinary and extraordinary polarized waves during the reflection.

$$\boldsymbol{A}^{\pm} = \begin{bmatrix} A_{oo}^{\pm} & A_{eo}^{\pm} \\ A_{oe}^{\pm} & A_{ee}^{\pm} \end{bmatrix} \tag{2.8}$$

The output fields emitted from the cavity can be calculated as:

$$\begin{bmatrix} E_{out,o}^{\pm} \\ E_{out,e}^{\pm} \end{bmatrix} = \boldsymbol{T}^{\pm}\begin{bmatrix} E_{cav,o}^{\pm} \\ E_{cav,e}^{\pm} \end{bmatrix} \tag{2.9}$$

Similar to the reflection matrices, $\boldsymbol{T}^{+}$ or $\boldsymbol{T}^{-}$ is a 2×2 transmission matrix which describes the coupling between the o- and e- waves during the transmission.

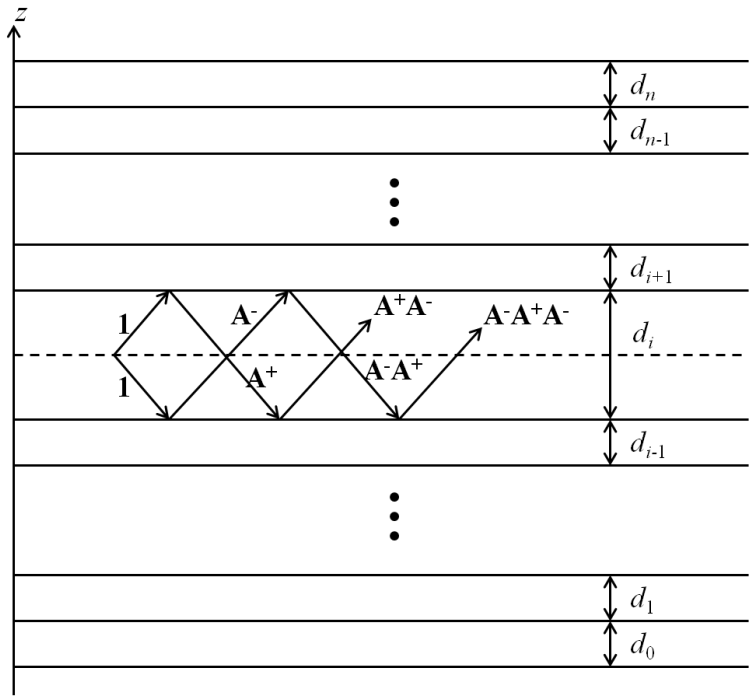

Figure 2.2: A plane wave is radiated and reflected in a stack of anisotropic films (consisting of n+1 layers). The wave is modified by interference with reflections of the cavity interfaces above (noted by +) and below (noted by -) (Figure 2 in [80]).

2.1.2 Reflection and transmission of anisotropic thin layer structures

In the previous section, it is presented that the plane wave fields in anisotropic cavities can be calculated if reflection and transmission matrices are known. This section shows how to obtain the reflection and transmission matrices of a stack of uniaxially anisotropic layers using the scattering matrix method [80, 81].

The 4×4 scattering matrix $\boldsymbol{S_{i,n}}$ relates incoming waves to outgoing waves (Figure 2.3) between layers with indices i and n with $i<n$.

$$\begin{bmatrix} E_{o,n,+} \\ E_{e,n,+} \\ E_{o,i,-} \\ E_{e,i,-} \end{bmatrix} = \boldsymbol{S_{i,n}} \begin{bmatrix} E_{o,i,+} \\ E_{e,i,+} \\ E_{o,n,-} \\ E_{e,n,-} \end{bmatrix} \tag{2.10}$$

The scattering matrix $\boldsymbol{S_{i,n}}$ can be treated as a block matrix consisting of four 2×2 matrices. Once $\boldsymbol{S_{i,n}}$ is determined, the reflection matrix $\boldsymbol{A}^+$ and the transmission matrix $\boldsymbol{T}^+$ can be identified by one 2×2 matrix of $\boldsymbol{S_{i,n}}$:

$$\boldsymbol{A}^+ = \boldsymbol{S_{i,n}}(21) \tag{2.11}$$

$$\boldsymbol{T}^+ = \boldsymbol{S_{i,n}}(11) \tag{2.12}$$

Another matrix $\boldsymbol{I}$ can be used to relate the waves in neighboring layers (Figure 2.3).

$$\begin{bmatrix} E_{o,j+1,+} \\ E_{e,j+1,+} \\ E_{o,j+1,-} \\ E_{e,j+1,-} \end{bmatrix} = \boldsymbol{I_j} \begin{bmatrix} E_{o,j,+} \\ E_{e,j,+} \\ E_{o,j,-} \\ E_{e,j,-} \end{bmatrix} \tag{2.13}$$

The scattering matrix $\boldsymbol{S_{i,n}}$ can be found by successively adding all layers from number (i+1) to n on top on the starting layer number i. The relation between the successive scattering matrix $\boldsymbol{S_{i,\,j}}$ and $\boldsymbol{S_{i,\,j+1}}$ is identified by the matrix $\boldsymbol{I_j}$ as following:

$$\begin{aligned}
\boldsymbol{S_{i,j+1}}(11) &= (\boldsymbol{I_j}(11)^{-1} - \boldsymbol{S_{i,j}}(12)\boldsymbol{I_j}(21)^{-1})^{-1}\boldsymbol{S_{i,j}}(11) \\
\boldsymbol{S_{i,j+1}}(12) &= \left(\boldsymbol{I_j}(11)^{-1} - \boldsymbol{S_{i,j}}(12)\boldsymbol{I_j}(21)^{-1}\right)^{-1}(\boldsymbol{S_{i,j}}(12)\boldsymbol{I_j}(22)^{-1} - \boldsymbol{I_j}(12)^{-1}) \\
\boldsymbol{S_{i,j+1}}(21) &= \boldsymbol{S_{i,j}}(22)\boldsymbol{I_j}(21)^{-1}\boldsymbol{S_{i,j+1}}(11) + \boldsymbol{S_{i,j}}(21) \\
\boldsymbol{S_{i,j+1}}(22) &= \boldsymbol{S_{i,j}}(22)\boldsymbol{I_j}(21)^{-1}\boldsymbol{S_{i,j+1}}(12) + \boldsymbol{S_{i,j}}(22)\boldsymbol{I_j}(22)^{-1}
\end{aligned} \tag{2.14}$$

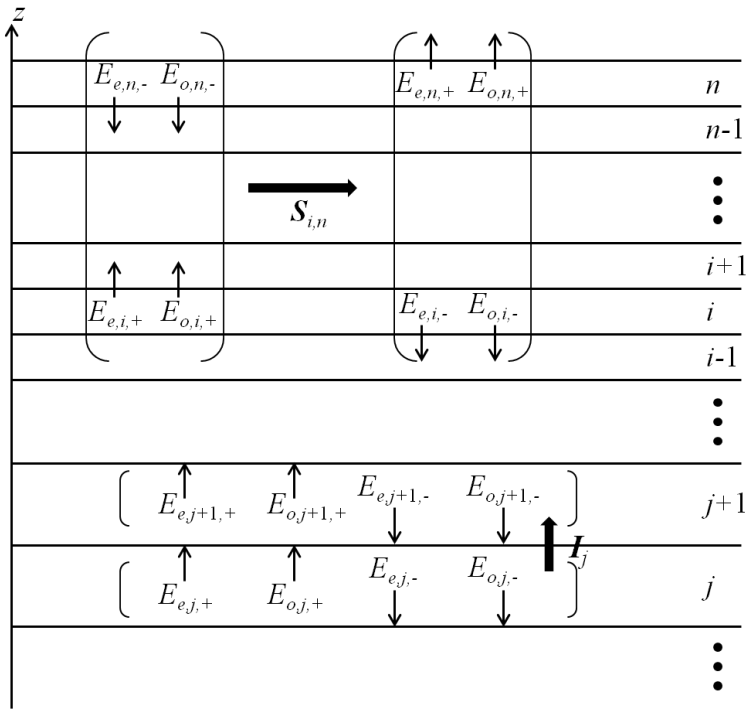

Figure 2.3: Scattering matrix **S** relates input-output waves (*up*). Matrix **I** relates waves in neighbor layers (*down*) (Figure 3 and 4 in [80]).

2.2 Simulation examples

To understand and predict the emission properties of the VCSEL device, theoretical simulations of the electric fields inside the system are performed in Matlab. The algorithm is a one-dimensional matrix operation for an input vector using the transmission and refection formalism. The system is treated as a multiple layer structure, each layer has its own optical refractive index and thickness. The simulation uses the plane wave expansion method described in [40] which is further extended for the simulation of lasing characteristics of devices with optical anisotropy [39]. The simulated configuration together with the values of the different material properties can be found in [82].

2.2.1 CLC thin layers

The simulation is performed for a 10 μm film of right-handed helical CLC. The host LC is E7 (n_o=1.5, n_e=1.7) and the pitch of the CLC is set as

530 nm. The CLC film is treated as discrete multiple layers, 36 layers in one pitch are used. This means that the optic director of the LC rotates 10˚ in the x-y plane from one layer to the next. The multiple layer structure of the CLC film is shown in Figure 2.4. Using the matrix operation method introduced in section 2.1, the outgoing electric fields are calculated in the form of Jones vectors. Assuming that linearly polarized light along the x axis is incoming to the CLC layer from the bottom ($\boldsymbol{J}_{\text{in}} = [1\ 0]$), the reflection and transmission Jones vectors ($\boldsymbol{J_1}$ and $\boldsymbol{J_2}$) are calculated for different wavelengths:

$$\boldsymbol{J_1} = \begin{bmatrix} J_1(1) \\ J_1(2) \end{bmatrix} = \boldsymbol{A^+ J_{in}} \tag{2.15}$$

$$\boldsymbol{J_2} = \begin{bmatrix} J_2(1) \\ J_2(2) \end{bmatrix} = \boldsymbol{T^+ J_{in}} \tag{2.16}$$

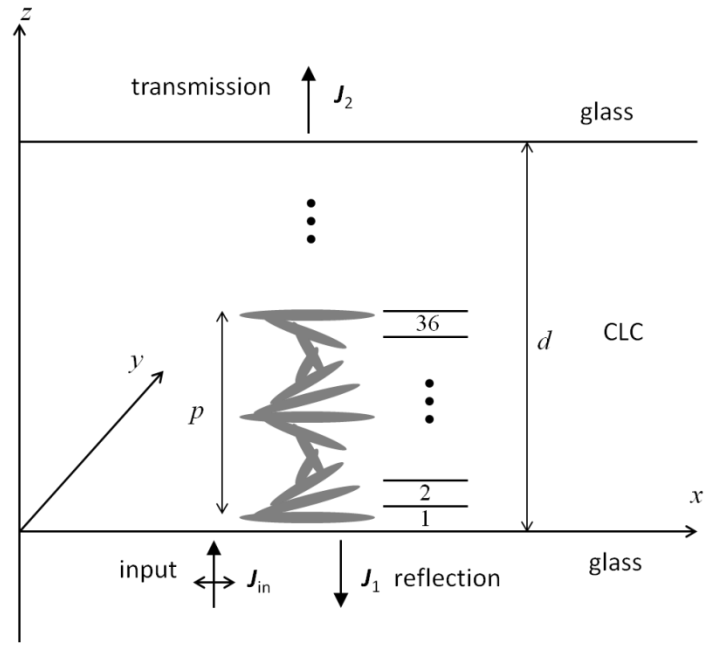

Figure 2.4: Reflection and transmission of a light beam incoming to a CLC layer. The incoming light is linearly polarized along x direction. 36 layers are used for one pitch.

The simulation results of the reflected and transmitted Jones vectors are shown in Figure 2.5. The vectors are normalized and the imaginary part of the first element is set to be zero. It is observed that for the light with wavelength in between 790 nm and 920 nm, the reflected Jones vector is nearly [1 j] (right-handed circular polarization), while the transmitted Jones vector is nearly [1 -j] (left-handed circular polarization). The reflectivity of these two polarizations is also calculated and presented in Figure 2.6. It reveals that right-handed circular polarization (RCP) is reflected back by the right-handed helix CLC within its photonic band gap, while the left-handed circular polarization (LCP) can pass through. Outside of the band gap, the reflection and transmission of other polarization strongly enhance, so the Jones vectors change rapidly with wavelength. The simulation agrees very well with the photonic band theory of the CLC and shows the correct reflection band position.

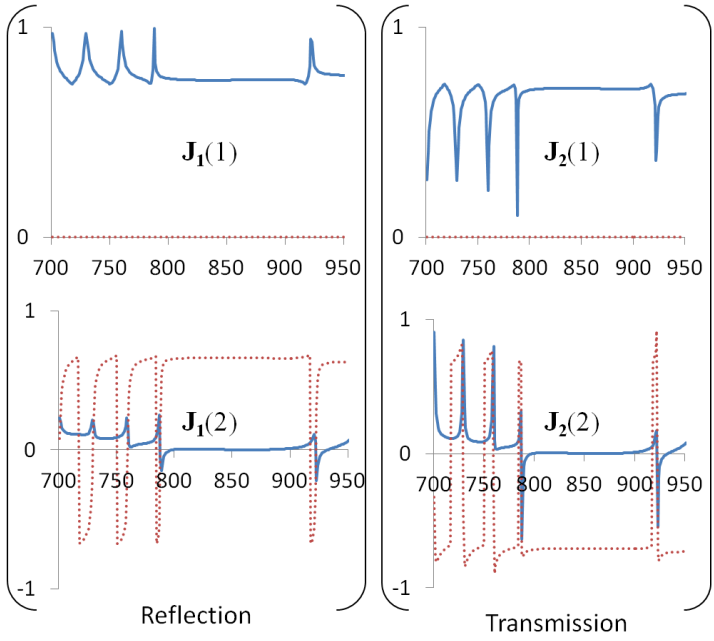

Figure 2.5: Simulated Jones vectors of the output fields from the CLC thin layer at different wavelengths. $\boldsymbol{J_1}(1,2)$ and $\boldsymbol{J_2}(1,2)$ are the Jones vectors of transmitted and reflected fields, respectively. Blue solid line: real part; red dot line: imaginary part. CLC pitch: 530 nm. CLC thickness: 10 μm. Inside the CLC band gap, only circularly polarized lights can be reflected or transmitted. Outside of the CLC band

gap, other polarization can be reflected or transmitted so that Jones vector changes rapidly with wavelength.

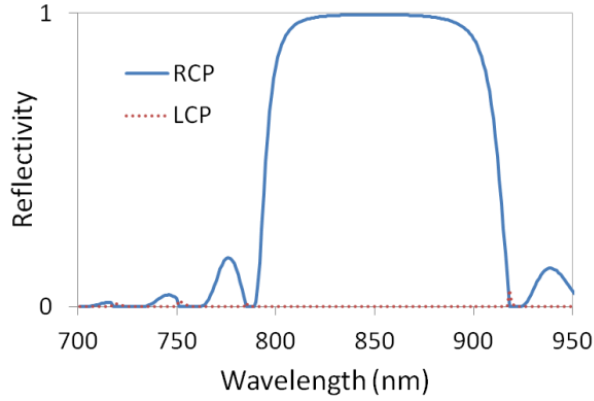

Figure 2.6: Simulated reflectivity of RCP and LCP by the CLC thin layer at different wavelengths. CLC pitch: 530 nm. CLC thickness: 10 μm.

2.2.2 Bare VCSELs

As another simple example, simulation results for bare VCSELs are discussed. The structural parameters of VCSEL, including refractive index and thickness for each layer, are listed in Table 2.1. In realistic cases, the threshold gain and the lasing wavelength for the two orthogonal linearly polarized modes (P_x and P_y) are slightly different. Therefore, one of these two modes is dominant. In our simulation a small anisotropy of 10^{-4} in the refractive index of the VCSEL semiconductor materials between x and y direction is included in the simulations to favor the emission of one of the two linear polarization directions [83]. We predefine this intrinsically dominant polarization as the P_x mode. The lasing threshold for one mode is obtained by increasing the imaginary part of the refractive index of the active layer Im{n} until the round trip gain (RTG) reaches 1 for this mode at a certain resonance wavelength λ_{res}. This threshold condition can be described as

$$\begin{bmatrix} E_{x,round_{trip}} \\ E_{y,round_{trip}} \end{bmatrix} = \boldsymbol{A}^{-}\boldsymbol{A}^{+}\begin{bmatrix} E_{x,0} \\ E_{y,0} \end{bmatrix} = \begin{bmatrix} E_{x,0} \\ E_{y,0} \end{bmatrix} \tag{2.17}$$

Where, $\boldsymbol{A}^-$ and $\boldsymbol{A}^+$ are the reflection matrix defined in Equation 2.8. Then the threshold gain (G_{th}) is calculated by $G_{th} = \frac{4\pi}{\lambda_{res}}\mathrm{Im}\{n\}$. For the P_x mode, the threshold gain that is obtained from the above condition is 2659 cm^{-1}, and this condition is first reached at the wavelength of 849.5 nm, the lasing wavelength. The wavelength dependent RTG in threshold condition is shown in Figure 2.7. Along the VCSEL cavity (z direction), the refractive index and optical intensity in x and y directions are shown in Figure 2.8.

Table 2.1: The materials in the VCSEL structure.

Structure	Material	Refractive index*	Thickness
Bottom/top DBR: 37.5/27 pairs	$Al_{0.12}Ga_{0.88}As$	3.52 - $i10^{-4}$	60.3 nm
	$Al_{0.9}Ga_{0.1}As$	3.11 - $i10^{-4}$	68.3 nm
VCSEL cavity	$Al_{0.3}Ga_{0.7}As$	3.4 - $i10^{-4}$	113 nm
	GaAs (QWs)	3.62 + i Im{n}	24 nm
	$Al_{0.3}Ga_{0.7}As$	3.4 - $i10^{-4}$	113 nm

The VCSEL chips used in this research are commercial products ULM850-SingleMode_OM-v14. *There is an anisotropy of 10^{-4} between x and y directions.

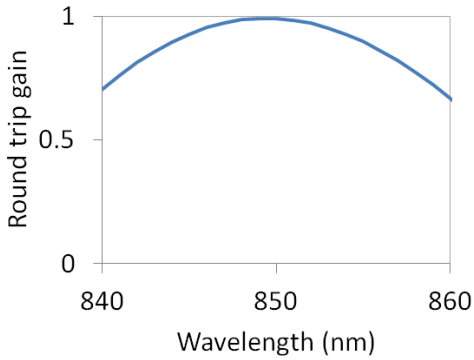

Figure 2.7: P_x mode round trip gain at different wavelengths when the threshold condition for lasing is reached. Threshold gain is 2659 cm^{-1} for the lasing wavelength of 849.5 nm.

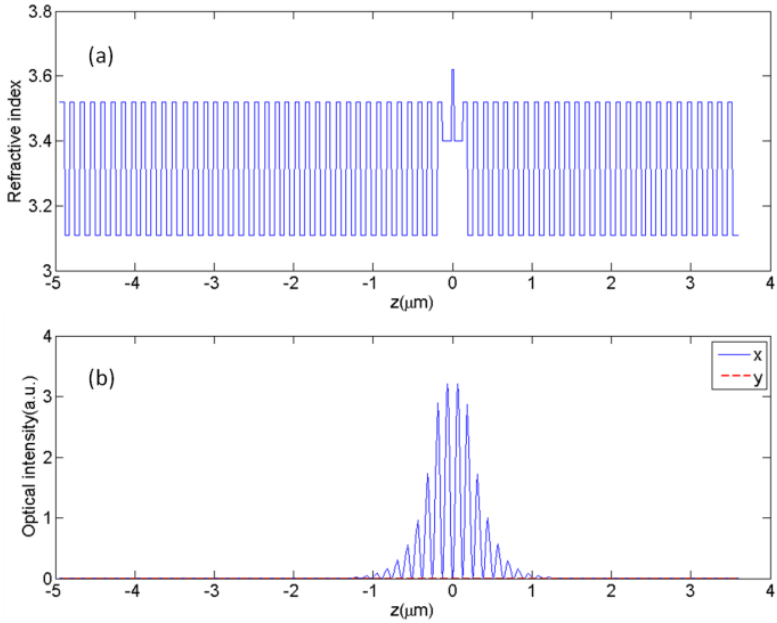

Figure 2.8: Simulations of bare VCSEL in the *z* dimension. (a) Refractive index. (b) Optical intensity in *x* or *y* direction.

Chapter 3

Bare VCSEL with nematic liquid crystal overlay

From chapter 3 to chapter 6, the developed VCSEL devices will be demonstrated in a sequence. This chapter describes the fabrication and characterization of electrically driven VCSEL cells, in which the emitting area is covered with a thin nematic LC layer that can be driven separately. The LC is aligned by photo-alignment. The lasing properties are not fundamentally changed because the LC layer introduces only minor reflections. The LC layer strongly affects the polarization state of the VCSEL emission due to its birefringent properties. It is observed that the polarization state of the laser emission can be controlled by the applied voltage. Besides the polarization control, that will be demonstrated in Section 3.2, also the threshold current, beam profile and wavelength of the output light can be tuned by introducing optical feedback by means of a highly reflective LC layer or by using a dielectric or metallic mirror. These updated functionalities will be discussed in further chapters.

3.1 Integration technology

The VCSEL chips used in this thesis work are purchased from ULM GmbH and the product number is ULM850-SingleMode_OM-v14. The dimensions of this chip are 250 μm × 250 μm × 150 μm. It is a single mode laser with emission wavelength near 850 nm. The threshold current is about 0.5 mA and the maximal operation current is 2 mA with an output power of 0.5 mW.

The two electrodes of the laser chip are separately located on the top and bottom surfaces. Because the aim of our research is to modulate the emission properties of VCSELs, we will use intrinsic single mode devices. Higher output power or higher quality of linear polarization is not required. Other chips which both electrodes are on the same surface are not favorable because the design of the top contact pattern is more complex and the device fabrication becomes more difficult.

A bare VCSEL chip is incorporated in a standard LC cell according to the procedure illustrated in Figure 3.1. Firstly, top and bottom substrates are prepared separately. The top substrate is initially a glass plate coated with a homogeneous thin film of transparent conductor Indium Tin Oxide (ITO) (Figure 3.1a). A pattern with separate square ITO electrodes is formed by lithography (Figure 3.1b). Afterwards, a thin film of photo-alignment layer is spin-coated and dried in the oven (Figure 3.1c). The photo-alignment material SD1 is dissolved in a 1 to 1 volume ratio of ethanol and NMP which is then spin coated. The parameters of spin coating are: speed 3000 rpm, 6 seconds acceleration and deceleration time, 30 seconds running time. The drying temperature is 100˚C and the drying time is 1 minute. Micro-sized conductive spacers which are mixed in UV-curable glue are placed on top of the patterned ITO such that they are on the edge of one separated ITO electrode (Figure 3.1d). The bottom substrate is also a glass plate coated with a homogeneous thin film of ITO (Figure 3.1e). Micro-sized conductive spacers which are mixed in UV-curable glue are placed on top of the bottom substrate (Figure 3.1f). The VCSEL chip is put on the conductive spacers and is gently pressed downward by using a thin glass plate with the same size of the bottom glass substrate placed on top of the chip. So that the spacers beneath the chip form a single layer and the chip surface is parallel to the bottom substrate surface. Then it is exposed to UV light, so that the optical glue is cured and the laser chip is fixed with the bottom substrate (Figure 3.1g). The reason why conductive glue is not used here is that the chip is not easy to be set parallel to the bottom surface due to the nonsolid state of the glue. Afterwards, some non-conductive spacers mixed in UV-curable optical glue, are placed near the edge of the bottom substrate (Figure 3.1h). Their size should be close to but smaller than the sum of the chip thickness and twice the size of the conductive spacers. This is because the top substrate should have contact with the conductive spacers on the top electrode of the chip, and the top substrate should be as parallel to the bottom substrate as possible. Finally, the top substrate is positioned on the bottom substrate to make a full cell (Figure 3.1i). Importantly, the positive

electrode of the VCSEL (square anode pad on the top surface) is well contacted with the conductive spacers on the top substrate, which is achieved by using an accurate positioning system and a microscope. Afterwards, in order to provide alignment of the LC with the photo-alignment polymers, linearly polarized UV light is used in the last step. The polarized UV light also cures the optical glue contacting the anode of the VCSEL and the edge of the full cell. Consequently, all electrical contacts in the cell are fixed in a reliable way. As a result, cells can be operated after a shelf life of three years.

The whole fabrication procedure is implemented in the clean room located in the Technology Park of Ghent University in Zwijnaarde.

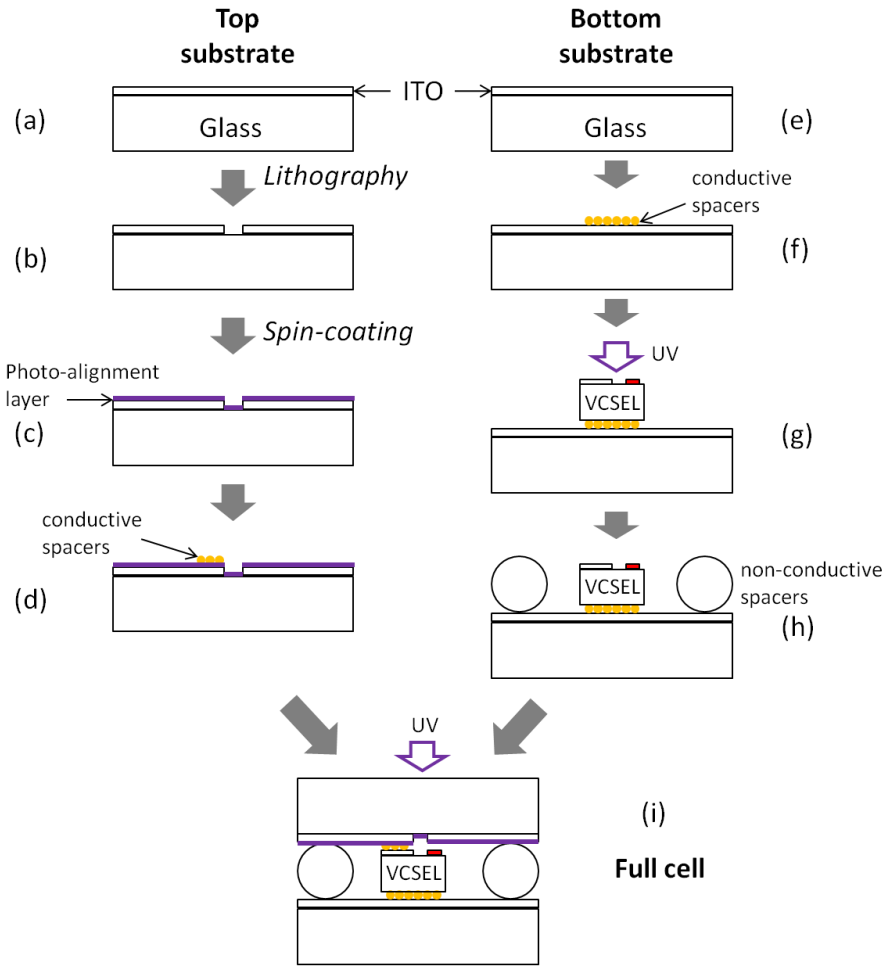

Figure 3.1: Illustration of the technology to fabricate VCSEL cells. (a-d) Processes for the top substrate. (e-h) Processes for the bottom substrate. (i) Full cell after positioning the top substrate on the bottom substrate.

After the cell is fabricated, electrode wires are soldered on the two substrates using an ultra-sonic vibrating soldering device. The LC can be filled in the cell and forms a thin layer between the VCSEL and the top substrate. The side view of the cell and the LC molecules with or without voltage are shown in Figure 3.2. If no voltage is applied across the LC layer, the LC molecules are planar aligned following the orientation of the photo-alignment material (Figure 3.2c). When a voltage is applied, the LC molecules reorient according to the electric field (Figure 3.2d).

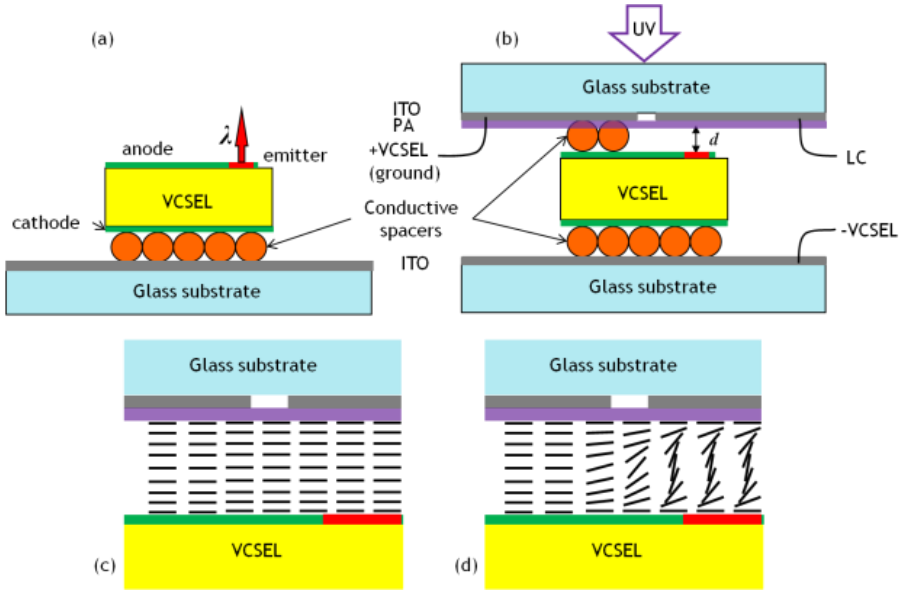

Figure 3.2: Schematic structure of VCSEL cell. (a) and (b) Two fabrication steps. PA: photo alignment layer; d: thickness of the LC overlay. The orientation of LC molecules (c) without and (d) with voltage applied across the LC overlay.

3.1.1 Independent electrodes for VCSEL and liquid crystal

The top ITO layer is patterned by using UV lithography in order to define a contact for the VCSEL anode and another contact for applying a voltage over the LC layer (Figure 3.1b). This pattern is presented more clearly by the top view scheme in Figure 3.3. There are four square pixels of ITO on the top substrate formed by etching the uniform ITO layer using a lithography

mask. The gap between the squares is 4μm. The anode of the VCSEL (the yellow square in the bottom left corner of the VCSEL chip in Figure 3.3) is electrically connected to the bottom left ITO pixel through micro-sized gold coated silica spacers embedded in UV cured optical glue. The diameter of these balls is 30 μm ± 0.1 μm for the results in this chapter. The thickness of the LC overlay is determined by the diameter of these spacers. However, in the beginning of this research, the technology to set VCSEL chip parallel to the bottom substrate was not perfect and the LC thickness is thinner due to a tilt of the VCSEL chip. This problem has been solved in later chapters. The VCSEL emitter (red circle in the top right corner of VCSEL chip shown in Figure 3.3) is just beneath the top right ITO pixel. The electrode connections are made by soldering a wire on the corresponding ITO nodes near the edge of the substrate.

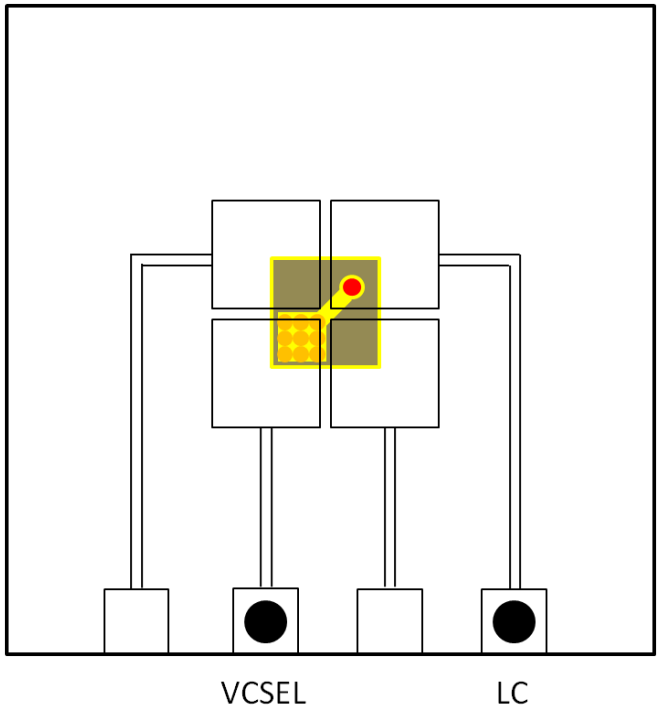

Figure 3.3: Top view of the VCSEL cell. The patterned ITO is shown by black lines. The VCSEL chip is shown in color: anode is yellow, emitter is red. Conductive spacers are shown by orange circles. Two soldered electrodes for VCSEL and LC are shown by black circles.

3.1.2 Defining the LC alignment using photo-alignment technology

A thin azo dye SD1 layer is spin coated on the top substrate which acts as a photo-alignment layer in order to align LC molecules [28]. In the first step (Figure 3.2(a)), the polarization state of the emission of the VCSEL is measured as it is important to align the LC at the correct angle with respect to this direction. In the second step, the cell is exposed to linearly polarized UV light (Figure 3.2(b)). The orientation of the SD1 molecules tends to be perpendicular to the UV polarization direction and this provides planar alignment of the LC director (Figure 3.2(c)). The LC alignment is set to 45 ° with respect to the original polarization direction of the VCSEL emission in order to obtain optimal polarization control of the emitted light. The LC director orientation is indicated in Figure 3.2(d) when voltage is applied across the LC overlay. In Figure 3.4, optical microscope pictures of the VCSEL inside the cell are shown. The pictures are taken in reflection mode. Figure 3.4(A) shows the cell before filling with LC. The conductive spacers, the outlines of the electrodes for LC on the top glass plate and the dominant polarization direction of the VCSEL emission (from the circular area) are indicated. After the LC (E7 from Merck) is filled in the cell, it is observed through crossed polarizers. In Figure 3.4 the images B, C and D show the reflection for different orientations of the device between crossed polarizer and analyzer. The fact that images B and D are darker in the field of interest (near the circular emission region) indicates that the LC overlay is indeed homogeneously oriented in a planar orientation. In the pictures, the metal electrodes always appear much brighter than the chip area and this is due to the high reflectivity of the metal lane. The area to the left of the emitting region does not have the correct LC alignment because there is some cured optical glue attached to the top glass surface. Due to the optically isotropic property of the optical glue, the region filled with glue (over the contact pad) remains dark in the images B, C and D.

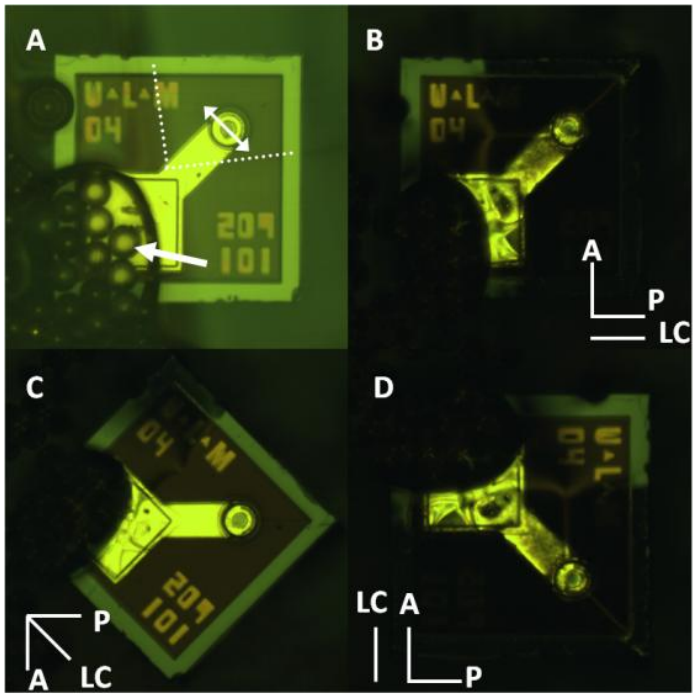

Figure 3.4: Polarization microscope images of VCSEL cell (a) before LC is filled in (without analyzer) and (b)–(d) after LC is filled in. Gold-coated spacers are indicated by an arrow. Dominant polarization direction is shown by a double arrow over the emitter region. Electrode for the LC layer over the emitter is indicated by dotted lines. Polarizer (P), analyzer (A), and LC alignment (LC) directions are also indicated.

3.2 Polarization characteristics

The optical setup of Figure 3.5 is designed to characterize the optical properties of the light emitted from the VCSEL cell. A laser beam propagates along the *z* direction. The quarter wave plate (with azimuth of the fast axis α) and the linear polarizer with azimuth φ are parallel to the *x*-*y* plane with reference 0 ° parallel to the x axis, which is chosen to be parallel with the dominant polarization direction of the VCSEL emission (indicated by the double arrow in Figure 3.4). Two convex lenses are used to transform the emission of the VCSEL into a parallel beam and to focus the transmitted beam onto a photo-detector, which is connected to a calibrated power meter.

The VCSEL cell is temperature stabilized at 25 ℃ using a temperature controller.

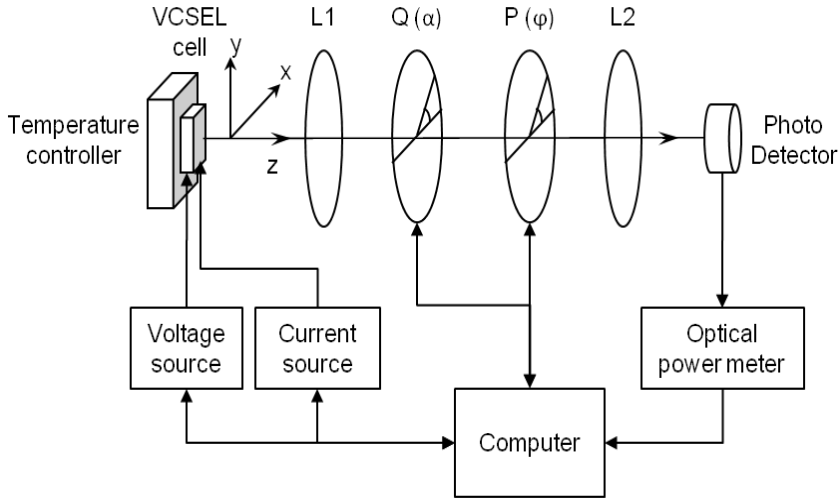

Figure 3.5: Optical setup for the VCSEL cell measurement. L1 and L2: convex lenses. Q: quarter wave plate with azimuth α. P: linear polarizer with azimuth φ.

3.2.1 Measurement of polarization state

Based on the method explained in Appendix A, the polarization state of the VCSEL emission without LC overlay is measured using the quarter wave plate (single order for the emission wavelength of the VCSEL) followed by one linear infrared polarizer. The transmitted intensity measurements $P(\alpha, \varphi)$ for different values of the azimuth of the quarter wave plate (α) and the azimuth of the linear polarizer (φ) are shown in Table 3.1. The Stokes parameter S_0 representing the total intensity is normalized to 1. The Stokes parameters S_1, S_2 and S_3 are obtained using $P(0,0)$, $P(90,90)$, $P(45,45)$, $P(135,135)$, $P(0,45)$ and $P(0,135)$ following the methods described in [84]:

$$S_1 = \frac{P(0,0)-P(90,90)}{P(0,0)+P(90,90)} \quad (3.1)$$

$$S_2 = \frac{P(45,45)-P(135,135)}{P(0,0)+P(90,90)} \quad (3.2)$$

$$S_3 = \frac{P(0,45)-P(0,135)}{P(0,0)+P(90,90)} \quad (3.3)$$

The degree of polarization p is defined as $p^2 = S_1^2 + S_2^2 + S_3^2$. The ellipticity angle χ is calculated by $\cos 2\chi = S1/p$ and the result is 13.8 °. As expected, we find that after the quarter wave plate with azimuth 0 °, the light is practically linearly polarized along the azimuth angle φ = 14 °. We can conclude that the VCSEL emission is elliptically polarized, with a high polarization degree, with a ratio of 14.3 between the powers along the long and short axis of the elliptical polarization $P(0,0)/P(90,90)$. This ratio varies between different samples of the same type of VCSEL.

Table 3.1: Transmission measurements and polarization state of the VCSEL emission before LC filing.

α(°)	φ(°)	P(µW)	S_0	S_1	S_2	S_3	p
0	0	82.15	1	0.869	0.097	0.464	0.990
90	90	5.75					
45	45	48.60					
135	135	40.08					
0	45	64.35					
0	135	23.59					

The electro-optical characteristics are investigated by measuring the P-I (optical power versus VCSEL current) curve, setting the linear polarizer at φ=0 ° and 90 °, respectively (without the quarter wave plate) (Figure 3.6). Measurements are carried out before LC filling and after filling with LC (E7 from Merck). An AC voltage can be applied over the LC overlay with a frequency of 1 kHz in order to avoid the influence of ion movement inside the LC [85]. We find that for the empty cell, the polarization ellipse is aligned along 0 °(first graph in Figure 3.6). After filing with LC, the azimuth of the polarization ellipse changes to 90 ° if no voltage is applied (second

graph in Figure 3.6) and changes back to 0 ° if 3V is applied (third graph in Figure 3.6).

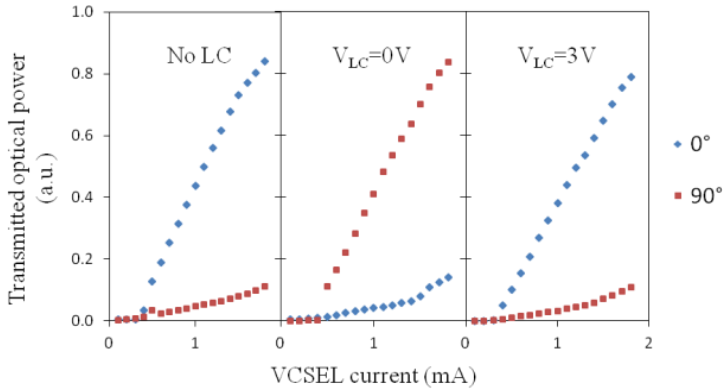

Figure 3.6: Transmitted optical power as a function of the VCSEL current. The polarizer is set to two directions, φ = 0 ° or φ = 90 °. From left to right: no LC filled in the cell, no voltage applied over the LC, and 3 V AC (1 kHz) applied over the LC.

Output optical power as a function of the voltage applied over the LC layer have been measured and shown in Figure 3.7. The measurement is done by setting the linear polarizer at its azimuth angle φ = 0 ° and 90 ° without quarter wave plate. The VCSEL is driven at a constant current of 1.6 mA and the voltage applied over the LC overlay is increased from 0 to 4 V. We find that the polarization state changes continuously with increasing LC voltage between 0.5 V (threshold) and 3 V. For voltages lower than the LC-threshold, the polarization state does not change appreciably. For voltages above the saturation voltage (3 V) the polarization state changes only a little. In between, the polarization state changes continuously, becoming circular for certain voltages. A similar measurement of the sample with a thinner LC layer (spacer size is 10 µm) is also shown in Figure 3.7. By comparing these two measurements, we found that the output optical power of the sample with thicker LC layer shows more periods. The reason is that the thicker the LC layer is, the larger the phase retardation is. This is explained in Equation 1.7 in the section 1.2.

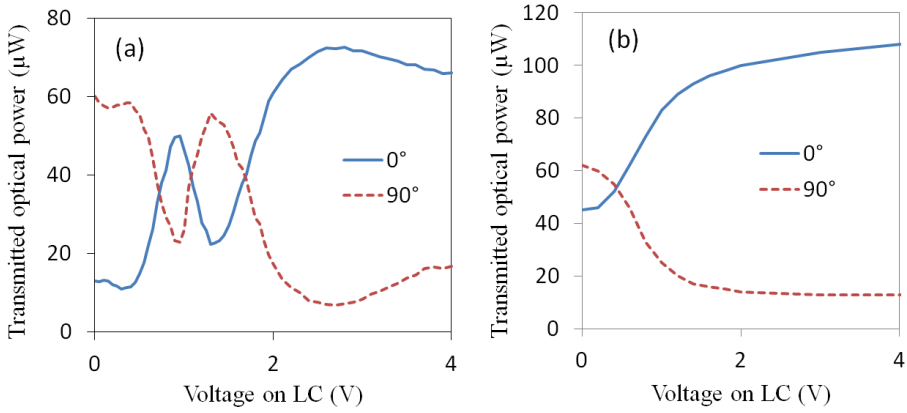

Figure 3.7: Measured output optical power at polarizer azimuth angle of 0 ° and 90 ° as a function of the voltage applied over the LC layer. (a) Spacer size is 30 μm. (b) Spacer size is 10 μm.

3.2.2 Comparison of measurements and theoretical simulations

In order to understand the dependence of the polarization state on the voltage applied over the LC overlay, theoretical simulations have been made to compare with the measurements. The simulated transmission in both x and y directions (T_x and T_y) is shown in Figure 3.8. The transmission is calculated using Equation 3.4 and Equation 1.9.

$$T_x = \frac{\left|A_x^{out}\right|^2}{\left|A_x^{in}\right|^2 + \left|A_y^{in}\right|^2}, T_y = 1 - T_{x.} \qquad (3.4)$$

The simulation is done based on Jones matrix formalism [84] and using the parameters for LC E7 found in [37, 86] for a thickness of 6μm. For comparison, the experimental results are also shown in Figure 3.8. It is observed that the measured emission has a smaller contrast between x and y directions than the simulation, especially in the voltage range of 1 V to 2 V. In order to explain the difference between the experiment and the simulation (especially the lower contrast near the threshold voltage in the experiment), we have added measurements of the degree of polarization for two situations: p2 is measured without an aperture, while p1 is measured with an

aperture placed between the first lens and the quarter wave plate. For the measurement with aperture, only the center part of the beam is used and about one fourth of the total power is passing through.

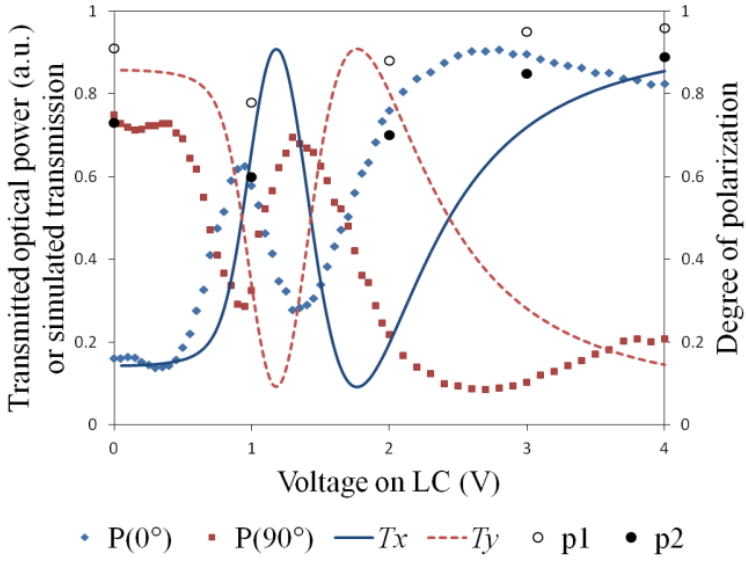

Figure 3.8: Transmitted optical power P, simulated transmission *T*, and the degree of polarization p as a function of the alternating voltage amplitude (1 kHz) applied over the LC layer. For P, the polarizer is set to two directions, $\varphi = 0\,°$ (x-axis) or $\varphi = 90\,°$ (y-axis). The degree of polarization p1 is measured with an aperture and p2 is measured without aperture. The operating current of VCSEL is 1.6mA.

Besides the VCSEL performance, the contrast ratio between P(0°) and P(90°) is limited by scattering of light in the LC as can be seen from the measurement of the degree of polarization. Typically, the amount of scattering is higher for voltages near the threshold voltage. This problem can be resolved effectively by using a thinner LC layer. The depolarization effect is not the only reason for a lower contrast, because the degree of polarization is higher when we measure with an aperture. For the VCSEL that we use, the light is emitted within a cone with half angle 13°. Rays that are emitted under a larger angle will see a larger retardation effect (demonstrated in Figure 3.9). Hence, the polarization state of light emitted under large angles is different from light in the beam center. Because we measure the integrated power to determine the Stokes parameters and the degree of polarization, a

change of polarization state for different emitted angles results in a decrease of the measured degree of polarization. To illustrate the incident angle dependent transmission, we simulate the *x* component of the polarization as a function of incident angle (θ, φ), using a model that is similar to the extended Jones formalism [13]. The simulation is done using the same parameters as Figure 3.8, but for different incident angles (θ changes from 0 to 12 °, φ changes from 0 to 360 °). The simulation results are shown as contours in Figure 3.10 (radius and polar angle correspond to θ and φ, respectively). It shows that the transmission at V_{LC} = 1.2 V and 1.8 V (peaks near the threshold voltage of the LC) varies more with incident angles than that at V_{LC} = 0V and 5V. The weighted average of the transmission can be calculated as a Gaussian beam with FWHM = 13 °, it is smaller than the value of normal incidence at V_{LC} = 1.2 V and higher at V_{LC} = 1.8 V. But, this difference is much less for V_{LC} = 0 V and 5 V. This can only partially explain the discrepancy in extinction (contrast ratio) between theory and experiment, which means that other effects such as scattering in the liquid crystal or inhomogeneous switching play a role. Thus a thinner LC layer and a small aperture may be useful ways to enhance the contrast ratio.

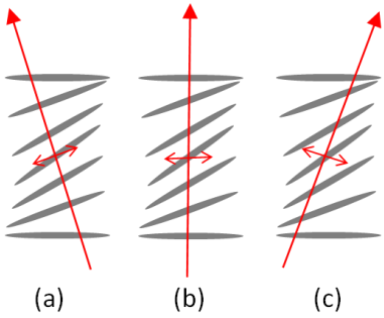

Figure 3.9: Propagation of light beams in the LC layer with different incident angles: θ =12 °, φ =135 ° (a); θ = φ = 0 ° (b); θ =12 °, φ =45 ° (c). The LC director aligns at φ = 45 °. The polarization direction of the light is indicated by the double arrow.

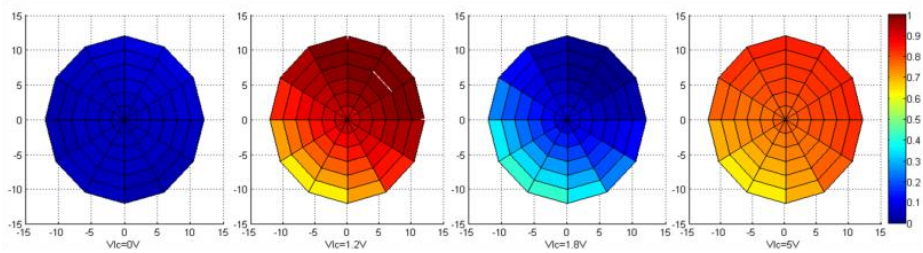

Figure 3.10: Simulated transmission in x direction as a function of incident angle (θ, φ). From left to right: voltage applied across LC layer 0 V, 1.2 V, 1.8 V and 5 V.

Chapter 4

Chiral liquid crystal as an external reflector

In the previous chapter, the technique to integrate a VCSEL chip into a LC cell is demonstrated. Based on this technology, an optical feedback to the VCSEL is now introduced by using the liquid crystal layer as an external mirror to the VCSEL. In this chapter, chiral liquid crystals (CLCs) cover the top of the VCSEL and one circular polarization mode can be effectively reflected back to the laser. The emission properties of this coupled CLC-VCSEL device can be controlled by temperature.

4.1 Photonic band-gap of chiral liquid crystal

CLC is a special type of nematic LC, which can be obtained by dissolving a certain type of chiral dopant into a non-chiral nematic LC host. For all results in this chapter, BDH1305 (from Merck) is used as the chiral dopant. The nematic LC can be E7 or 5CB. CLC exhibits a periodic helical arrangement of the LC molecules with a certain pitch (see Figure 1.10). The pitch is determined by both the LC and the concentration of chiral dopant. The higher the dopant concentration, the shorter is the CLC pitch. Similar to the electronic energy bands in a periodic crystal lattice, a photonic band is provided by the CLC helix structure for the transmitted light which has the same handedness of circular polarization. When the electric field vector of the propagating light can follow the molecule orientation in the CLC, the transmission is forbidden. Therefore, this structure can selectively reflect a

certain type of circular polarization (with the same handedness of the CLC helix), which can provide an optical feedback to the VCSEL. The handedness of the CLC depends on both the type of chiral dopant and the type of LC solvent.

4.1.1 Selective reflection of one circular polarization mode

To confirm the photonic band-gap in a CLC material and to obtain information about the handedness and the band position, measurements of transmission spectra for two different types of circular polarization are performed. Circularly polarized light is incident onto a thin layer of 5CB LC host CLC which is filled in a cell with alignment on both substrates. The circularly polarized light is produced by a linear polarizer (broad band Vis-IR) followed by a quarter wave plate (zero-order @ 850 nm). If a linearly polarized light of 850 nm wavelength is entering the quarter wave plate, the polarization along the slow axis is retarded by a quarter-wave or 90˚ in phase compared to that along the fast axis. This optical setup is shown in Figure 4.1. The measured transmission spectra of both right-handed circular polarization (RCP) and left-handed circular polarization (LCP) are displayed in Figure 4.2. The chiral dopant concentration is 3.2 wt% and the cell thickness is 6.8 μm. It is observed that the RCP can be effectively reflected for the wavelength range between 780 nm and 870 nm (band edges). This confirms that the helix structure in the CLC is right-handed. Measurements with other types of nematic LCs, which are not shown here, indicate that the CLC in these nematic LCs with BDH1305 as chiral dopant all have a right-handed helix. From theoretical considerations, the reflectivity should be close to unity inside the reflection band for RCP. The measurement results however show a transmission of a few percent for RCP. This is probably due to scattering of the spacers in the cell located in the detection region. This reflection characteristic of the CLC can be applied to the VCSEL device as an extra mirror which may result in a strong change of the emission properties. In fact, the research results in this chapter (section 4.2 to 4.4) indicate that the CLC-VCSEL system is a strongly coupled system with a complex polarization behavior.

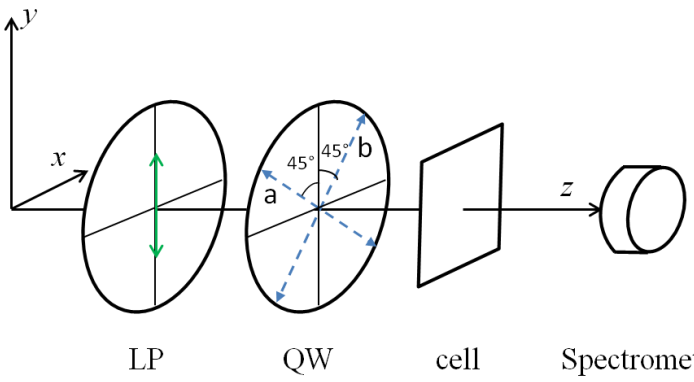

Figure 4.1: Optical setup for the transmission measurement. A linear polarizer (LP) is placed before a quarter wave plate (QW). The transmission axis of the LP is along the y axis and is represented by the green double arrow. The fast axis of the QW for two cases (a or b) is shown by the blue double arrows. (a) A right-handed circular polarization (RCP) is generated after the QW; (b) left-handed circular polarization (LCP) is generated after the QW.

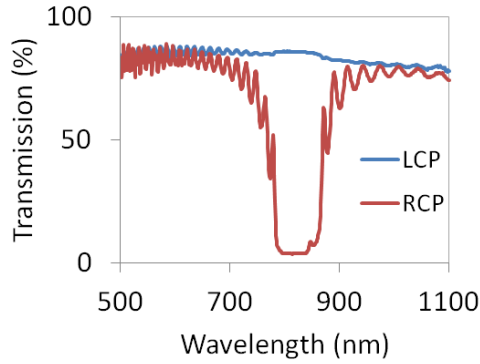

Figure 4.2: Transmission spectra of circularly polarized incidence for 5CB host CLC thin layer. *Red curve*: right-handed circular polarization (RCP); *blue curve*: left-handed circular polarization (LCP). The chiral dopant concentration is 3.2 wt%. CLC thickness: 6.8 μm. Measurement is performed at a temperature of 25°C.

4.1.2 Chiral dopant concentration-dependent pitch and band position

The pitch of the CLC helix depends on the concentration of the chiral dopant dissolved in the nematic LC. The pitch is inversely proportional to the concentration, which can be described as:

$$p = \frac{A}{concentration} \tag{4.1}$$

The parameter *A* is a LC specific constant which can be determined by measurements of a series of transmission spectra for different concentrations. Pitch *p* has a unit of nm, concentration has a unit of weight percentage (wt%), and *A* has a unit of nm•wt%. Such a series is shown in Figure 4.3. The pitch is related to the stop-band edges as presented in Equation 4.2. Both the left and right band edges can be read from the transmission spectra, together with the known refractive index of the corresponding nematic LC, the pitch *p* can be estimated for a certain concentration of chiral dopant. Using Equation 4.1, parameter *A* can be calculated by fitting the results for different concentrations, which is shown in Figure 4.4. Therefore, the band position can be designed by choosing a proper concentration, as long as *A* is known.

$$\begin{aligned} \lambda_{left\ bandedge} &= p * n_o \\ \lambda_{right\ bandedge} &= p * n_e \end{aligned} \tag{4.2}$$

In order to introduce optical feedback to the VCSEL, the reflection band of the CLC should be suitably designed so that the emission wavelength of VCSEL is just located inside the band. In this way, RCP light can be effectively reflected back to the VCSEL by the CLC layer. The CLC layer then is an external mirror. For the 5CB host CLC, 3.2 wt% concentration of BDH1305 is chosen for this reason. For the E7 host CLC, the proper concentration is 3.6 wt%.

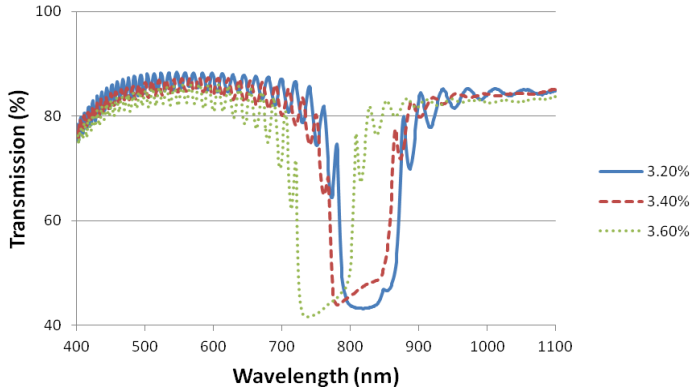

Figure 4.3: Transmission spectra of non-polarized incidence for 5CB host CLC thin layer. Different concentrations of chiral dopant are shown. CLC thickness: 6.8 µm. Measurement is performed at a temperature of 25 °C.

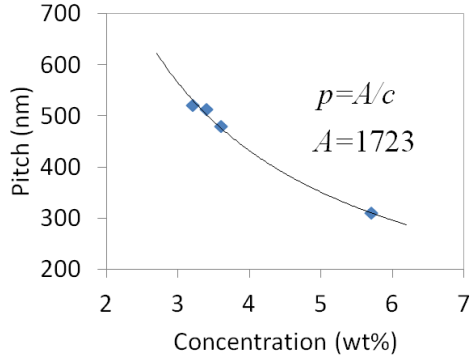

Figure 4.4: Measured result of the pitch of 5CB host CLC as a function of the concentration of chiral dopant. The fitting parameter A is 1723 nm·wt%.

4.1.3 Temperature dependent reflectivity

The photonic band character arises from the periodicity in the CLC. When the temperature is increased and is higher than the clearing point of the host nematic LC, the reflection band of the CLC will disappear because the host LC changes from nematic phase to isotropic phase. To confirm this behavior, measurements of the transmission spectra at different temperatures are performed. In Figure 4.5, transmission spectra of 5CB host CLC are shown

for temperatures between 25 °C and 34 °C. It is observed that the reflection band gradually disappears with increasing temperature. The band structure completely disappears at temperatures higher than 33 °C. This phenomenon can be well explained by the phase transition of 5CB: pure 5CB transfers from nematic phase to isotropic phase at its clearing point of 35 °C. The small mismatch between the measurement and the expected transition temperature is due to the fact that the mixture of chiral dopant slightly changes the basic characteristics of 5CB. In contrast, pure E7 has a much broader nematic range which is from -10 °C to 60.5 °C. Therefore, the reflection band of E7 host CLC is expected to maintain until the temperature is higher than about 60 °C.

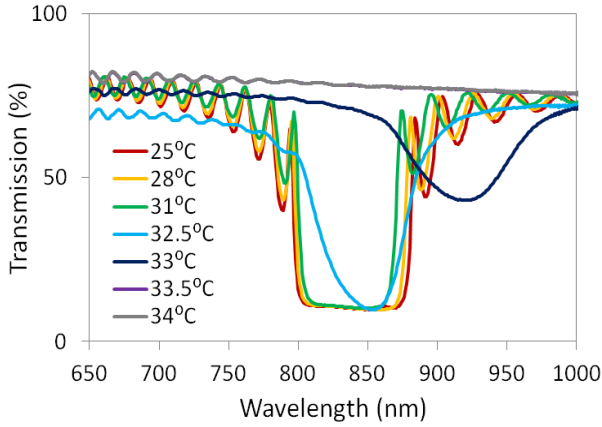

Figure 4.5: Transmission spectra of RCP incidence for 5CB host CLC thin layer. The chiral dopant concentration is 3.2%. CLC thickness: 6.8 μm. Different measurement temperatures are shown.

4.2 CLC-VCSEL device

The different CLC mixtures based on 5CB and E7 as discussed in the previous section are used now as top cladding for VCSELs. In these devices, the top glass substrate is covered with a uniform transparent conductor ITO and a photo-alignment layer, while the bottom glass substrate is covered with only a layer of ITO. The anode and cathode of the VCSEL are electrically connected to the top and bottom ITO, respectively, through micro sized gold coated silica spheres embedded in UV cured optical glue.

The side view of the device is schematically shown in Figure 4.6. As there is no separate electrode for the LC, there is no voltage drop across the CLC layer enclosed between the VCSEL output facet and the ITO layer of the upper glass substrate and we don't expect any influence of the driving current on the LC behavior. The thickness of the CLC overlay is 10 μm.

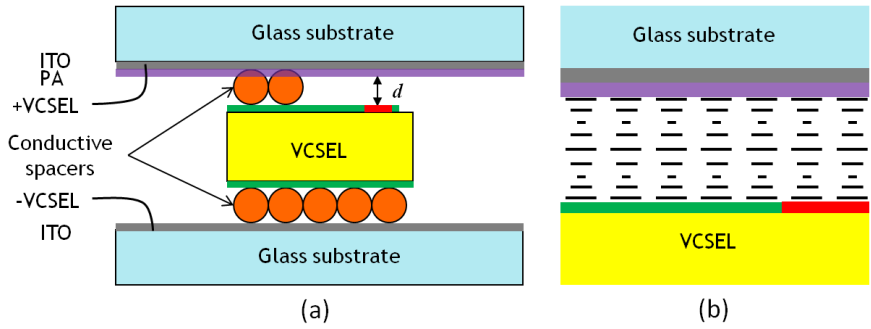

Figure 4.6: (a) Schematic side view of the CLC-VCSEL device. (b) The CLC layer between the VCSEL and top substrate.

Microscope pictures of the CLC-VCSEL cell before and after filling with 5CB host CLC are shown in Figure 4.7. It is observed in the *right* picture that a few domains form in the CLC layer. Above the emitter region no domain walls can be distinguished, meaning that there is only a single domain above the emitting region. This single domain makes sure that all LC molecules have a homogeneous helical orientation above the emitter, which is critical for realizing a predictable optical feedback to the VCSEL cavity.

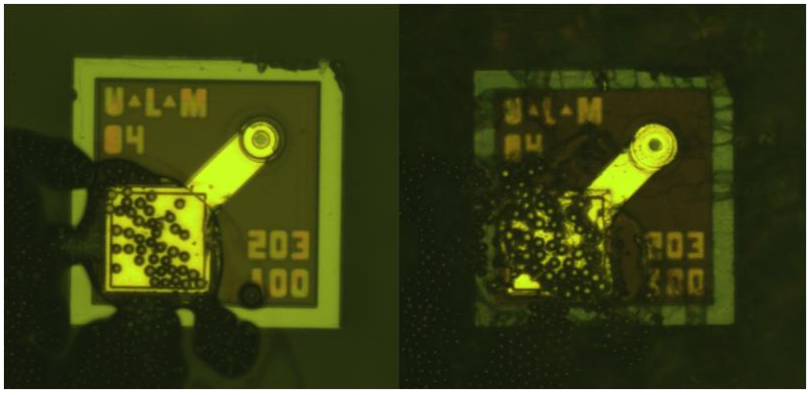

Figure 4.7: The top-view reflection microscopic pictures of the CLC-VCSEL device. *Left*: no CLC is present; *right*: 5CB host CLC is present.

4.3 Measurements of polarization state

The polarization state of the emission of the stand-alone VCSEL (before CLC is filled in the cell) and CLC-VCSEL (after CLC is filled in) is measured at different temperatures using a fixed driving current of 1.6 mA which is well above the threshold current. Figure 4.8(a) compares the optical power as a function of the orientation of the linear polarizer for the stand-alone VCSEL, the CLC-VCSEL and a VCSEL followed by a separated CLC layer at 25 ℃ (the experimental setup is the same with the one presented in Figure 3.5 without quarter wave plate). In the latter case, the reflection from the CLC layer is not coupled back into the VCSEL's active region. It is observed that both the CLC-VCSEL and a VCSEL followed by a separate CLC layer emit circularly polarized light. But the latter's optical intensity is drastically lower than the one from the CLC-VCSEL, because one half of the intensity of the VCSEL emission is lost by reflection of the CLC layer which cannot coupled back into the VCSEL. In contrast, the CLC-VCSEL has an even higher total optical power than the stand-alone VCSEL for the same driving current. This phenomenon will be further discussed in a later section concerning the lasing threshold (see e.g. Figure 4.11a and 4.12b). This phenomenon indicates that the CLC in the CLC-VCSEL provides effective optical feedback by reflecting one circular polarization mode back to the VCSEL. All Stokes parameters are extracted from optical power measurements for different orientations of the quarter wave plate and the linear polarizer according to the procedure in [75]. The results are shown in Figure 4.8(b).

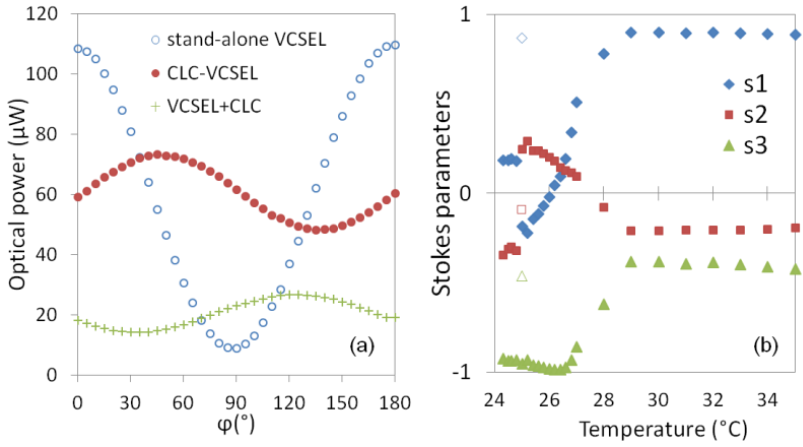

Figure 4.8: (a) Optical power of a stand-alone VCSEL, a 5CB based CLC-VCSEL and a stand-alone VCSEL followed by a separated CLC layer as a function of the azimuth of the linear polarizer P at 25 °C. (b) The Stokes parameters of the emission at different temperatures (solid dots: 5CB based CLC-VCSEL, empty dots: stand-alone VCSEL). VCSEL driving current is 1.6 mA.

4.3.1 Degree of polarization

The polarization states of both stand-alone VCSEL and CLC-VCSEL emission are quantified by the Stokes parameters, which indicate the type of polarization and the degree of polarization. As explained in Appendix A, linear polarization is represented by Stokes parameter S_1 or S_2, while circular polarization corresponds to Stokes parameter S_3 (plus one for RCP and minus one for LCP). Figure 4.8(b) shows clearly the degree of polarization for the emission of both stand-alone VCSEL and CLC-VCSEL. The emission of the stand-alone VCSEL is elliptically polarized, but with one axis of the ellipse being much smaller than the other one. In other words the emission is almost linearly polarized. Noteworthy is the fact that the degree of circular polarization (represented by the Stokes parameter S_3) at lower temperatures reaches a higher value than the degree of linear polarization (represented by $\sqrt{{s_1}^2 + {s_2}^2}$) at higher temperatures. For instance, S_3 is -0.984 at a temperature of 26° C, while $\sqrt{{s_1}^2 + {s_2}^2}$ is 0.856 at temperature of 30 °C. This means that the CLC layer can be used to increase the purity of the polarization state of the VCSEL.

4.3.2 Thermally switchable polarization between linear and circular

Below 27 °C the emission of the CLC-VCSEL is very close to left-handed circular polarization. In contrast, the polarization at temperatures higher than 29 °C is close to linear polarization. This transition is attributed to the transition of the nematic to the isotropic phase of the liquid crystal. It is noted that this transition temperature is lower than the temperature for which the reflection band disappears for 5CB host CLC which is 33 °C shown in the measurements in Figure 4.5. We attribute this difference to a difference between the temperature displayed on the temperature controller and the real temperature in the CLC layer due to the local heating effect of the electrical pumping of the VCSEL. This local temperature difference can be 2 °C to 5 °C depending on the driving current. This is confirmed by the threshold current and spectral measurements that will be discussed later in this section. When the CLC is in the isotropic phase, the CLC does not affect the emission of the VCSEL and the polarization corresponds with the standalone VCSEL (presented by empty markers in Figure 4.8(b)), which remains close to linear polarization at different temperatures.

4.3.3 Simulations

To understand and predict the emission properties of the CLC-VCSEL device, theoretical simulations of the electric fields inside the system are performed using the plane wave expansion method described in chapter 2. The threshold is calculated by increasing the optical gain of the active region until the roundtrip gain reaches one. For this threshold gain, the electric field vectors in each layer along the *z* direction are calculated. The simulation results are presented in Figure 4.9. The total optical intensity along the x ($|E_x|^2$) and the y ($|E_y|^2$) axis is presented in Figure 4.9(a) and (b). The phase difference between the two electric components propagating towards positive z direction, Φ_x - Φ_y, is shown in Figure 4.9(c). The propagating fields towards positive and negative z direction are separately presented in Figure 4.9(d) and (e). The CLC-VCSEL emits left-handed circularly polarized light which is concluded from the amplitude and phase difference shown in Figure 4.9(b) and (c). The calculated Stokes parameter S_3 of the outgoing light is -0.995. The contrast between x and y electric fields inside the VCSEL is lower than for a stand-alone VCSEL which indicates that the CLC and VCSEL are strongly coupled and form a new system. It is noted that the optical reflection provided by the CLC overlay is comparable with

the reflection by the bottom DBR in the VCSEL which means that the CLC layer provides an effective optical feedback. Since the reflectivity is selectively increased it can be understood that the circularly polarized emission from the CLC-VCSEL results in a lower threshold compared to the standalone VCSEL [87]. Indeed the simulation shows that the CLC-VCSEL has 12.8% lower threshold gain than the stand-alone VCSEL which corresponds with the measurement results. Important to note is that only the right circularly polarized wave is reflected by the CLC layer. The left circularly polarized wave can propagate through this layer. Intuitively one might expect that the whole device will start lasing in the right circular polarization as this polarization experiences a larger reflection from the top DBR and CLC layer. However, this does not occur, because a right (left) circularly polarized wave is transformed into a left (right) circularly polarized wave when reflected on a metallic or dielectric mirror. Only for reflection onto a CLC layer the handedness of the circular polarization is preserved. The transformation of the handedness by the bottom DBR stack is the reason why the behavior of the electric field components in Figure 4.9(b), (d) and (e) is so complicated. Instead of decomposing the field along *x* and *y*, it is interesting to decompose the electric fields into left and right circularly polarized (LCP and RCP) modes. The fields for left and right circularly polarized modes, that are propagating in the positive and negative *z* direction, are presented in Figure 4.10(a) and (b). Inside the VCSEL the light is mainly linearly polarized along the x-axis, which leads to equal amounts of LCP and RCP. Inside the CLC RCP light cannot propagate and the evanescent field decreases exponentially in the z-direction. The slope of the exponential decay in Figure 4.10(b) can be analytically calculated based on the theory in [88] and the material parameters of the CLC. The slope estimated from Figure 4.10(b) corresponds to the logarithm of the intensity of RCP light. For a sufficiently large value of the CLC thickness (larger than 3 μm), the intensity of RCP light decreases exponentially with z:

$$I \propto e^{-2sz} \tag{4.3}$$

Where $s^2 = \kappa^2 - (\frac{\Delta k}{2})^2$, $\kappa = \frac{\pi}{\lambda}\frac{{n_e}^2-{n_o}^2}{\sqrt{{n_e}^2+{n_o}^2}}$, $\Delta k = \frac{4\pi}{\lambda}\sqrt{\frac{{n_e}^2+{n_o}^2}{2}} - \frac{4\pi}{p}$. n_e and n_o are the refractive index of the host LC material, λ is the wavelength and p is the pitch of CLC. Using the same values of n_e, n_o, λ and p as in the simulation, we get the slope of $\log I$, which is -2s, from Equation 4.3. It

agrees with the value of the slope calculated from Figure 4.10(b). It is clear from this analysis that practically all of the RCP light is reflected back into the VCSEL.

Furthermore, the transverse optical power distribution at the output facet of the CLC-VCSEL can be simulated using a three dimensional simulation model (see Figure 5 in [76]). Compared to the bare VCSEL, the size of the lasing spot of the CLC-VCSEL is slightly smaller. This indicates that the laser beam of the CLC-VCSEL has a lower divergence than the bare VCSEL.

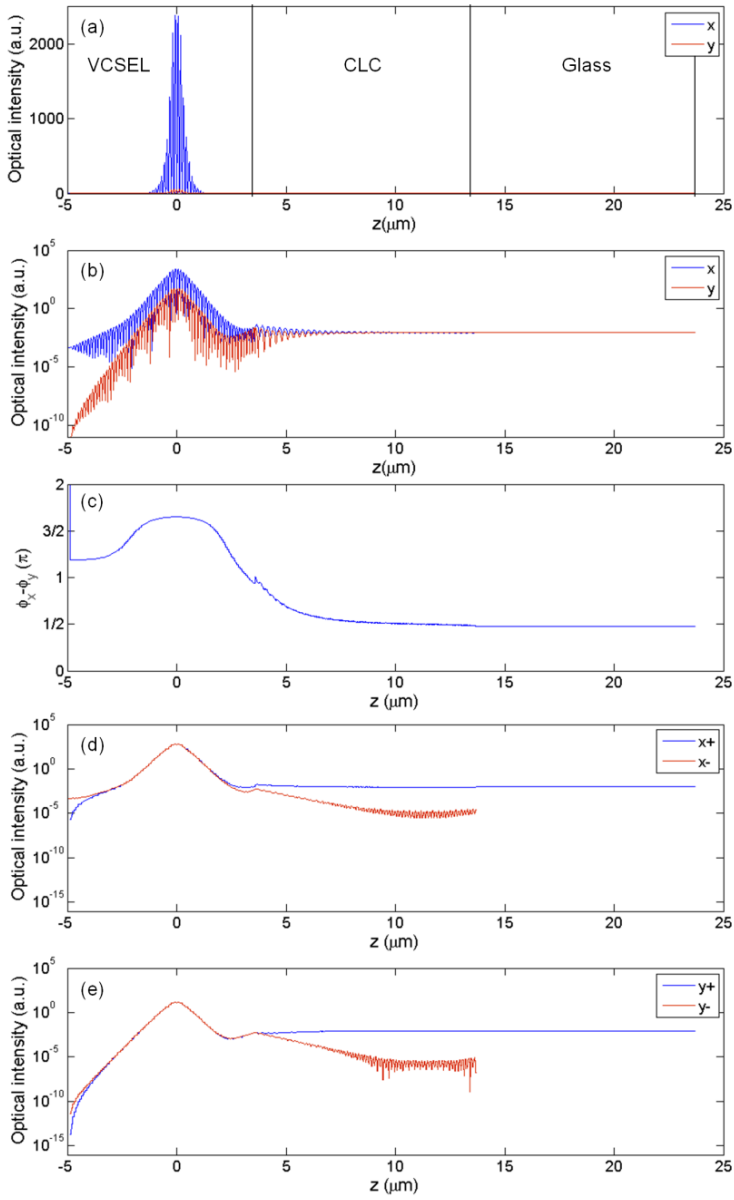

Figure 4.9: (a), (b) Simulations of optical intensity along x and y axis in the CLC-VCSEL device. (c) Phase difference between x and y electrical components moving towards positive z direction. (d), (e) Moving field intensity along x and y axis: +/- towards positive/negative z direction.

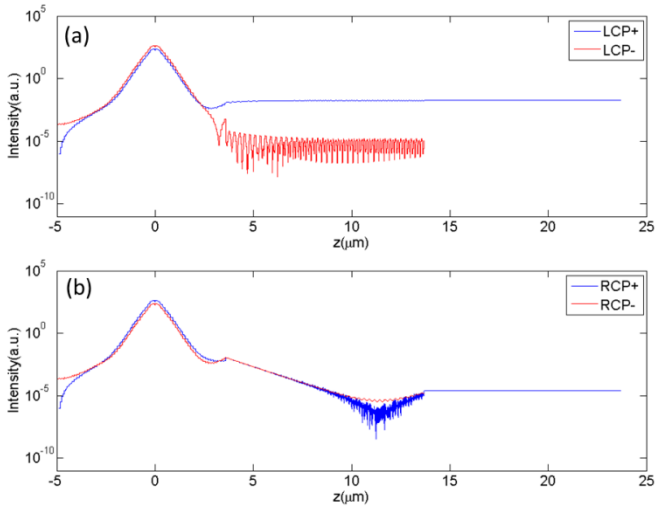

Figure 4.10: Simulations of optical intensity of circular mode propagating fields: +/- towards positive/negative z direction. LCP: left handed circular polarization, RCP: right handed circular polarization.

4.4 Lasing threshold

One of the advantages of a VCSEL from the application point of view is that its threshold current for lasing is rather low. The high emission efficiency and low energy consumption make it a good candidate for many applications, such as light sources and sensors. It will be shown in this section that the threshold can be further decreased, and meanwhile the light emission efficiency can be further increased, by using a CLC overlay. Two different types of host LCs will be demonstrated: 5CB and E7.

4.4.1 Measurements

4.4.1.1 5CB host CLC

The output power is measured for the stand-alone VCSEL (before CLC is filled in the cell) and the CLC-VCSEL as a function of VCSEL driving current. The results are shown in Figure 4.11. The threshold current is calculated by searching the intersection point with the x-axis using a least square linear regression for the linear part of the P-I curve. This method is schematically shown in Figure 4.12.

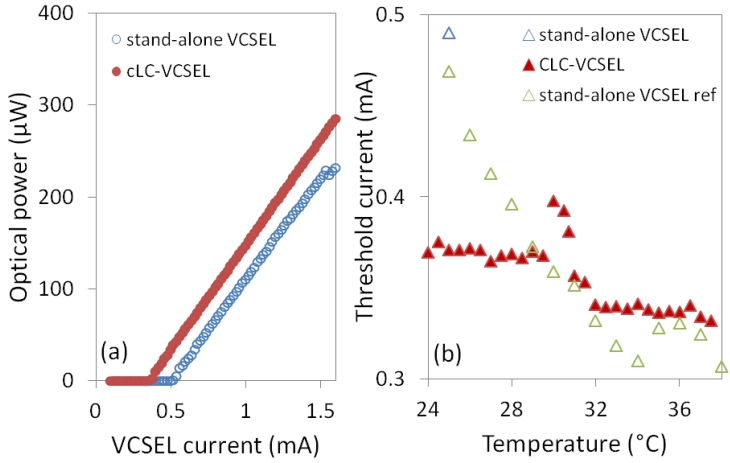

Figure 4.11: (a) Optical power of a stand-alone VCSEL and a 5CB based CLC-VCSEL as a function of VCSEL current at 25 ℃. (b) The threshold current of the stand-alone VCSEL (with another one as a reference) and the CLC-VCSEL at different temperatures.

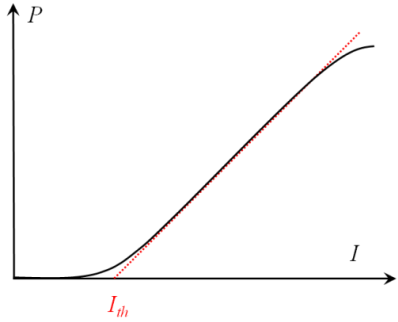

Figure 4.12: Algorithm to calculate the threshold current (I_{th}). The black solid line presents a typical measured power versus current curve. The red dot line is the least square linear regression line for the linear part of the measured curve.

At room temperature (25 ℃, shown in Figure 4.11(a)) the calculated threshold current is 0.49 mA and 0.37 mA for stand-alone VCSEL and for the CLC-VCSEL, respectively. So the threshold current of the CLC-VCSEL is lowered by about 25% compared with the stand-alone VCSEL. At temperatures higher than 30 ℃, the CLC does not play a role and the threshold current of the CLC-VCSEL follows the trend of the threshold current of a stand-alone VCSEL. But the dependence of threshold current on temperature for the CLC-VCSEL does not follow the one of the stand alone

VCSEL for lower temperatures. This difference is confirmed by comparison with a bare VCSEL sample of the same product series (shown as a reference in Figure 4.11(b)). The evolution of the threshold current with temperature is attributed to the gain offset [89-91], which is the difference between the gain peak wavelength and the resonance cavity wavelength. This gain offset changes with temperature because the resonance wavelength red-shifts with temperature. When the gain offset is optimal, the threshold current reaches its minimum. Apparently in our samples, the wavelength spacing between the cavity resonance and the gain peak decreases with temperature and reaches its minimum when the temperature is higher than 32 ℃.

4.4.1.2 E7 host CLC

In this section, measurements are presented for a cell with CLC based on E7. Because the phase transition temperature of E7 is 60.5 ℃, which is higher than the maximum obtainable temperature in our setup, no transition is observed in the measurements. The polarization of the CLC-VCSEL remains left-handed circular in the whole measurement range from 20 ℃ to 50 ℃. The optical power measurements for stand-alone VCSEL and CLC-VCSEL at 25 ℃ are shown in Figure 4.13. Using the same calculation method for CLC in 5CB, the threshold current is 0.40 mA and 0.32 mA for stand-alone VCSEL and CLC-VCSEL, respectively. So, the threshold of CLC-VCSEL is about 20% lower than that of stand-alone VCSEL.

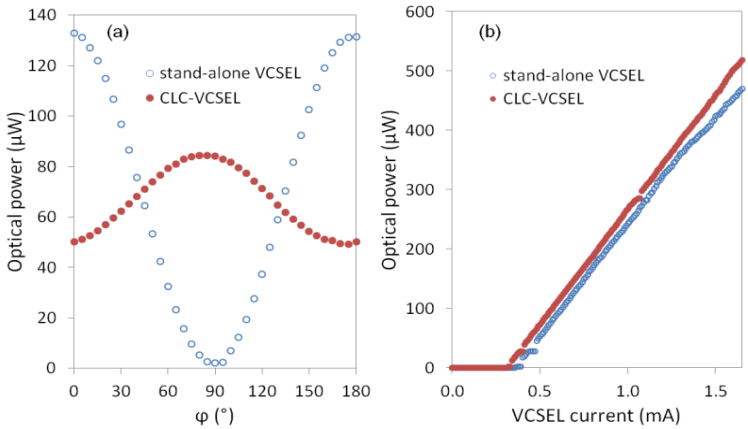

Figure 4.13: (a) Optical power of a stand-alone VCSEL and an E7 based CLC-VCSEL as a function of azimuth of a linear polarizer P at 25 ℃. VCSEL driving current is 1.6 mA. (b) Optical power of a stand-alone VCSEL and an E7 based CLC-VCSEL as a function of VCSEL driving current at 25 ℃.

4.4.2 Simulations

To understand the decreased threshold current of the CLC-VCSEL compared to the bare VCSEL, simulation of the threshold gain is performed for different thickness of the CLC layer. The result is shown in Figure 4.14. It is observed that the threshold gain decreases with increasing thickness of CLC. This is due to the increased reflectivity of the top mirror, which includes the top DBR reflector in the VCSEL and the CLC layer. The thicker the CLC layer, the higher the fraction of the RCP component that is reflected. Therefore, the lasing condition is fulfilled at a lower threshold gain.

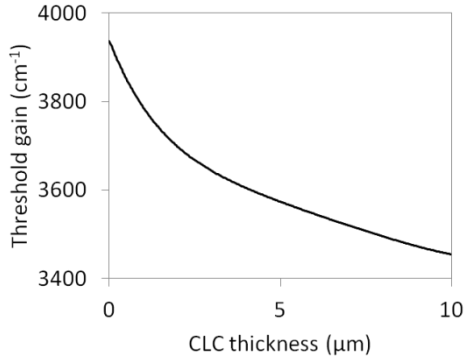

Figure 4.14: Simulation of the threshold gain of CLC-VCSEL as a function of the thickness of CLC layer. The thickness changes from 0 (stand-alone VCSEL) to 10 μm.

4.5 Lasing wavelength

As introduced in the first chapter, one interesting extra functionality would be to have a tunable emission wavelength of the VCSEL. Intrinsically, the VCSEL emits a single wavelength at a certain driving current and a certain temperature. The wavelength can change if the current or temperature changes. This phenomenon is attributed to the temperature dependent refractive index of the semiconductor materials in the VCSEL. In this section, the wavelength properties of the CLC-VCSEL are determined and compared to the stand-alone VCSEL. Interestingly we observe that the wavelength tunability of the CLC-VCSEL is higher than that of the stand-alone VCSEL. Two different types of host LCs - 5CB and E7 - are described.

4.5.1 Measurements

Measurements of the emission wavelength from the stand-alone VCSEL are taken under a series of driving currents and temperatures, in order to know the intrinsic characteristics of the stand-alone VCSEL. From results shown in Figure 4.15(a) and Figure 4.16(a), the intrinsic slope of wavelength versus current or temperature can be determined. The slope for the driving current is about +0.5 nm/mA, while the slope for the temperature is about +0.04 nm/K. Measurements of more than 10 VCSEL chips show that these parameters slightly vary among different VCSEL samples, but the deviation is less than 10%.

4.5.1.1 5CB host CLC

The emission spectra are measured for the stand-alone VCSEL and the CLC-VCSEL at different temperatures and the emission wavelengths are shown in Figure 4.15. It is observed that the wavelength red-shifts as temperature or driving current are increased. This is mainly due to a positive temperature coefficient of the materials of which the VCSEL is made (dn/dT is about $+2\times10^{-4}$/K for GaAs and AlGaAs). For the CLC-VCSEL, the slope of the curve changes at the phase transition from CLC nematic phase to isotropic phase. The slope of the wavelength versus temperature curve at a certain current is about +0.04 nm/K for the stand-alone VCSEL and +0.08 nm/K for the CLC-VCSEL (indicated by solid and dotted black lines in Figure 4.15). It reveals that the temperature based wavelength tuning of CLC-VCSEL is larger than for the stand-alone VCSEL.

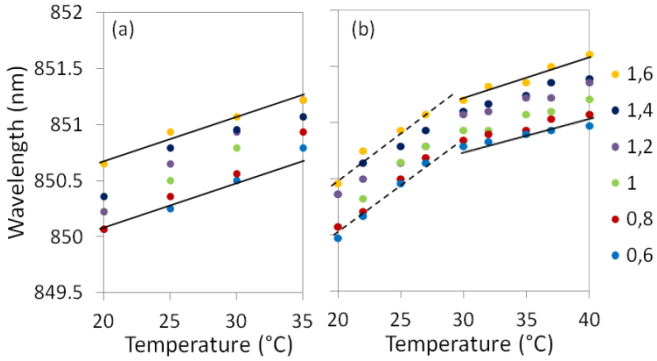

Figure 4.15: Emission wavelength of a stand-alone VCSEL (a) and a 5CB based CLC-VCSEL (b) at different temperatures and different driving currents (shown in the legend in mA unit). The linear dependence of wavelength of a stand-alone VCSEL and a 5CB based CLC-VCSEL on temperature is indicated by solid and dotted black lines, respectively.

4.5.1.2 E7 host CLC

The emission spectra are measured for the stand-alone VCSEL and the CLC-VCSEL at different temperatures and the emission wavelengths are shown in Figure 4.16. Similar to the CLC based on 5CB, the wavelength red-shifts as temperature or driving current increase. The slope of the wavelength versus temperature at a certain current is about +0.04 nm/K for the stand-alone VCSEL and +0.07 nm/K for the CLC-VCSEL (indicated by solid and dotted black lines in Figure 4.16).

So, it is concluded that the wavelength tuning slope is higher for the CLC-VCSEL than the bare VCSEL.

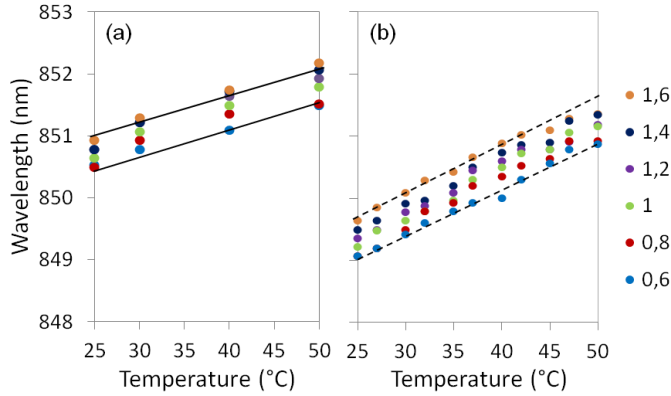

Figure 4.16: Emission wavelength for a stand-alone VCSEL (a) and an E7 based CLC-VCSEL (b) at different temperatures and different driving current (shown in the legend in mA unit). The linear dependence of wavelength of a stand-alone VCSEL and an E7 based CLC-VCSEL on temperature is indicated by solid and dotted black lines, respectively.

4.5.2 Simulations

In order to explain the broader temperature-tuning range of the wavelength for CLC-VCSEL shown in Figure 4.15(b) and Figure 4.16(b), simulations are performed and discussed.

The increased emission wavelength versus temperature slope of the CLC-VCSEL is an effect which cannot be found by incorporating the refractive index changes with temperature of the different materials used. For the

semiconductor materials in the stand-alone VCSEL, a temperature coefficient for the refractive index of 2×10^{-4}/K is considered in the simulations. For the liquid crystal, the variation in refractive index with temperature is taken from [86] and presented in Figure 4.17. However, the increased wavelength versus temperature slope of the CLC-VCSEL can be found in simulations when the pitch of the CLC helix of the CLC helix is increased with increasing temperature. The physical mechanism behind this effect is the fact that the total CLC layer thickness increases. More evidence that this thickness increases with temperature will be demonstrated in the next chapter and its origin will also be explained there. This distance change is in the order of 10 nm per ℃ but varies between samples.

Incorporating a CLC layer thickness change in the simulations (while keeping the number of pitches the same) results in the simulation and measurement results presented in Figure 4.18. Figure 4.18 shows that the emission wavelength periodically increases as a function of the pitch for different thicknesses of the CLC layer. This period can be ascribed to the reflection of the LCP light at the interface between the CLC and the glass substrate. The period of 14nm (for 10μm thick CLC) or 7nm (for 20 μm thick CLC) of pitch corresponds with a phase difference of 2π between the incident and the reflected LCP. The pitch is inversely proportional to the CLC thickness, which indicates that the small reflection at the CLC/ITO/glass interface plays an important role. With a CLC layer thickness variation of 10nm per ℃ the wavelength change with temperature can be explained. Figure 4.19 shows the emission wavelength variation as a function of temperature for two different cases. The blue curve shows the variation of the emission wavelength for a bare VCSEL taking into account the 2×10^{-4}/K refractive index variation. The red curve shows the emission wavelength for a VCSEL with a CLC layer. The temperature variation is clearly stronger in the latter case. Because the pitch in the measurement temperature range remains below one period, the wavelength tuning is monotonic. The simulation for the 5CB host CLC is not presented here but is very similar to the E7 host CLC.

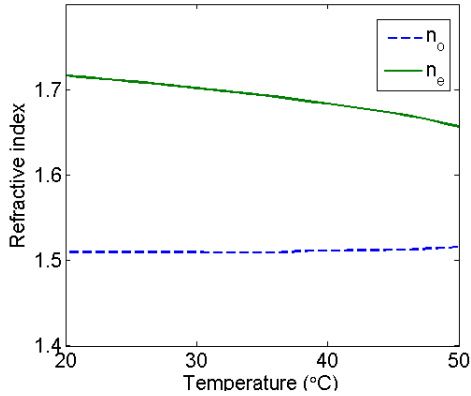

Figure 4.17: Refractive indices of E7 as a function of temperature for wavelength 850 nm.

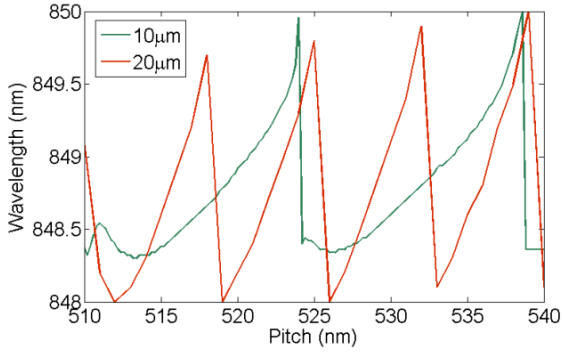

Figure 4.18: Simulation of emission wavelength of E7 host CLC-VCSEL as a function of the pitch for two different thicknesses of the CLC layer.

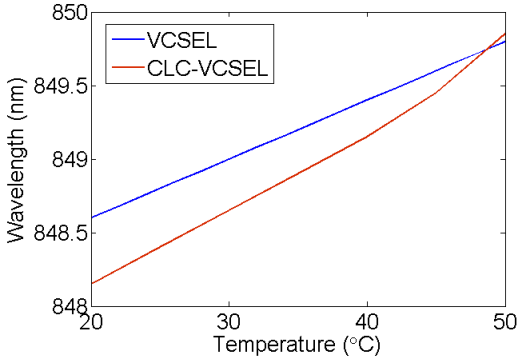

Figure 4.19: Simulation of emission wavelength of stand-alone VCSEL and E7 host CLC-VCSEL as a function of temperature.

Chapter 5

Thermally tunable external cavity

In chapter 4, CLC has been used to provide optical feedback to the VCSEL. This feedback is selective, in other words, only for one circular polarization mode. In this chapter, an external air-cavity is introduced by an additional reflector, metallic or dielectric, which can provide optical feedback irrespective the polarization state. The emission properties, including polarization state, transverse mode profile and wavelength, can be tuned by changing the external cavity length.

5.1 Device structure

The extra reflector of the VCSEL is prepared by using either an aluminum thin film or dielectric reflector. The side view schemes of the devices are shown in Figure 5.1. There are two cell structures: a VCSEL with aluminum reflector (AL-VCSEL) and a VCSEL with dielectric reflector (DE-VCSEL). For the AL-VCSEL (Figure 5.1(a)), the top and bottom glass substrates are covered with respectively a thin semitransparent aluminum film and a transparent conductor indium tin oxide (ITO). The aluminum film is made by thermal evaporation. The cathode and anode of the VCSEL are electrically connected to the bottom ITO and the top aluminum electrodes, respectively through conductive micro-sized gold-coated silica spacers embedded in UV cured optical glue. The transmission of the top glass plate is shown to the right in Figure 5.1(a). For the DE-VCSEL (Figure 5.1(b)),

the top substrate is covered with a patterned chromium (Cr) film and a highly reflective periodic dielectric stack (SiO_2/Ta_2O_5 double layers). The Cr is used as anode electrode of the VCSEL, while the dielectric stack with appropriate layer thicknesses acts as reflector for the VCSEL emission.

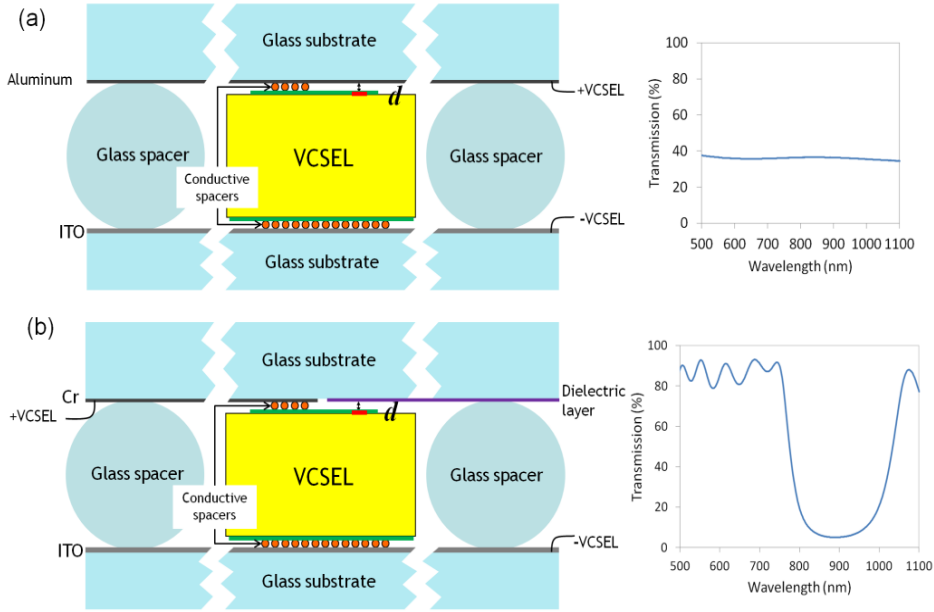

Figure 5.1: Schematic structure of the VCSEL cell. (a) With aluminum reflector: AL-VCSEL. (b) With dielectric reflector: DE-VCSEL. The transmission spectra of the corresponding reflectors are shown to the right. *d*: the length of the external cavity. The laser is emitted from the emitter of the VCSEL chip which is indicated by a red line on the top right of the VCSEL.

The periodic dielectric material has an optical reflection band which is similar to a Bragg reflector. The position of this reflection band is determined by the optical refractive indices and the thicknesses of the materials. In order to make an effective reflection of the VCSEL emission, the band should be designed to include the emission wavelength. Therefore, calculations are performed to estimate the thickness of each layer in the periodic structure. The predicted transmission of suitable optical refractive index and thickness of the material in each layer are demonstrated in Figure 5.2. It is found that for more than 6 pairs of layers, the transmission at 850 nm is sufficiently low. Considering the difficulty of accurate thickness

control during the fabrication process, 6 pairs are chosen as the optimal number in the experiments. On top of an ITO coated glass substrate, six pairs of SiO_2/Ta_2O_5 are evaporated layer by layer, using e-gun evaporation. The transmission through the top glass plate is measured and shown to the right in Figure 5.1(b). It agrees with the simulation and indeed provides good reflection at 850 nm.

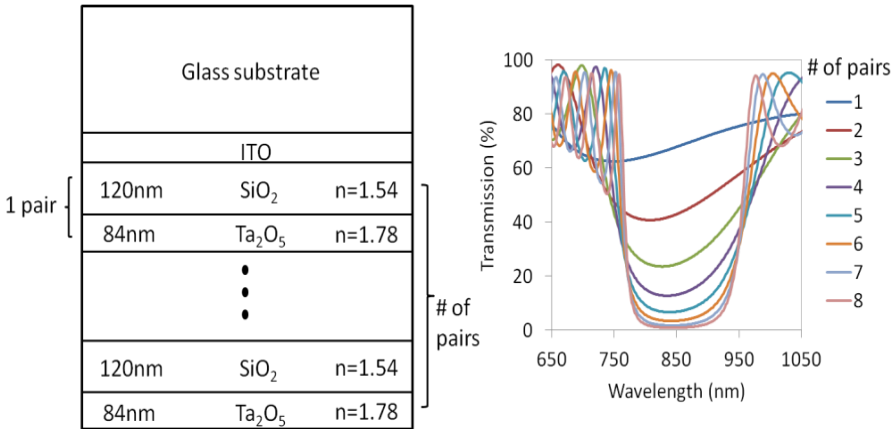

Figure 5.2: (*left*) Schematic structure of the top substrate of a DE-VCSEL. (*right*) Simulations of the transmission through the top substrate for different numbers of pairs of layers.

The diameter of the conductive spacers is 10 μm ± 0.1 μm. The length of the cavity between the VCSEL emitter and the top substrate is determined by the diameter of these spacers, but also by temperature, because thermal stresses in the materials lead to a deformation of the device as will be demonstrated by the measurements in this chapter. The optical microscope pictures of the square VCSEL wafer inside the devices are shown in Figure 5.3. The pictures are taken in reflection mode.

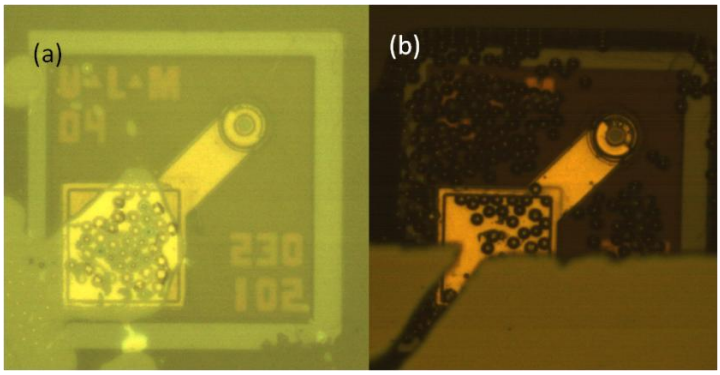

Figure 5.3: Reflection microscopic pictures of the VCSEL in the device: (a) AL-VCSEL (the AL film is semi-transparent for visible light), (b) DE-VCSEL (the dielectric reflector is transparent for visible light; the opaque part is the Cr film).

5.2 Optical setup

The optical setup shown in Figure 5.4 is designed to characterize different optical properties of the VCSEL cell emission: polarization state, emission wavelength and transverse mode profile. Compared to the previous setup described in Figure 3.5, the current setup allows to measure all parameters at the same time. The light beam propagates along the *z* direction. The quarter wave plate (with azimuth of the fast axis α) and the linear polarizer with azimuth φ are parallel to the *x*-*y* plane with reference 0 °parallel to the *x* axis. The 0 ° reference is chosen to be parallel with the dominant polarization direction (P_x) of the VCSEL emission. The orthogonal polarization mode P_y corresponds to φ=90 °. Convex lenses are used to transform the emission of the VCSEL into a parallel beam and to focus the transmitted beam onto a spectrometer or a photo-detector, which is connected to a calibrated power meter. Far field pictures are taken on a screen by a camera. The temperature of the VCSEL cell is controlled by a temperature controller.

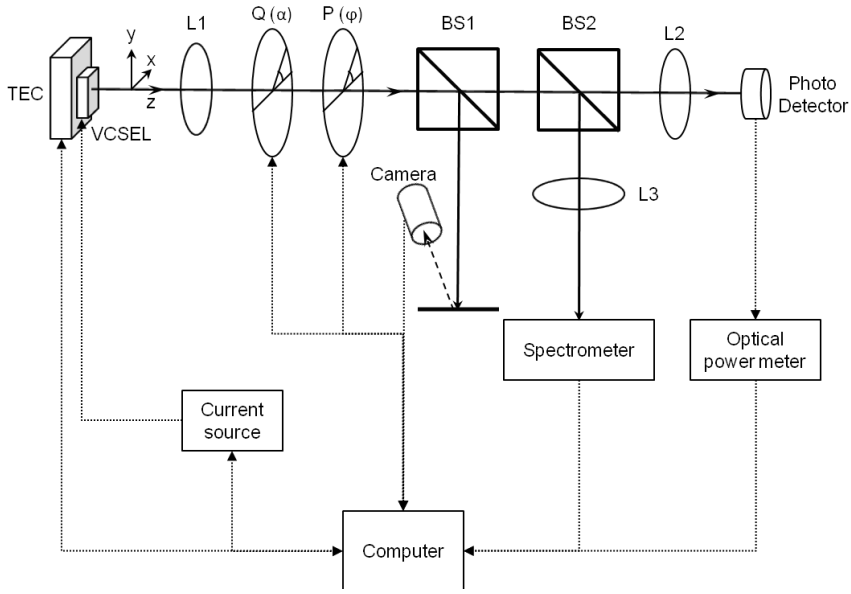

Figure 5.4: Optical setup for the VCSEL emission measurement. L1, L2, L3: convex lenses. Q: quarter wave plate with azimuth α. P: linear polarizer with azimuth φ. TEC: temperature controller. BS: beam splitter. The light propagates mainly along the z direction.

5.3 Polarization

As a reference, the measurements for the bare VCSEL cell indicate that the emission polarization remains at its original polarization mode, irrespective of temperature. The improved cell design in this chapter will show the advantage of controlled polarization switching. All measurement results in this chapter are obtained by driving the VCSEL with a fixed current of 1.6 mA.

5.3.1 Competition between two intrinsic orthogonal modes

5.3.1.1 AL-VCSEL

The output optical power is measured as a function of temperature for the two orthogonal polarizations P_x and P_y. The results are shown in Figure 5.5. We found that in the whole operating temperature range, a periodic polarization switching occurs. It is shown in Figure 5.5 that in temperature ranges from 27 ℃ to 30 ℃, from 36 ℃ to 38 ℃ and from 43 ℃ to 44 ℃, the dominant polarization state is P_y. In temperature ranges from 30 ℃ to

35 °C, from 38 °C to 43 °C and from 44 °C to 48 °C, P_x is the dominant mode. The period of the polarization switching is about 7 °C. It is noted that at temperatures about 26 °C and 36 °C, the two orthogonal polarizations co-exist. This means that the polarization switch from P_x to P_y is not as steep as the switch from P_y to P_x (as shown in Figure 5.5).

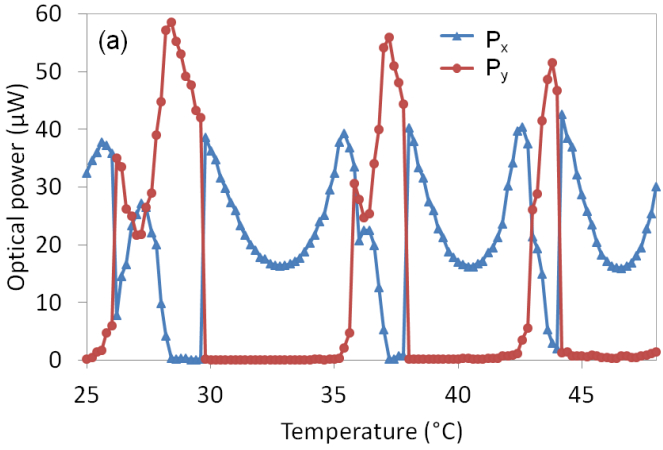

Figure 5.5: Measurement of the optical power of AL-VCSEL for two orthogonal polarization modes at different temperatures.

5.3.1.2 DE-VCSEL

The measurement of the optical power of the DE-VCSEL for two orthogonal polarization modes P_x and P_y at different temperatures are shown in Figure 5.6. Similar to the AL-VCSEL the polarization switches between P_x and P_y when temperature is increasing. P_x is dominant in temperature ranges from 20 °C to 25 °C and from 30 °C to 35 °C. While P_y is dominant in temperature ranges from 25 °C to 30 °C and from 35 °C to 40 °C. This switching happens for a period of about 10 °C. However, it is different with the AL-VCSEL that all the switches are very steep, and there is less co-existence between modes in Figure 5.5.

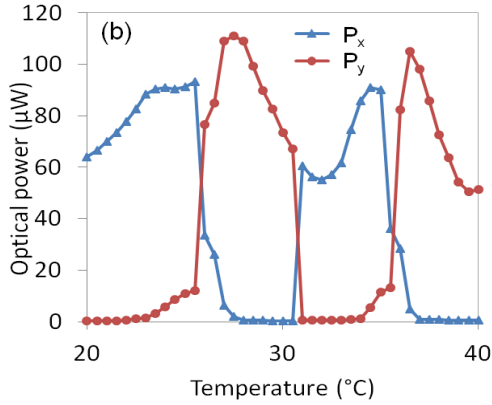

Figure 5.6: Measurement of the optical power of a DE-VCSEL for two orthogonal polarization modes at different temperatures.

The threshold current of the DE-VCSEL is measured as a function of temperature and is shown in Figure 5.7. It is found that also the threshold current exhibits periodic fluctuations, which correspond to the optical power measurements in Figure 5.6. It is noted that the polarization switching (at 27 °C and 37 °C) happens near the local maximum of the threshold current. This is because the mode at which the VCSEL is lasing is the one which has the lowest threshold gain. When the threshold gain of mode P_x increases with temperature and overtakes the threshold gain of mode P_y, the lasing mode changes from P_x to P_y.

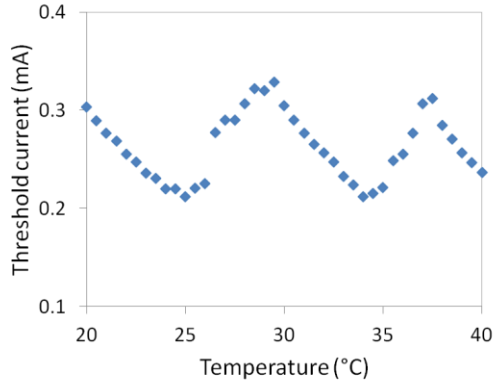

Figure 5.7: Measurement of the threshold current of DE-VCSEL at different temperatures.

5.3.2 Simulation of the external cavity length dependent threshold

To understand the reason for this switching behavior and to demonstrate that the observed results can be explained by a change in external cavity length, simulations of the threshold gain (G_{th}) of the AL-VCSEL lasing system are carried out using the plane wave expansion method which has been explained in chapter 2. The parameters used in the simulation are listed in Table 5.1. The simulation for the DE-VCSEL is similar. The simulation results for two polarization modes are shown in Figure 5.8 and Figure 5.9, respectively. The minimum threshold gain for both polarization modes as a function of the cavity length is presented in Figure 5.10. We assume that the length of the external cavity changes with temperature because of the thermal expansion effect of the device. The influence of temperature on the refractive index of the materials is ignored in the simulations as this only leads to the steady background increase of the emission wavelength. At room temperature, the length of the external cavity is assumed to be 10 µm and it is increased to about 11 µm. This length range is used in the simulation to match with the measurement results. Because the real VCSEL exhibits an emission which is diverging with angles up to about 10°, the simulation is carried out for angles from 0° to 10°. A small residual-stress birefringence of 10^{-4} in the refractive index (real part) of the VCSEL semiconductor materials between x and y direction is included in the simulations to favor the emission of one of the two linear polarization directions [43, 83, 92]. From the simulation results, we find that the threshold gain G_{th} changes periodically with the external cavity length. The period is determined from the simulation results as 0.425 µm, which obviously corresponds to half of the VCSEL emission wavelength (0.85 µm). The switching of the polarization can be explained by the minimal threshold gain selection at a certain temperature.

Table 5.1: Parameters of VCSEL with external reflector used in simulation.

Cell structure	Material	Refractive index	Thickness
Bottom/top DBR: 37.5/27 pairs	$Al_{0.12}Ga_{0.88}As$	$3.52 - i10^{-4}$	60.3 nm
	$Al_{0.9}Ga_{0.1}As$	$3.11 - i10^{-4}$	68.3 nm
VCSEL cavity	$Al_{0.3}Ga_{0.7}As$	$3.4 - i10^{-4}$	113 nm
	GaAs (QWs)	$3.62 + i$ Im{n}	24 nm
	$Al_{0.3}Ga_{0.7}As$	$3.4 - i10^{-4}$	113 nm
External cavity	air	1	10 µm
Metal reflector	Al	$2.59 - i8.17$	20 nm

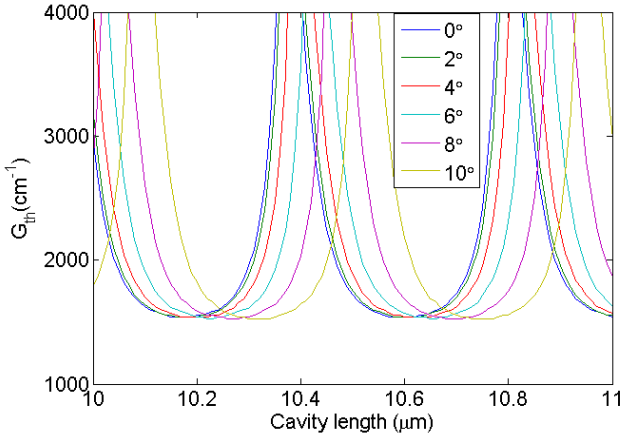

Figure 5.8: Simulation of the AL-VCSEL threshold gain (G_{th}) of the P_x mode as a function of extra cavity length for different emission angles.

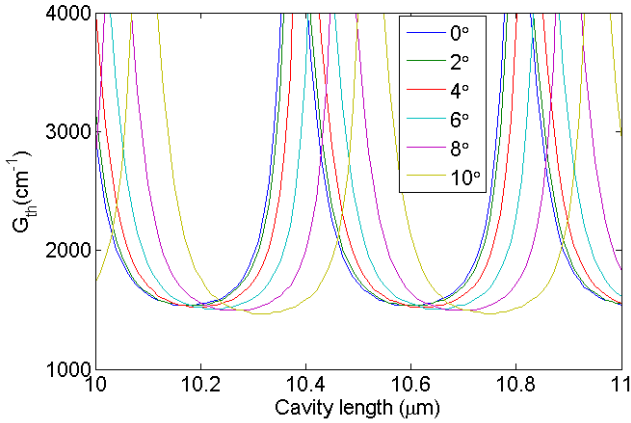

Figure 5.9: Simulation of the AL-VCSEL threshold gain (G_{th}) of the P_y mode as a function of extra cavity length for different emission angles.

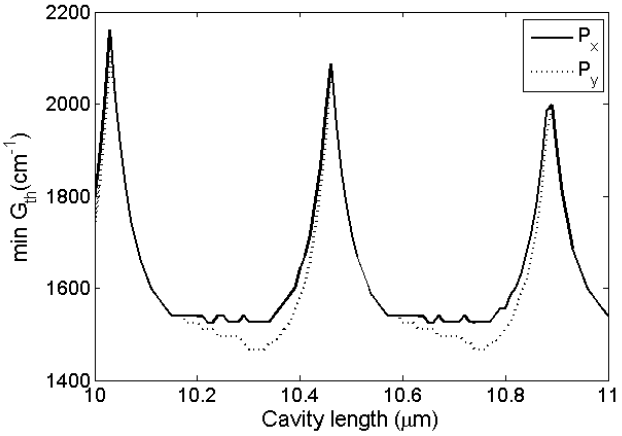

Figure 5.10: Minimum threshold gain for both polarization modes of the AL-VCSEL as a function of the cavity length.

By comparing the simulations with the measurements, the relationship between the external cavity length and temperature can be determined. Analysis of the simulations results points towards an increasing external cavity length with temperature. The quantified dependence is about 60 nm/K. This means that the external air cavity length increases one half of the VCSEL wavelength (425 nm) if the temperature increases about 7 °C. This temperature dependence is demonstrated in Figure 5.11.

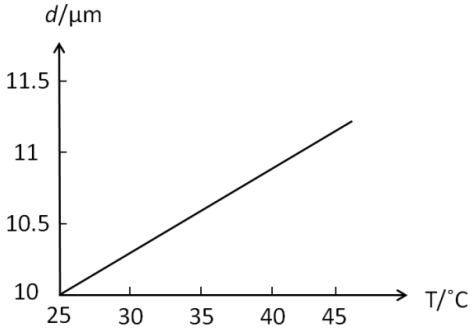

Figure 5.11: The proposed relation between the external cavity length *d* and the device temperature *T*.

The reason for this temperature dependent behavior can be explained as following. The mechanical forces raised by heating this complex device

structure play an important role in tuning the physical length of the external cavity, *d* in Figure 5.1. All temperature related phenomena in this chapter can be attributed to the relationship between the external cavity length and the device temperature.

The VCSEL is glued between two glass plates with spacers in between and stresses are introduced during the production process. These stresses change by temperature, as different materials have different expansion coefficients. So we expect a force exerted by the top glass plate via de conductive spacers on the anode of the VCSEL. As a result, the VCSEL chip can slightly tilt around the conductive spacers on the anode pad and the distance between the VCSEL emitting region and the top substrate changes as a function of the device temperature. For temperatures not far away from room temperature, this relation can be approximately treated as a linear increase of the distance with increasing temperature.

5.4 Transverse mode profiles

In this section, the transverse modes of the emission are investigated at different temperatures. The external cavity length is controlled by the temperature and modulates the optical feedback for the VCSEL. Both far-field beam pictures and light intensity profiles are measured for two orthogonal polarization modes. Intrinsically, the beam profile of a VCSEL without external reflector remains in the fundamental mode and the polarization remains P_x, independent of the temperature.

5.4.1 Periodic change of beam profiles

Far field pictures of the two linear polarization modes at different temperatures are shown in Figure 5.12. These measurements are carried out without quarter wave plate. For polarization mode P_x, the pictures are taken when the linear polarizer is parallel to the *x* axis (φ =0°). For polarization mode P_y, the polarizer is set at φ=90°. The beam profile varies with temperature and is usually circular symmetric, except for certain temperatures: 30 °C, 37 °C and 43 °C. There is an approximate periodic variation of the beam profile between fundamental mode and high-order modes with temperature. The transverse intensity profiles along the horizontal axis of the beam pictures at temperatures from 29 °C to 34 °C (one period) are analyzed and shown in Figure 5.13.

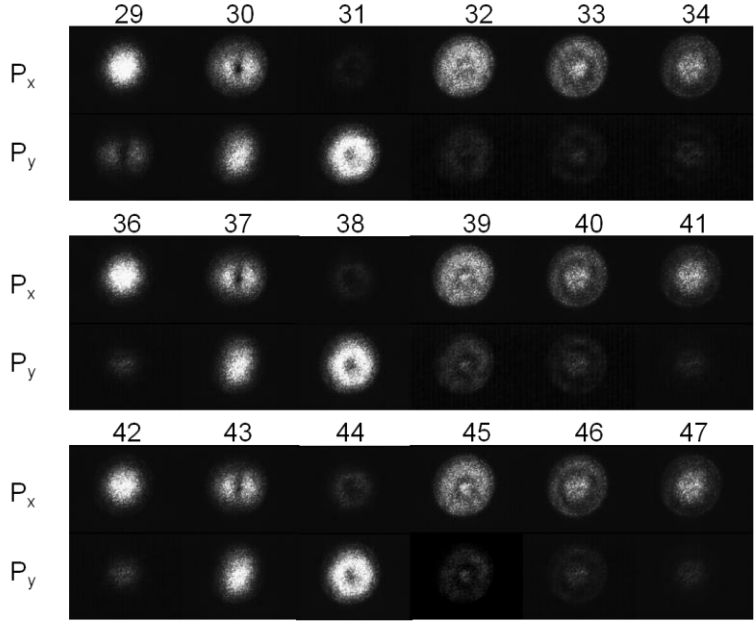

Figure 5.12: Far field beam profiles of AL-VCSEL for two orthogonal polarizations at different temperatures.

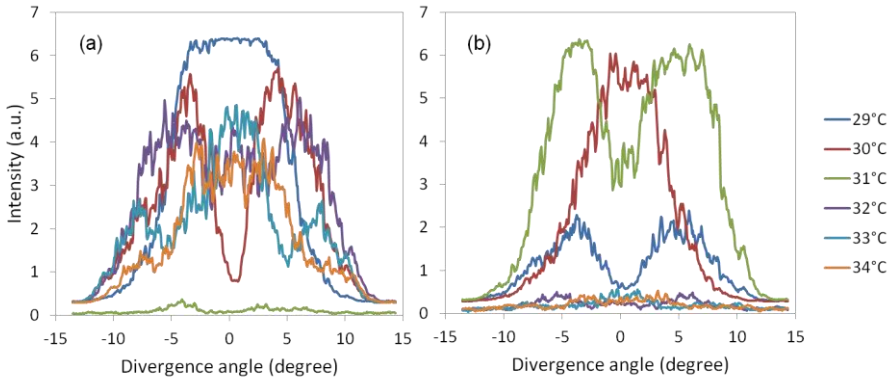

Figure 5.13: Intensity profiles of the beam pictures of AL-VCSEL for two orthogonal orientations of the polarizer P at temperatures from 29 ℃ to 34 ℃. (a) P_x mode; (b) P_y mode.

These results correspond to the polarization measurements of their intensity in section 5.3. The position of the cell on the temperature controller and the

change in ambient temperature may have caused the small mismatch between the polarization and beam profile measurements.

5.4.2 Simulation of the angle dependent threshold

The simulation results of the threshold gain of AL-VCSEL are shown in Figure 5.14. They are based on the same simulation data as Figure 5.8 and 5.9. The divergence angle of the lasing is used as variables here. It is observed that the angle dependent G_{th} changes periodically with the external cavity length. This period is 0.425 μm, which is the same with the simulation in section 5.3. In one period shown in Figure 5.14, the emission angle is determined by the minimal threshold gain. When the external cavity length is about 10.1 μm, lasing happens at small angles. If the external cavity length is about 10.35 μm, lasing would take place at large angles. In between these two cases, the emission direction gradually transits along with the external cavity length and could be at both small and large angles. This simulation can explain the periodic beam profiles shown in Figure 5.12 and 5.13. With increasing temperature, the external cavity length increases, so that the beam profiles changes. The measured beam profiles show similar periodic angle characteristics with the simulation. This result confirms the relationship between the external cavity length and the temperature which is presented in Figure 5.11.

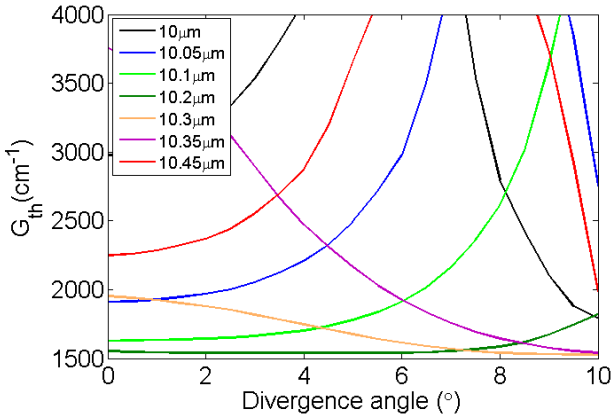

Figure 5.14: Simulation of the AL-VCSEL threshold gain (G_{th}) of P_x mode as a function of emission angle for different external cavity lengths.

5.5 Emitting wavelength

The thermal drift of the emission wavelength has already been demonstrated in chapter 4. There it has been shown that the emitting wavelength red-shifts with increasing temperature with a slope of about 0.04 nm/K. In this chapter the wavelength does not show a continuous behavior, as in the previous chapter, but switches rather abruptly.

5.5.1 Measurements

The emission spectra of the AL-VCSEL are measured for two linear polarization directions at different temperatures (Figure 5.15). The emission wavelength increases with temperature, which is expected due to the refractive index change of the semiconductor materials in the VCSEL structure. On top of this increasing background, periodic switches of the emission wavelength (about 1 nm) are observed. The switches happen at temperatures 27 °C, 37 °C and 43 °C.

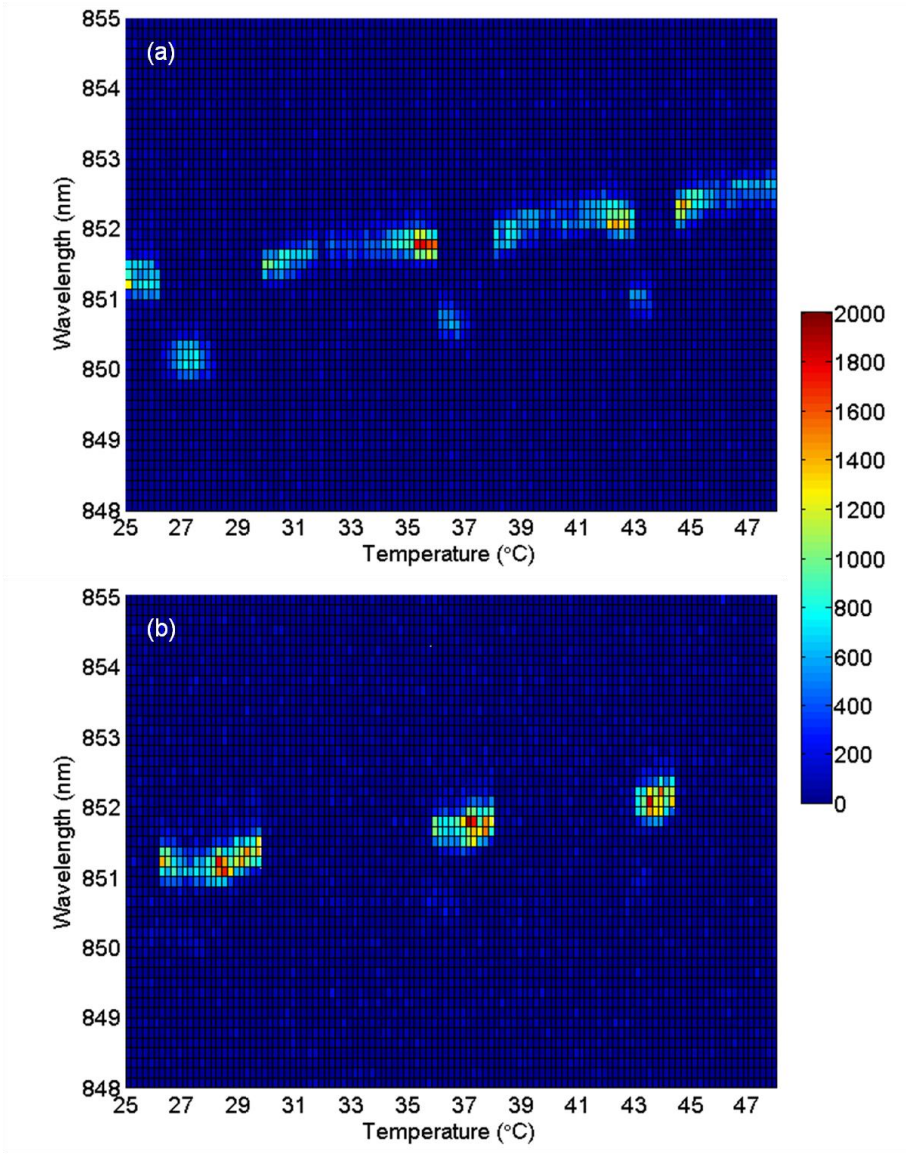

Figure 5.15: Emission spectra of AL-VCSEL for two orthogonal orientations of the polarizer P and for different temperatures. (a): P_x mode; (b): P_y mode.

5.5.2 Simulations

The simulation of the AL-VCSEL laser emission wavelength of P_x polarization as a function of the external cavity length helps to understand the switching of longitudinal modes. The simulation is done for different emission angles. Firstly, the variation of the emission wavelength at 0 degree is simulated together with the threshold gain. This is shown in Figure 5.16. It is observed that at a certain external cavity length (about 10.35 μm or 10.8 μm), the emission wavelength jumps (and reduces by a few nanometer) in correlation with the minimum threshold gain. Switching happens at a period of a half wavelength. This phenomenon can be explained by the phase shift caused by the external cavity.

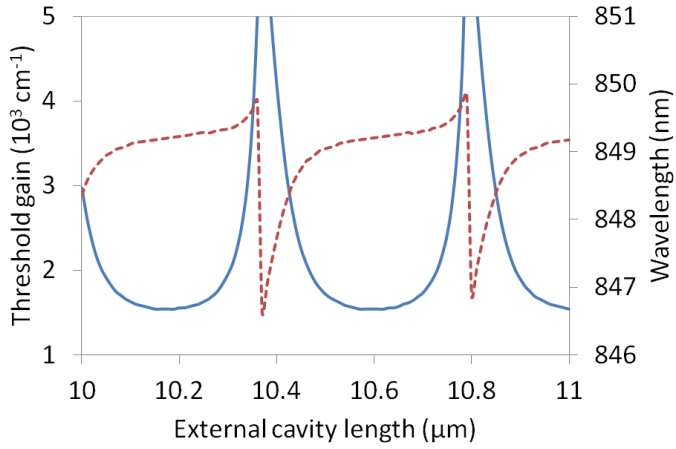

Figure 5.16: Simulation of the AL-VCSEL threshold gain (blue solid line) and lasing wavelength (red dot line) of P_x mode as a function of the external cavity length. The emission angle is 0 degrees.

The simulations for other emission angles are shown in Figure 5.17. Because the lasing angle will shift with the cavity length in order to maintain the minimum threshold gain (as illustrated in Figure 5.10), the emission wavelength will vary as indicated by the black line in Figure 5.17. As we have only simulations for every 2 degrees, the black line appears to switch discontinuously between the curves in Figure 5.17. Actually, the wavelength behavior can be attributed to the transverse mode switching demonstrated in Figure 5.12. The transverse mode switches from fundamental to first order, the resonant wavelength decreases simultaneously. The emission wavelength

of different VCSEL chips of the same batch varies between 850 and 860 nm due to manufacturing variations, and the value of the wavelength in the simulations and experiments also do not match exactly. When the external cavity length changes half of the emission wavelength, one new resonance mode appears. This is confirmed by the optical power measurements shown in Figure 5.5. The total optical power reaches a peak when a new standing wave mode is formed.

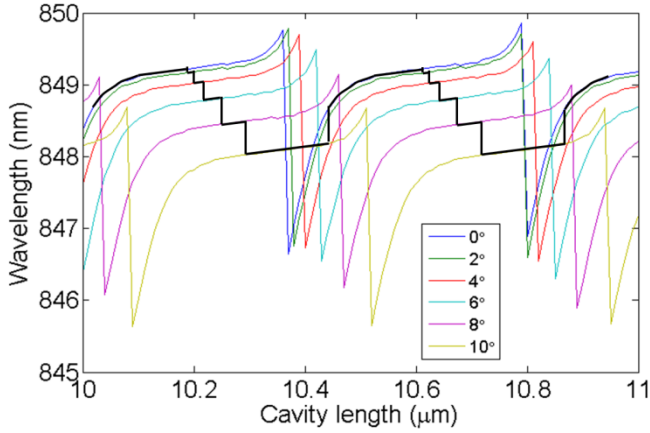

Figure 5.17: Simulation of the AL-VCSEL lasing wavelength of P_x mode as a function of the external cavity length for different emission angles. The black line indicates how the lasing wavelength will change to obtain the minimum threshold gain.

Chapter 6

Electrically tunable external cavity

In this chapter, the VCSEL has an external cavity of which the optical length can be tuned by a voltage. The tunable external cavity for the VCSEL is provided by a dielectric reflector and a thin layer of nematic liquid crystal between the reflector and the VCSEL. From now on this device will be referred to as the DE-LC-VCSEL. The reflection band of the dielectric mirror is designed to match the emission wavelength of the VCSEL by choosing the appropriate layer thicknesses. By changing the voltage across the LC layer, the optical length in the external cavity can be tuned for one linear polarization component. Hence the emitting properties of the DE-LC-VCSEL, including the polarization state, emission wavelength and threshold current, can be controlled by the voltage applied over the LC layer.

6.1 Cell structure

The side view of the device is shown in Figure 6.1. The cathode and anode of the VCSEL are electrically connected to the bottom ITO and the top chromium electrodes, respectively, through micro-sized gold coated silica embedded in UV cured optical glue. The diameter of these balls is 10 μm ± 0.1 μm. The physical length of the cavity between the VCSEL emitter and the top substrate is determined by the diameter of these spacers.

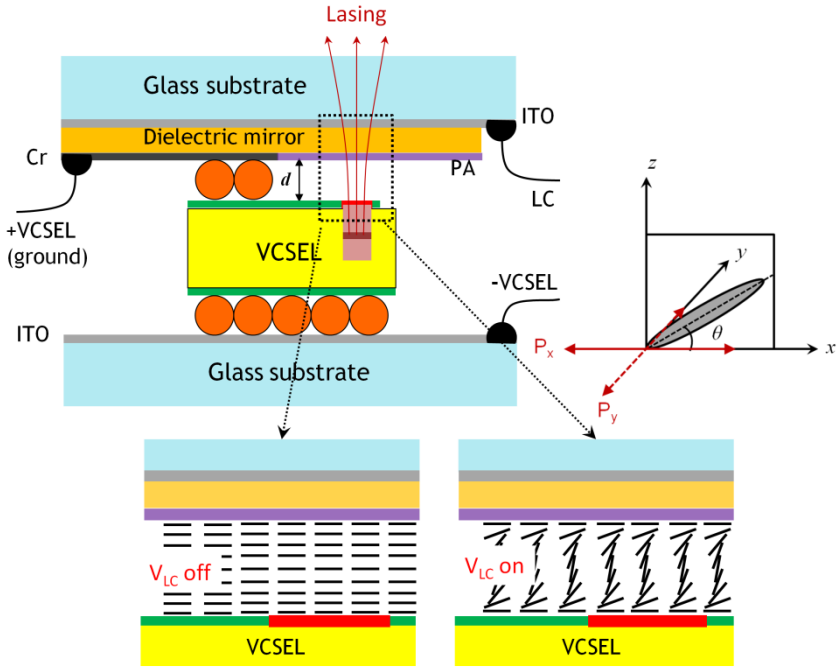

Figure 6.1: Schematic structure of the LC-VCSEL cell. *d*: physical length of the external cavity. The inserted pictures show the LC director configurations for two cases: with or without voltage applied over the LC layer. The *xyz* coordinate system is also shown.

In order to drive the VCSEL and to tune the LC cavity independently, two separated pairs of electrodes are necessary for the VCSEL and the LC layer. For this reason, the cell structure is designed properly so that the two pairs of electrodes work independently. As shown in Figure 6.1, the chromium on the top substrate and the ITO on the bottom substrate are the two electrodes for VCSEL; while the ITO on the top substrate and the chromium (connected to the anode at the top of the VCSEL chip) are electrodes to apply a voltage over the LC. Given the high resistivity of the dielectric layer, the ITO and chromium on the top substrate are effectively insulated.

The external cavity is formed by the reflection from the dielectric reflector coated on the top substrate. As demonstrated in section 5.1, six pairs of SiO_2/Ta_2O_5 thin layers are coated on the substrate in order. The thickness of each layer is controlled accurately by the evaporation rate and time, so that the bi-layer structure has an optimal reflection property.

The alignment of the LC molecules in the external cavity is controlled by the photo-alignment layer, and this planar alignment direction is chosen to be the same as the original linear polarization direction of the VCSEL (defined as x axis).

6.2 Voltage controlled liquid crystal orientation

As introduced in Chapter 1 and presented in Chapter 3, planar aligned nematic LC can reorient according to the applied voltage. Due to its birefringent property, the optical path length changes as a result of this reorientation. In Chapter 3 this phenomenon was used to modify the polarization state of the emitted light. In this Chapter the effect is used to modify the optical path length of one linear polarization mode.

The orientation of the LC under a certain voltage is represented in Figure 6.1. In the coordinate system, the rotation of the LC molecule director occurs within the *x*-*z* plane and has a tilt angle of θ. The orientation of the LC director influences the effective refractive index for the beam with polarization parallel to the LC alignment. The optical path length of this polarization mode (mode P_x) changes with the LC director orientation. The polarization mode P_y always encounters the ordinary refractive index and its optical path length is independent of the voltage. As a result, the reflection and the lasing threshold for P_x change with the applied voltage, while the values for P_y remain constant. When the lasing threshold for P_x increases above that for P_y, the polarization switches from P_x to P_y and the threshold current reaches a local maximum.

6.3 Measurements and simulations

The emission properties of the LC-VCSEL are measured at different voltages applied across the LC layer at room temperature 28 °C. An ac voltage of 1 kHz square wave is applied. Voltages ranging from 0 to 5 V (peak-to-peak voltage) are used in all measurements. The results of polarization, threshold current, slope efficiency, and emission wavelength are shown in this section. These measurements are compared to the theoretical simulation of the threshold gain (G_{th}) and emission wavelength of the lasing system. The parameters used in the simulation are displayed in Table 6.1.

Table 6.1: DE-LC-VCSEL parameters

Structure	Material	Refractive index*	Thickness
Bottom/top DBR: 37.5/27 pairs	$Al_{0.12}Ga_{0.88}As$	$3.52 - i10^{-4}$	60.3 nm
	$Al_{0.9}Ga_{0.1}As$	$3.11 - i10^{-4}$	68.3 nm
VCSEL cavity	$Al_{0.3}Ga_{0.7}As$	$3.4 - i10^{-4}$	113 nm
	GaAs (QWs)	$3.62 + i$ Im{n}	24 nm
	$Al_{0.3}Ga_{0.7}As$	$3.4 - i10^{-4}$	113 nm
External cavity	E7	n_e=1.7, n_o=1.5	10 μm
Dielectric reflector: 6 pairs	SiO_2	1.54	120 nm
	Ta_2O_5	1.78	84 nm

*There is an anisotropy of 10^{-4} between x and y directions in VCSEL materials.

6.3.1 Polarization

The emission properties of the DE-LC-VCSEL are measured for different voltages applied across the LC layer. The optical power is measured as a function of the azimuth angle of the polarizer, as shown in Figure 6.2. This measurement is repeated for different voltages from 0 to 4 V. For different voltages applied over the LC layer, the curves are proportional with either $\cos^2\alpha$ or $\sin^2\alpha$, which indicates that the emission is linearly polarized along either the x or the y direction. To illustrate the polarization switching behavior, the optical powers along the two orthogonal directions x and y (P_x and P_y modes) are measured and shown in Figure 6.3 as a function of the voltage applied over the LC layer. The polarization direction changes from x to y in voltage zones of 1.1~1.2 V, 1.5~1.7 V and 2.1~2.5 V. The contrast ratio between the two polarizations remains high in the whole voltage range. The switching of the polarization is controllable by applying a suitable voltage over the LC layer.

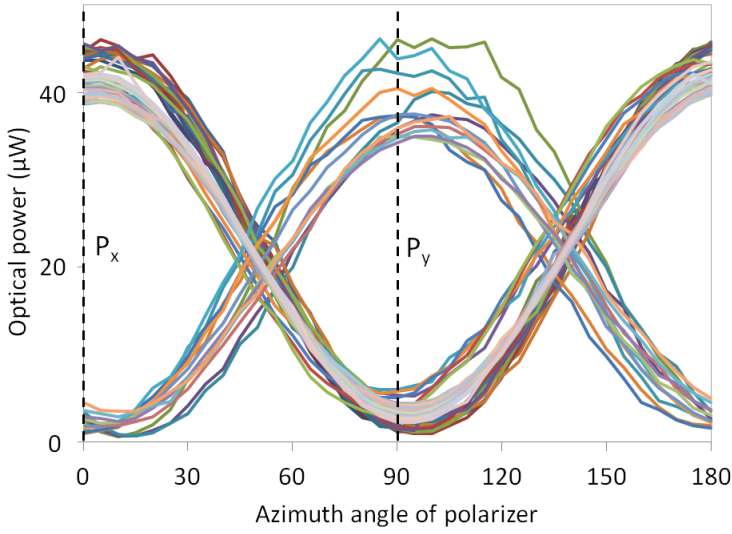

Figure 6.2: Measured optical power as a function of the azimuth angle of polarizer. Each curve corresponds to an applied voltage over the LC layer. The power at 0 (90) degrees represents the contribution of the P_x (P_y) polarization.

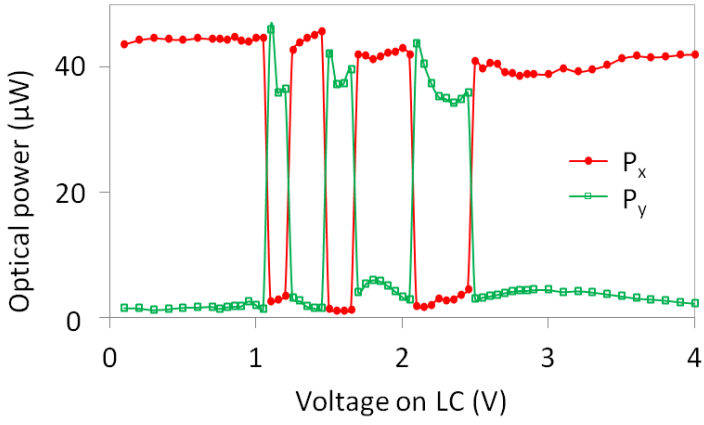

Figure 6.3: Measured optical power for two polarizer azimuth angles (0° and 90°, or along x and y axis, respectively) at different voltages applied on LC layer. VCSEL current is 1mA.

The polarization switching for different transient voltages is shown in Figure 6.4, 6.5 and 6.6. The optical power of the P_y mode is measured during the applications of a time-dependent voltage signal over the LC. It is observed that when the LC switches dynamically from 0 V to 3 V (Fig. 6.4) the polarization switches between P_x and P_y in the same way as for the steady state, shown in Figure 6.3. We record the switching over 100 ms which is the typical switching time for this kind of LC, with the given voltage and layer thickness. Figure 6.4 illustrates that full switching of the LC is not needed because the VCSEL switches polarization several times. The actual polarization switching of the VCSEL occurs in a much shorter time than the LC switching time.

Stable and reproducible switching can be achieved by using two voltage amplitudes - just below and just above a polarization switching point - and sufficiently long time intervals to let the LC reach its steady state (Figure 6.5). The observed power oscillations of about 100 Hz come from the data acquisition device. The switching itself occurs in less than 100 µs (inset figures in Figure 6.5). The time interval between two polarization switching events can be drastically shortened by using an overdrive scheme which is known from display technology. The voltage is shortly set to a value much higher (or lower) than the steady state value, to speed up the reorientation of the LC director. To demonstrate this principle, we switch the amplitude of the applied voltage from 2.1 V to 0 V. There is a lag time of about 4 ms before the laser switches from P_y to P_x. Almost directly after the switching to P_x we apply an amplitude of 2.4 V which results in a lag time of 2 ms before switching back to P_y (Figure 6.6). After this we apply again the steady state value of 2.1 V. The actual switching time of the laser cannot be detected because the acquisition time of our photodiode is limited to 10 µs. In this way we demonstrate that with an overdrive scheme one switching cycle can be completed in only a few milliseconds.

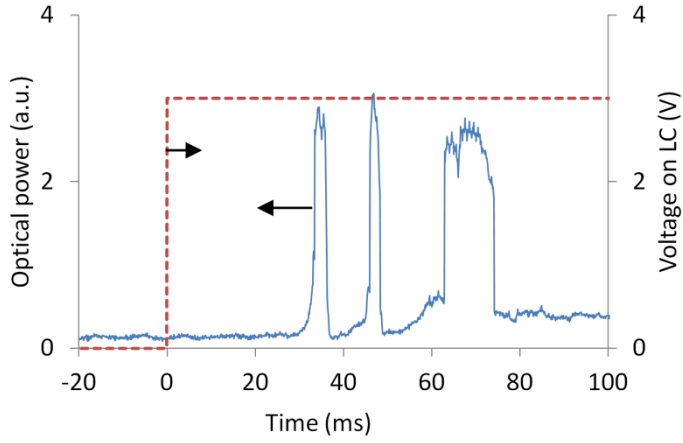

Figure 6.4: Transient optical power of the P_y mode (blue solid line) and amplitude of the applied voltage over the LC (red dashed line, frequency 1kHz), during switching of the liquid crystal. The VCSEL current remains at 1mA.

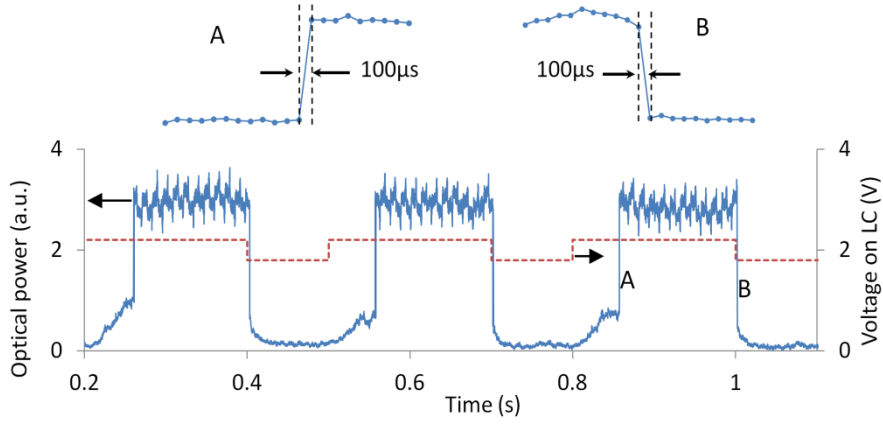

Figure 6.5: Transient optical power of the P_y mode (blue solid line) and amplitude of the applied voltage over the LC (red dashed line, frequency 1kHz) during switching of the liquid crystal. The voltage amplitude switches between two values. The inserted graphs show the detailed measurement data of two switches A and B.

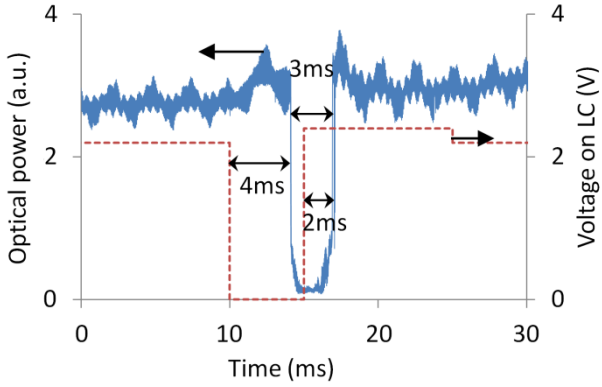

Figure 6.6: Transient optical power of the P_y mode (blue solid line) and amplitude of the applied voltage over the LC (red dashed line, frequency 1kHz) during switching of the liquid crystal. The time intervals between polarization switching and the voltage switching are indicated.

The switching time measured in Figure 6.5 is limited by the switching properties of the LC material, and the resolution of our measurement equipment. Closer analysis of the switching (Figure 6.7) reveals that several jumps between the maximum and minimum level can be distinguished in one switching event. This is probably due to fluctuations of the liquid crystal during reorientation. The VCSEL switches multiple times between the two polarization states during an interval of 100 µs. As shown in Figure 6.7, during the switching on (Figure 6.7a) or switching off (Figure 6.7b) interval, switching actually occurs in less than 10 µs (this is the resolution of our measurement equipment). The issue of repeated switching may be avoided by using optimized nematic mixtures or other types of liquid crystals such as dual frequency LC [93] or nano-pore polymerized LCs [94]. We believe that the switching time of this device can be much faster (below microsecond), because intrinsic laser switching can happen in the order of nanoseconds.

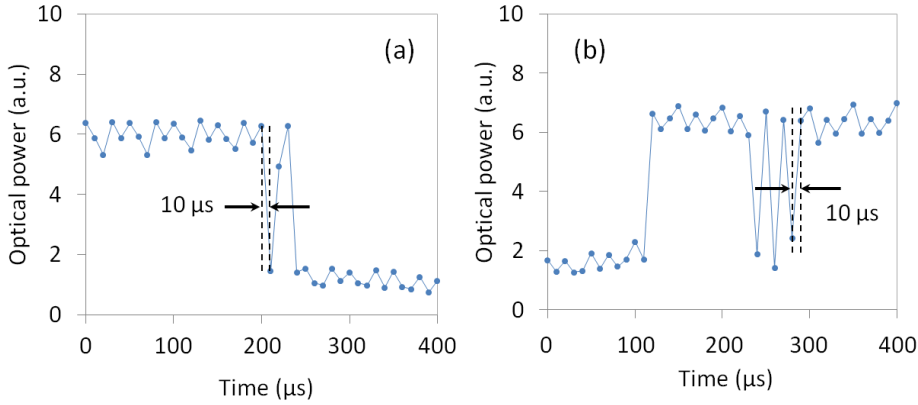

Figure 6.7: Measured optical power P_y emission as a function of time. The sampling rate is 100 kHz. (a) Switch off. (b) Switch on.

6.3.2 Threshold

The threshold current as a function of the applied voltage over the LC layer is shown in Figure 6.8. Similar to the periodic polarization switching, the threshold current exhibits local maxima around 1 V, 1.5 V and 2.6 V. The simulated threshold gain for the two polarization modes is shown in Figure 6.9. As explained in section 6.2, the lasing threshold for mode P_x changes periodically with the voltage applied over the LC layer, while the threshold for mode P_y remains the same. At the moment that the lasing threshold for mode P_x becomes larger than for mode P_y, the polarization switches from mode P_x to mode P_y (shown in Figure 6.3), and the threshold current reaches a local maximum (Figure 6.8). This phenomenon repeats three times in the applied voltage range, which confirms that the measurement results match well with the theoretical analysis.

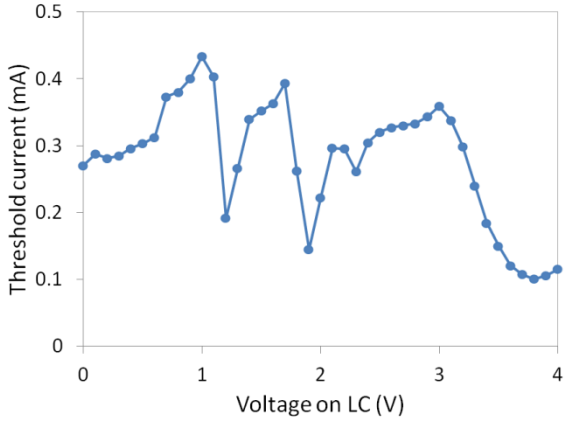

Figure 6.8: Measured threshold current as a function of the applied voltages over the LC layer.

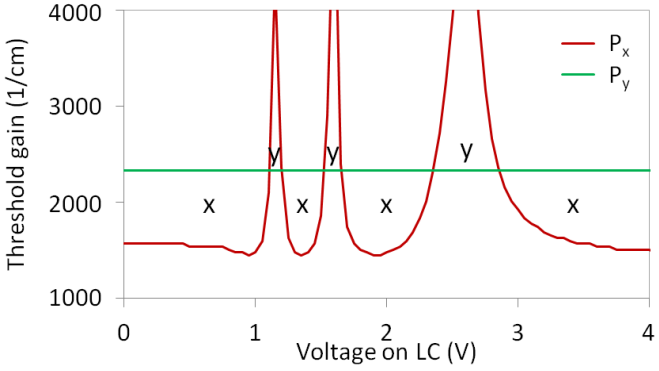

Figure 6.9: The simulated threshold gain (red line for P_x mode; green line for P_y mode), as a function of the voltage applied over the LC layer.

6.3.3 Emission wavelength

The emission wavelength of the two polarization modes (P_x and P_y) as a function of the voltage over the LC is shown in Figure 6.10. It is observed that the emission wavelength of polarization P_x continuously decreases over 0.5 nm with increasing voltage and that after the switch to P_y the lasing wavelength is about 1 nm smaller. This switch to P_y is observed in the intervals 1~1.1 V, 1.5~1.8 V or 2.2~2.6 V. Compared to the polarization measurement in Figure 6.3, there is a small mismatch of the voltage range where the switches happen, which is due the fact that the measurements are

not exactly reproduced at different times. Compared to the measurement results of threshold current shown in Figure 6.8, it is observed that the threshold current reaches a local maximum at the voltage values where the polarization switches to P_y mode.

The measurements of wavelength agree well with the simulation of the emission wavelength which is presented in Figure 6.10. The simulated emission wavelength of P_x is modulated by the voltage applied over the LC layer, while the one of P_y does not change. The reason of this wavelength behavior is the same with that of the threshold gain behavior. Because the optical path length of P_x mode changes with the reorientation of LC molecules, the resonance wavelength is modulated as a result. But P_y mode is not influenced by the LC orientation, so its lasing wavelength remains constant.

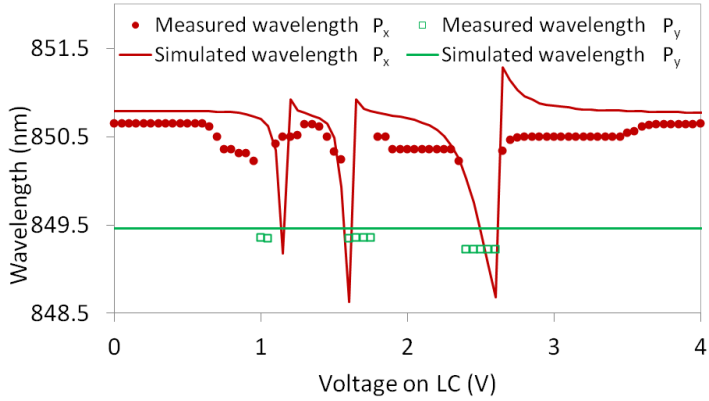

Figure 6.10: Measured emission wavelength (red dots for P_x; green squares for P_y) and simulated emission wavelength (red line for P_x; green line for P_y) as a function of the voltage amplitude over the LC layer. The VCSEL current is 1 mA, the frequency of the LC is 1 kHz.

Chapter 7

Conclusions and outlook

This work provides a better physical understanding of the combined VCSEL with LC system. A technology to integrate VCSELs in LC devices has been developed and the resulting devices have been characterized. The result is a laser that is driven with a current source, for which the emission properties (power, polarization, and wavelength) can be modulated by applying a voltage over the liquid crystal or by changing the temperature.

7.1 Achievements

7.1.1 VCSEL with nematic LC overlay

The electrically driven VCSEL is covered with a thin nematic LC layer that can be driven separately. The LC is aligned by photo-alignment. The LC layer strongly affects the polarization of the VCSEL emission due to its birefringent properties. The polarization state of the laser emission can be controlled by the applied voltage.

7.1.2 CLC-VCSEL

CLC is used to provide optical feedback to the VCSEL, because the circular polarization mode with the same handedness of CLC helix is effectively reflected due to the photonic band structure of the CLC. The emission is purely circularly polarized, with even higher polarization purity than the linear polarization of the stand-alone VCSEL. In addition, the threshold

current is decreased, the wavelength can be thermally tuned and the slope efficiency is increased.

7.1.3 VCSEL with an external metallic or dielectric mirror

The VCSEL device has an external cavity that is formed by an additional reflector, made by aluminum or a stack of dielectric layers, which can provide polarization-insensitive optical feedback. The external cavity length can be changed by temperature due to thermal deformation of the mechanical structure. The emission properties, including polarization state, transverse mode and longitudinal mode, can be tuned by changing the external cavity length. As a result, the emission of the device is thermally tunable.

7.1.4 LC-VCSEL

Nematic LC covered by a dielectric reflector (periodic bi-layers of SiO_2/Ta_2O_5) provides optical feedback to the VCSEL. The reflection band of the dielectric reflector is determined by the refractive indices of the materials and the thicknesses of the layers. In order to make effective optical feedback, the reflection band is suitably designed to include the emission wavelength of the VCSEL. By changing the voltage across the LC layer, the optical length of the external cavity can be tuned. As a result, the emitting properties of the LC-VCSEL can be controlled by the voltage applied on the LC layer. Stable and reproducible polarization switching between two orthogonal linear polarizations is realized in sub-millisecond time scales.

7.2 Outlook

This work has realized emission-controlled LC-VCSEL devices. But there are still areas in which further improvements could be obtained.

Firstly, the wavelength tuning of these devices is now in the order of a few nanometer. This might be further improved. One possible way is to fabricate a device based on a “half VCSEL”, which has only one DBR mirror (at the bottom), with nematic LC or CLC as top mirror. In this way, the reflection of the LC layer will be much more efficient and play a more important role in the modulation of the emission. Some theoretical analyses have been made on this LC + half VCSEL model and these indeed predict a much larger wavelength tuning range of tens of nanometer [76, 82]. We also made simulations of the emission wavelength for this LC-half-VCSEL tuned by

the voltage applied over the nematic LC layer. The result is shown in Figure 7.1. The simulation predicts a wavelength tuning range of more than 10 nm for an applied voltage of 5 V, which is much larger than the tuning range of a full VCSEL with a LC external cavity (LC-full-VCSEL) and a VCSEL with only a half of top DBR and a LC external reflector (LC-halftop-VCSEL).

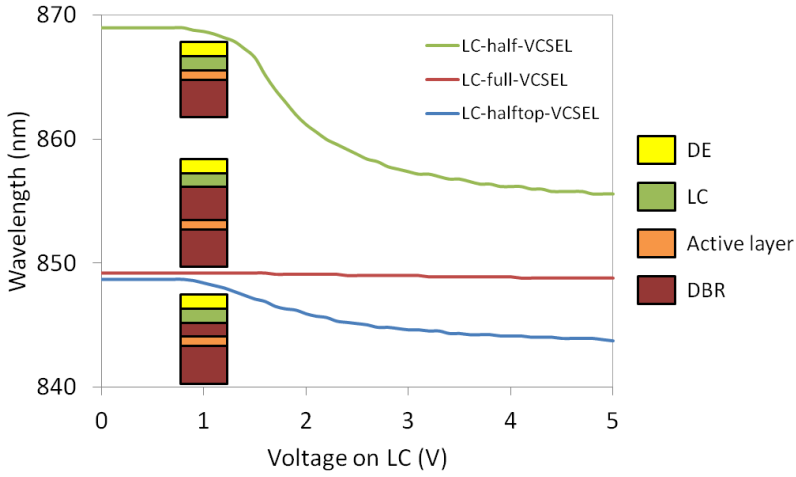

Figure 7.1: Simulated emission wavelength of a half VCSEL with a LC external cavity, as a function of the voltage applied over the LC layer. LC thickness is 1 µm. The simulations of a full VCSEL and a VCSEL with a half top DBR are also shown for comparison.

Furthermore, the nonlinear effect of light propagating in the LC can be studied using high output power VCSELs. The non-linearity refers to the fact that the liquid crystal director can reorient under influence of the electromagnetic field of the laser emission. The output optical power of currently used VCSEL is only about 0.5 mW. Commercial products with much higher output power (in the order of a few milliwatts) are available. This should be intense enough to influence the liquid crystal confuration. It would be interesting to investigate the laser properties for different LC orientations.

Appendix A

Stokes Parameters

In this appendix, the Stokes parameters are used to describe the state of polarization of an electro-magnetic wave. This approach is applied in this thesis for the representation of the polarization state of the emission from the VCSEL device.

The most convenient representation of polarized light uses a set of four parameters S_0, S_1, S_2 and S_3, introduced by Sir George Stokes in 1852. A good insight into the formalism is offered in [95]. The advantage to describe light polarization in this way is that it is linked to a measurement scheme. By measuring the light intensity transmitted from a linear polarizer and a quarter wave plate with proper azimuth angles, all the Stokes parameters can be determined.

The quantitative description of the polarization states is introduced in [96] and will be discussed below. Assume that light propagates in the z direction, the two electric field components can be assigned with a phase and amplitude such that

$$E_x = E_{x0}\sin(\omega t + \Phi_x)$$
$$E_y = E_{y0}\sin(\omega t + \Phi_y) \qquad \text{(A.1)}$$

where E_x and E_y are the components of the electric field along directions x and y, ω is the angular frequency, Φ is the phase of the electric field. E_{x0}, E_{y0}, Φ_x, and Φ_y are constants.

The coordinate system and electric field components are presented in Figure A.1(a). The field components vary in time and describe an ellipse. If the principle axes of the ellipse described by (E_x, E_y) are in directions making angles θ and $\theta+\pi/2$ with the direction x (Figure A.1(b)), the equations can be simplified as

$$E_\theta = E_0 \cos\beta \sin\omega t$$
$$E_{\theta+\frac{\pi}{2}} = E_0 \sin\beta \cos\omega t \qquad \text{(A.2)}$$

where β is the angle whose tangent is the ratio of the fields along the two principle axes of the ellipse traced by the end point of electric vector as shown in Figure A.1(c). The value of β is between - $\pi/2$ and $\pi/2$, and the sign of β is negative or positive according to whether the polarization is left-handed or right-handed.

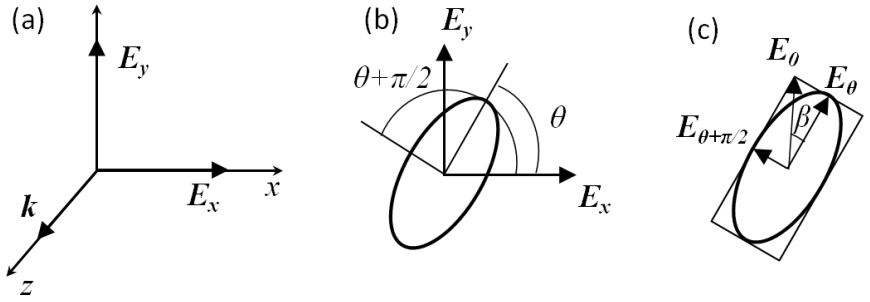

Figure A.1 : Plane wave propagating in the z direction. (a) Coordinate system. (b) Electric field components in x and y direction. (c) Ellipse traced by the end point of the electric field vector.

The intensity of the beam can be written as the square of the mean of the electric field vector E_0:

$$\hat{I} = E_0^2 = E_{x0}^2 + E_{y0}^2 = \hat{I}_x + \hat{I}_y \qquad \text{(A.3)}$$

The formulas connecting the representations of polarized light with four intensities S_0, S_1, S_2 and S_3 are important and can be combined in the following way. The expressions of electric fields components in x and y system can be described by the angles θ and β using the relations in Equation (A.2) :

$$E_x = E_0(\cos\beta \cos\theta \sin\omega t - \sin\beta \sin\theta \cos\omega t)$$
$$E_y = E_0(\cos\beta \sin\theta \sin\omega t + \sin\beta \cos\theta \cos\omega t) \qquad \text{(A.4)}$$

These equations can be reduced to the form of Equation (A.1) by letting

$$E_{x0} = E_0\sqrt{cos^2\beta cos^2\theta + sin^2\beta sin^2\theta}$$
$$E_{y0} = E_0\sqrt{cos^2\beta sin^2\theta + sin^2\beta cos^2\theta} \quad (A.5)$$

and

$$\tan\Phi_x = \tan\beta\tan\theta$$
$$\tan\Phi_y = -\tan\beta/\tan\theta \quad (A.6)$$

From the equations (A.3) to (A.6), we have the relations expressed as

$$S_0 = \hat{I} = E_0^2 = E_{x0}^2 + E_{y0}^2 = \hat{I}_x + \hat{I}_y$$
$$S_1 = E_{x0}^2 - E_{y0}^2 = \hat{I}_x - \hat{I}_y = \hat{I}\cos 2\beta\cos 2\theta$$
$$S_2 = 2E_{x0}E_{y0}\cos(\Phi_y - \Phi_x) = \hat{I}\cos 2\beta\sin 2\theta \quad (A.7)$$
$$S_3 = 2E_{x0}E_{y0}\sin(\Phi_y - \Phi_x) = \hat{I}\sin 2\beta$$

These are the Stokes parameters representing the polarization of an elliptically polarized beam. There is a relation in Equation (A.7) that

$$S_0^2 = S_1^2 + S_2^2 + S_3^2$$
$$\tan 2\theta = \frac{S_2}{S_1} \quad (A.8)$$
$$\sin 2\beta = \frac{S_3}{\sqrt{S_1^2 + S_2^2 + S_3^2}}$$

The meaning of Stokes parameters can be understood like this : S_1 represents the linear polarization along x or y direction, S_2 represents the linear polarization along 45˚ to x axis, S_3 represents the degree of circular polarization. So, the set of Stokes parameters (S_0, S_1, S_2, S_3) directly represent the polarization state of the light. (1, ±1, 0, 0) represents a pure linear polarization with polarization is along the x axis (+) or y axis (-). (1, 0, ±1, 0) represents a pure linear polarization which polarization is along 45˚

(+) or 135˚ (-) to the *x* axis. (1, 0, 0, ±1) represents pure right-handed (+) or pure left-handed (-) circular polarization.

The polarization discussed above is completely or fully polarized (Equation A.8 is satisfied). In reality, it is possible that the light is not completely polarized. Therefore, a more general description which can represent all real cases is needed. The Poincare sphere is a good approach for this purpose. All types of polarization states can be described as points on the sphere which is shown in Figure A.2. Complete polarization corresponds to a P vector that ends on the surface of the Poincare sphere. All other, partially polarized states can be described by a P vector ending inside the sphere.

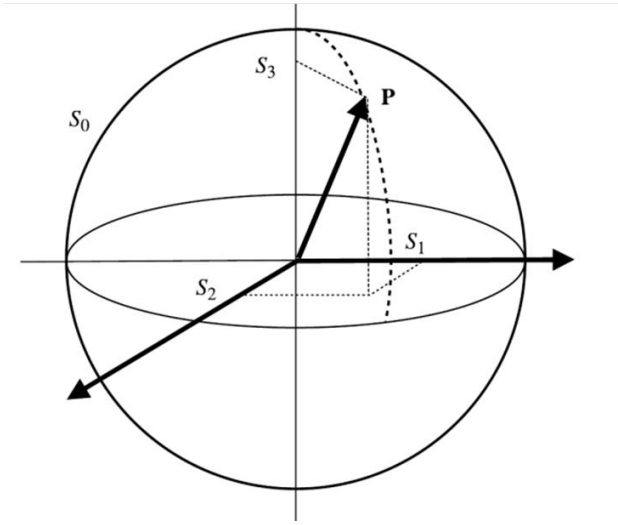

Figure A.2 : Poincare sphere representation of the polarization states of a monochromatic wave. A vector P represents a polarization state with a certain set of Stokes parameters. The radius of the sphere is S_0.

A new parameter *p* is defined for partially polarized light, called degree of polarization:

$$p = \frac{\sqrt{S_1^2+S_2^2+S_3^2}}{S_0} \qquad \text{(A.9)}$$

The degree of polarization *p* equals to one for fully polarized light, and it is less than one for partially polarized light.

Appendix B

Jones Matrix Formalism

Maxwell's equations are used to study the propagation of light waves in optical media. Because Maxwell's equations can only be handled analytically in special cases, such as plane waves in free space or in anisotropic media, numerical methods have been developed, based on different approximations or geometrical assumptions. The main idea of approximation approaches for monochromatic light propagation is to reduce the number of electromagnetic field variables. This is possible if the medium is assumed to be stratified and the light is assumed to be a plane wave. These two assumptions make the first-order Maxwell differential equations replaced by second-order differential equations. The aim then is to solve the equations taking into account the dielectric properties of the medium. Each layer of the stratified medium is characterized by a 2×2 matrix, which was first introduced by Jones [97-101]. The Jones matrix formalism is a conventional technique for calculating the optical properties of birefringent layered media for normal incidence. In this appendix this matrix method is studied and applied to our LC case, in which LC is treated as a stack of planar layers that have different refractive indices in each layer under an applied voltage.

Assume a plane wave travels along the *z*-direction, perpendicular to the *x*-*y* plane. This coordinate system is used to describe the polarization of the light by introducing a vector system with complex numbers that represent the

amplitude and phase of polarization components. The Jones vector is defined as

$$\boldsymbol{V} = \begin{bmatrix} V_x \\ V_y \end{bmatrix} = \begin{bmatrix} V_{x0} e^{i\varphi_x} \\ V_{y0} e^{i\varphi_y} \end{bmatrix} \tag{B.1}$$

The intensity is given as

$$I = \boldsymbol{V}\boldsymbol{V}^* = |V_x|^2 + \left|V_y\right|^2 \tag{B.2}$$

A polarization dependent device can be characterized by a 2×2 matrix $\boldsymbol{J}$. It is so called Jones matrix, which connects the incoming and outgoing wave in a vector description by

$$\boldsymbol{V}_{out} = \begin{bmatrix} J_{11} & J_{12} \\ J_{21} & J_{22} \end{bmatrix} \boldsymbol{V}_{in} \tag{B.3}$$

The elements of J are complex. The Jones matrix describes the linear transformation of the Jones vector of a plane wave by reflection, retardation, rotation, absorption, or transmission. If all the considered perturbations are assumed to be loss free, the resulting Jones matrices are unitary and take the form

$$\boldsymbol{J} = \begin{bmatrix} J_{11} & J_{12} \\ J_{21} & J_{22} \end{bmatrix} = \begin{bmatrix} A & -B^* \\ B & A^* \end{bmatrix} \; with \; |A|^2 + |B|^2 = 1 \tag{B.4}$$

The Jones matrix formalism can be applied in our research to investigate the light propagation in nematic LC thin layer, for example. The Jones matrix will be discussed for two cases: without and with voltage applied across the LC layer. Assume the LC molecules are originally planar aligned in the plane normal to the light propagation direction. If a voltage is applied perpendicular to this plane, LC molecules will reorient and till out of the plane.

If there is no voltage applied on, all directors of a planar LC layer are in the *x-y* plane and with an angle φ to the *x* axis (see Figure B.1a). In its local coordinate system (*x'y'z* coordinates), the Jones matrix for the LC layer can be written as

$$\boldsymbol{J} = \begin{bmatrix} e^{-i\frac{2\pi}{\lambda}n_e d} & 0 \\ 0 & e^{-i\frac{2\pi}{\lambda}n_o d} \end{bmatrix} = e^{-i\frac{\pi}{\lambda}(n_e+n_o)d} \begin{bmatrix} e^{-i\frac{\pi}{\lambda}\Delta n d} & 0 \\ 0 & e^{i\frac{\pi}{\lambda}\Delta n d} \end{bmatrix} \quad \text{(B.5)}$$

$$\Delta n = n_e - n_o$$

n_e and n_o are the extra-ordinary and ordinary refractive index, respectively. Δn is the birefringence of the material. d is the thickness of the LC layer.

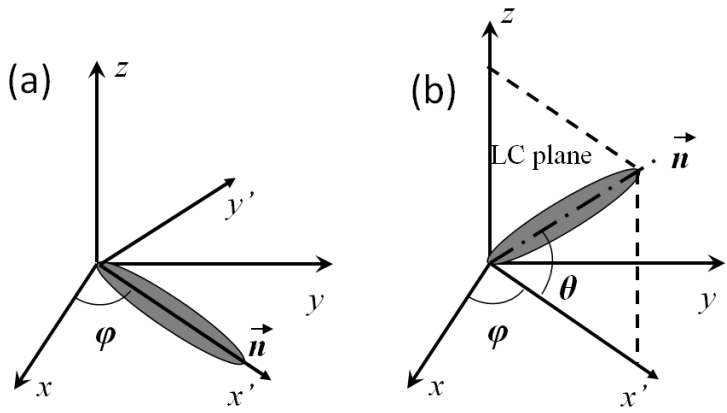

Figure B.1 : LC director in coordinate systems. (a) no voltage is applied; (b) voltage is applied over the LC layer, the LC director reorients in the LC plane (*x*'-*z* plane).

When a voltage is applied across the planar LC layer, the LC molecules will reorient within a plane (LC plane shown in Figure B.1b) according to the strength of the electric field. Therefore, the optical axes of the LC will be changed and the refractive indices in the coordinate system will change. The effective refractive index, instead of n_e, can be used to describe the index along the LC plane. The index perpendicular to the LC plane remains as n_o. So, the Jones matrix in the local coordinate system can be written as:

$$\boldsymbol{J} = e^{-i\frac{\pi}{\lambda}(n_e+n_o)d} \begin{bmatrix} e^{-i\frac{\pi}{\lambda}\int_0^d (n_{eff}(z)-n_o)dz} & 0 \\ 0 & e^{i\frac{\pi}{\lambda}\int_0^d (n_{eff}(z)-n_o)dz} \end{bmatrix} \quad \text{(B.6)}$$

with the effective refractive index $n_{eff}(z) = \frac{n_e n_o}{\sqrt{n_e^2 \sin^2\theta(z) + n_o^2 \cos^2\theta(z)}}$

$\theta(z)$ is the tilt angle of LC director indicated in Figure B.1b. It is a function of z and depends on the applied voltage which is demonstrated in Figure 1.8. When this matrix is applied to the laboratory coordinate system (xyz coordinates), transfer matrix should be used to rotate the azimuth angle φ. This is indeed the matrix described in Equation 1.9.

Bibliography

[1] G. E. Moore. (1965, April 19) Cramming More Components onto Integrated Circuits. *Electronics*. 114-117.

[2] B. E. Lemoff, M. E. Ali, G. Panotopoulos, G. M. Flower, B. Madhavan, A. F. J. Levi, *et al.*, "MAUI: Enabling fiber-to-the-processor with parallel multiwavelength optical interconnects," *J. Lightwave Technol.*, vol. 22, pp. 2043-2054, Sep 2004.

[3] H. Soda, K.-i. Iga, C. Kitahara, and Y. Suematsu, "GaInAsP/InP Surface Emitting Injection Lasers," *Jpn. J. Appl. Phys.*, vol. 18, pp. 2329-2330, 1979.

[4] F. Koyama, s. Kinoshita, and K.-i. Iga, "Room Temperature CW Operation of GaAs Vertical Cavity Surface Emitting Laser," *IEICE TRANSACTIONS* vol. E71, pp. 1089-1090, 1988.

[5] A. Scherer, J. Jewell, J. P. Harbison, K. Uomi, S. J. B. Yoo, R. J. Bhat, *et al.*, "Microfabrication of vertical-cavity surface-emitting laser cavities," in *Proceedings of SPIE*, 1994.

[6] C. Levallois, B. Caillaud, J. L. D. de la Tocnaye, L. Dupont, A. Le Corre, H. Folliot, *et al.*, "Long-wavelength vertical-cavity surface-emitting laser using an electro-optic index modulator with 10 nm tuning range," *Appl. Phys. Lett.*, vol. 89, p. 011102, Jul 3 2006.

[7] T. Sakamoto, H. Tsuda, M. Hikita, T. Kagawa, K. Tateno, and C. Amano, "Optical interconnection using VCSELs and polymeric waveguide circuits," *J. Lightwave Technol.*, vol. 18, pp. 1487-1492, Nov 2000.

[8] J. Missinne, E. Bosman, B. Van Hoe, G. Van Steenberge, S. Kalathimekkad, P. Van Daele, *et al.*, "Flexible Shear Sensor Based on

Embedded Optoelectronic Components," *IEEE Photonic. Tech. L.*, vol. 23, pp. 771-773, Jun 15 2011.

[9] B. Van Hoe, D. Lamon, E. Bosman, G. Van Steenberge, J. Missinne, P. Goethals, *et al.*, "Embedded high resolution sensor based on optical feedback in a Vertical Cavity Surface Emitting Laser," *Smart Sensor Phenomena, Technology, Networks, and Systems 2010*, vol. 7648, 2010.

[10] G. Overton. (2013) VCSEL ILLUMINATION: High-power VCSELs rule IR illumination. *Laser Focus World*.

[11] http://www.compoundsemiconductor.net/.

[12] http://www.aopen.com/.

[13] http://www.lasercomponents.com/.

[14] https://www.eol.ucar.edu/content/atmospheric-profiling.

[15] http://www.myeos.org/node/3578.

[16] P. G. De Gennes and J. Prost. (1995). *The Physics of Liquid Crystals*.

[17] I. Dierking. (2003). *Textures of Liquid Crystals*.

[18] I. Khoo. (1994). *Liquid Crystals: Physical Properties and Nonlinear Optical Phenomena*.

[19] P. J. Collings. (1990). *Liquid Crystals: Nature's Delicate Phase of Matter (2 ed.)*.

[20] K. Iizuka. (2002). *Elements of Photonics*. *1*.

[21] P. Yeh and C. Gu. (1999). *Optics of Liquid Crystal Displays*.

[22] A. d'Alessandro and R. Asquini, "Liquid Crystal Devices for Photonic Switching Applications: State of the Art and Future Developments," *Mol. Cryst. Liq. Cryst.*, vol. 398, pp. 207-221, 2003.

[23] J. Beeckman, K. Neyts, and P. Vanbrabant, "Liquid-crystal photonic applications," *Opt. Eng.*, vol. 50, p. 081202, 2011.

[24] O. Castany and L. Dupont, "Liquid crystal micro-cells: collective fabrication of individual micro-cells," *J. Micromech. Microeng.*, vol. 20, Jun 2010.

[25] Y. P. Lan, C. Y. Chen, R. P. Pan, and C. L. Pan, "Fine-tuning of a diode laser wavelength with a liquid crystal intracavity element," *Opt. Eng.*, vol. 43, pp. 234-238, Jan 2004.

[26] A. R. Barron. (2012). *Physical Methods in Chemistry and Nano Science*.

[27] J. Stohr and M. G. Samant, "Liquid crystal alignment by rubbed polymer surfaces: a microscopic bond orientation model," *J. Electron Spectrosc.*, vol. 98, pp. 189-207, 1999.

[28] V. G. Chrigrinov, V. M. Kozenkov, and H. S. Kwok. (2008). *Photoalignment of Liquid Crystalline Materials-Physics and Applications.*

[29] K. Ichimura, "Photoalignment of Liquid-Crystal Systems," *Chem. Rev.*, vol. 100, pp. 1847-1873, 2000.

[30] B. Jerome, "Surface effects and anchoring in liquid crystals," *Rep. Prog. Phys.*, vol. 54, p. 391, 1991.

[31] K. Ichimura, *Polymers as Electrooptical and Photooptical Active Media*. Berlin: Springer, 1996.

[32] K. Ichimura, T. Seki, Y. Kawanishi, Y. Suzuki, M. Sakuragi, and T. Tamaki, *Photoreactive Materials for Ultrahigh-Density Optical Memory*. Amsterdam: Elsevier Science, 1994.

[33] K. Ichimura, Y. Suzuki, T. Seki, A. Hosoki, and K. Aoki, "Reversible change in alignment mode of nematic liquid crystals regulated photochemically by command surfaces modified with an azobenzene monolayer," *Langmuir*, vol. 4, pp. 1214-1216, 1988.

[34] K. Aoki, T. Seki, Y. Suzuki, T. Tamaki, A. Hosoki, and K. Ichimura, "Factors affecting photoinduced alignment regulation of cyclohexanecarboxylate-type nematic liquid crystals by azobenzene molecular films," *Langmuir*, vol. 8, pp. 1007-1013, 1992.

[35] K. Aoki, Y. Kawanishi, T. Seki, M. Sakuragi, T. Tamaki, and K. Ichimura, "REVERSIBLE ALIGNMENT CHANGE OF LIQUID-CRYSTALS INDUCED BY PHOTOCHROMIC MOLECULAR FILMS - PROPERTIES OF AZOBENZENE CHROMOPHORES COVALENTLY ATTACHED TO SILICA SURFACES " *Liq. Cryst.*, vol. 19, pp. 119-125, 1995.

[36] L. M. Blinov and V. G. Chrigrinov, *Electrooptic Effects in Liquid Crystal Materials*. New York: Springer, 1994.

[37] P. Yeh and C. Gu, Eds., *Optics of Liquid Crystal Displays*. John Wiley & Sons, 2010, p.^pp. Pages.

[38] V. I. Kopp, B. Fan, H. K. M. Vithana, and A. Z. Genack, "Low-threshold lasing at the edge of a photonic stop band in cholesteric liquid crystals," *Opt. Lett.*, vol. 23, pp. 1707-1709, 1998.

[39] L. Penninck, J. Beeckman, P. De visschere, and K. Neyts, "Numerical simulation of stimulated emission and lasing in dye doped cholesteric liquid crystal films," *J. Appl. Phys.*, vol. 113, p. 8, 2013.

[40] L. Penninck, J. Beeckman, P. D. Visschere, and K. Neyts, "Light emission from dye-doped cholesteric liquid crystals at oblique angles: Simulation and experiment," *Phys. Rev. E*, vol. 85, p. 041702, 2012.

[41] C. J. Chang-Hasnain, J. P. Harbison, L. T. Florez, and N. G. Stoffel, "Polarization characteristics of quantum well vertical cavity surface emitting lasers," *Electron. Lett.*, vol. 27, pp. 163–164, 1991.

[42] M. P. v. Exter, A. K. J. v. Doorn, and J. P.Woerdman, "Electrooptic effect and birefringence in semiconductor vertical-cavity lasers," *Phys. Rev. A*, vol. 56, pp. 845-853, 1997.

[43] A. K. Jansen van Doornen, M. P. van Exter, and J. P. Woerdman, "Elasto-optic anisotropy and polarization orientation of vertical-cavity surface-emitting semiconductor lasers," *Appl. Phys. Lett.*, vol. 69, pp. 1041-1043, 1996.

[44] C. L. Chua, R. L. Thornton, D. W. Treat, and R. M. Donaldson, "Anisotropic apertures for polarization-stable laterally oxidized vertical-cavity lasers " *Appl. Phys. Lett.*, vol. 73, p. 1631 1998.

[45] H. K. T. Yoshikawa, K. Kurihara, M. Kajita, Y. Sugimoto, K. Kasahara, "Complete polarization control of 8×8 vertical-cavity surface-emitting laser matrix arrays " *Appl. Phys. Lett.*, vol. 66, p. 908, 1995.

[46] W. Wanga, Y. Q. Ninga, Z. H. Tiana, X. Zhanga, J. J. Shia, Z. F. Wanga, *et al.*, "Coherent polarization stabilization in large-aperture rectangular post bottom-emitting vertical-cavity surface-emitting lasers," *Opt. Commun.*, vol. 284, pp. 1335–1338, 2011.

[47] Å. Haglund, J. S. Gustavsson, J. Bengtsson, P. Jedrasik, and A. Larsson, "Design and evaluation of fundamental-mode and polarization-stabilized VCSELs with a subwavelength surface grating," *IEEE J. Quantum Electron.*, vol. 42, pp. 231-240, 2006.

[48] S. J. Schablitsky, L. Zhuang, R. C. Shi, and S. Y. Chou, "Controlling polarization of vertical-cavity surface-emitting lasers using amorphous silicon subwavelength transmission gratings " *Appl. Phys. Lett.*, vol. 69, p. 7, 1996.

[49] J. H. Ser, Y. G. Ju, J. H. Shin, and Y. H. Lee, "Polarization stabilization of vertical-cavity top-surface-emitting lasers by

inscription of fine metal-interlaced gratings " *Appl. Phys. Lett.*, vol. 66, p. 2769 1995.

[50] M. A. Arteaga, M. López-Amo, H. Thienpont, and K. Panajotov, "Role of external cavity reflectivity for achieving polarization control and stabilization of vertical cavity surface emitting laser " *Appl. Phys. Lett.*, vol. 90, p. 031117 2007.

[51] D.-S. Song, Y.-J. Lee, H.-W. Choi, and Y.-H. Lee, "Polarization-controlled, single-transverse-mode, photonic-crystal, vertical-cavity, surface-emitting lasers " *Appl. Phys. Lett.*, vol. 82, p. 3182 2003.

[52] G. Verschaffelt, W. v. d. Vleuten, M. Creusen, E. Smalbrugge, T. G. v. d. Roer, F. Karouta, *et al.*, "Polarization Stabilization in Vertical-Cavity Surface-Emitting Lasers Through Asymmetric Current Injection," *IEEE Photonic. Tech. L.*, vol. 12, pp. 945-947, 2000.

[53] Y.-G. Ju, Y.-H. Lee, H.-K. Shin, and I. Kim, "Strong polarization selectivity in 780-nm vertical-cavity surface-emitting lasers grown on misoriented substrates " *Appl. Phys. Lett.*, vol. 71, p. 741 1997.

[54] H. Saito, K. Nishi, S. Sugou, and Y. Sugimoto, "Controlling polarization of quantum-dot surface-emitting lasers by using structurally anisotropic self-assembled quantum dots " *Appl. Phys. Lett.*, vol. 71, p. 590 1997.

[55] X. Hachair, G. Tissoni, H. Thienpont, and K. Panajotov, "Linearly polarized bistable localized structure in medium-size vertical-cavity surface-emitting lasers," *Phys. Rev. A*, vol. 79, p. 011801, 2009.

[56] K. Panajotov, "Polarization switching induced by phase change in extremely short external cavity vertical-cavity surface-emitting lasers " *Appl. Phys. Lett.*, vol. 84, pp. 2763-2765, 2004.

[57] T. H. Russell and T. D. Milster, "Polarization switching control in vertical-cavity surface-emitting lasers " *Appl. Phys. Lett.*, vol. 70, pp. 2520-2522, 1997.

[58] A. Valle, L. Pesquera, and K. A. Shore, "Polarization Selection and Sensitivity of External Cavity Vertical-Cavity Surface-Emitting Laser Diodes," *IEEE Photonic. Tech. L.*, vol. 10, pp. 639-641, 1998.

[59] C. I. Wilkinson, J. Woodhead, J. E. F. Frost, J. S. Roberts, R. Wilson, and M. F. Lewis, "Electrical polarization control of vertical-cavity surface-emitting lasers using polarized feedback and a liquid crystal," *IEEE Photonic. Tech. L.*, vol. 11, pp. 155-157, Feb 1999.

[60] A. V. Barve, Y. Zheng, L. A. Johansson, A. Mehta, A. Husain, and L. A. Coldren, "Fast, electrically controlled polarization modulation of

multimode vertical-cavity surface-emitting lasers by RF frequency modulation," *Opt. Express*, vol. 21, pp. 31092-31097, 2013.

[61] P. Perez, A. Valle, L. Pesquera, and A. Quirce, "All-Optical Inverter Based on Polarization Switching in VCSELs Subject to Single and Dual Optical Injection " *IEEE J. Selected topics in Quant. Electr.*, vol. 19, p. 1700408 2013.

[62] A. A. Qader, Y. Hong, and K. A. Shore, "Robust Irreversible Polarization Switching in Optically Injected VCSELs " *IEEE Photonic. Tech. L.*, vol. 25, pp. 1173-1176 2013.

[63] Q. Wang, B. Guan, K. Liu, X. Liu, X. Jiang, Y. Ma, *et al.*, "Temperature dependent polarization switch of 850-nm VCSELs with different apertures," *Opt. Laser Technol.*, vol. 63, pp. 19-23 2014.

[64] C. Degen, I. Fischer, and W. Elsaber, "Transverse modes in oxide confined VCSELs: Influence of pump profile, spatial hole burning, and thermal effects," *Opt. Express*, vol. 5, pp. 38-47, 1999.

[65] Y. G. Zhao and J. G. McInerney, "Transverse-Mode Control of Vertical-Cavity Surface-Emitting Lasers," *IEEE J. Quantum Electron.*, vol. 32, pp. 1950-1958, 1996.

[66] J. Dellunde, A. Valle, and K. A. Shore, "Transverse mode selection in external cavity vertical cavity surface emitting laser diodes," *J. Opt. Soc. Amer., B*, vol. 13, pp. 2477-2783, 1996.

[67] O. Castany, "Tunable semiconductor vertical-cavity surface-emitting laser with an intracavity liquid crystal layer," *Appl. Phys. Lett.*, vol. 98, p. 161105, 2011.

[68] T. Gruendl, K. Zogal, P. Debernardi, C. Gierl, C. Grasse, K. Geiger, *et al.*, "50 nm continuously tunable MEMS VCSEL devices with surface micromachining operating at 1.95 mu m emission wavelength " *Semicond. Sci. Tech.*, vol. 28, p. 012001 2013.

[69] M. C. Larson and J. S. Harris, "Wide and continuous wavelength tuning in a vertical-cavity surface-emitting laser using a micromachined deformable-membrane mirror " *Appl. Phys. Lett.*, vol. 68, p. 891 1996.

[70] M. Maute, E. Riemenschneider, G. Bohm, H. Halbritter, M. Ortsiefer, R. Shau, *et al.*, "Micro-mechanically tunable long wavelength VCSEL with buried tunnel junction " *Electron. Lett.*, vol. 40, pp. 430-431 2004.

[71] M. Nakahama, H. Sano, N. Nakata, A. Matsutani, and F. Koyama, "Electro-thermal tuning of MEMS VCSEL with giant wavelength-temperature dependence " *IEICE Electron. Expr.*, vol. 9, 2012.

[72] C. Gierl, T. Gruendl, S. Paul, K. Zogal, M. T. Haidar, P. Meissner, *et al.*, "Temperature characteristics of surface micromachined MEMS-VCSEL with large tuning range " *Opt. Express*, vol. 22, pp. 13063-13072, 2014.

[73] T. Yano, H. Saitou, N. Kanbara, R. Noda, S. Tezuka, N. Fujimura, *et al.*, "Wavelength Modulation Over 500 kHz of Micromechanically Tunable InP-Based VCSELs With Si-MEMS Technology," *IEEE J. Selected topics in Quant. Electr.*, vol. 15, pp. 528-534, 2009.

[74] M. Maute, B. Kogel, G. Bohm, P. Meissner, and M. Amann, "MEMS-tunable 1.55-mu m VCSEL with extended tuning range incorporating a buried tunnel junction," *IEEE Photonic. Tech. L.*, vol. 18, pp. 688-690, 2006.

[75] Y. Xie, J. Beeckman, W. Woestenborghs, K. Panajotov, and K. Neyts, "VCSEL with photo-aligned liquid crystal overlay," *IEEE Photonic. Tech. L.*, vol. 24, pp. 1509-12, 1 Sept. 2012.

[76] K. Panajotov, Y. Xie, M. Dems, C. Belmonte, H. Thienpont, J. beeckman, *et al.*, "Vertical-cavity surface-emitting laser emitting circularly polarized light," *Laser Phys. Lett.*, vol. 10, p. 105003, 2013.

[77] Y. Xie, J. Beeckman, K. Panajotov, and K. Neyts, "Vertical-cavity surface-emitting laser with a chiral nematic liquid crystal overlay," *IEEE Photonic. J.*, vol. 6, p. 1500010, 2014.

[78] Y. Xie, J. Beeckman, K. Panajotov, and K. Neyts, "Vertical-cavity surface-emitting laser with a liquid crystal external cavity," *Opt. Lett.*, vol. 39, pp. 6494-6497, 2014.

[79] W. Lukosz, "Theory of optical-environment-dependent spontaneous-emission rates for emitters in thin-layers," *phys. Rev. B*, vol. 22, pp. 3030-3038, 1980.

[80] L. Penninck, P. De visschere, J. Beeckman, and K. Neyts, "Dipole radiation within one-dimensional anisotropic microcavities: a simulation method," *Opt. Express*, vol. 19, pp. 18558-18576 2011.

[81] D. Y. K. Ko and J. R. Sambles, "Scattering matrix-method for propagation of radiation in stratified media - attenuated total reflection studies of liquid-crystals," *J. Opt. Soc. Amer. A, Optics image science and Vision*, vol. 5, pp. 1863-1866, 1988.

[82] K. Panajotov and H. Thienpont, "Vertical-cavity surface-emitting laser with liquid crystal overlay," *Opt. Express*, vol. 19, p. 16749, 2011.

[83] K. Panajotov, B. Nagler, G. Verschaffelt, A. Georgievski, H. Thienpont, J. Danckaert, *et al.*, "Impact of in-plane anisotropic strain on the polarization behavior of vertical-cavity surface-emitting lasers," *Appl. Phys. Lett.*, vol. 77, pp. 1590-1592, 2000.

[84] T. Kihara, "Measurement method of Stokes parameters using a quarter-wave plate with phase difference errors," *Appl. Optics*, vol. 50, pp. 2582-2587, Jun 10 2011.

[85] R. James, G. Stojmenovik, C. Desimpel, S. Vermael, F. A. Fernandez, S. E. Day, *et al.*, "Influence of Ion Transport on Liquid Crystal Switching," *J. Disp. Technol.*, vol. 2, pp. 237-246, Sep 2006.

[86] J. Li, S. T. Wu, S. Brugioni, R. Meucci, and S. Faetti, "Infrared refractive indices of liquid crystals," *J. Appl. Phys.*, vol. 97, Apr 1 2005.

[87] O. Svelto and D. C. Hanna, *Principles of lasers*, 4 ed. United State of America: Springer, 1998.

[88] T. Scharf, *Polarized light in liquid crystals and polymers*. United State of America: Wiley Interscience, 2007.

[89] W. Nakwaski, "Thermal aspects of efficient operation of vertical-cavity surface-emitting lasers," *Opt. Quant. Electron.*, vol. 28, pp. 335-352, 1996.

[90] V. Jayaraman, T. J. Goodnough, T. L. Beam, F. M. Ahedo, and R. A. Maurice, "Continuous-Wave Operation of Single-Transverse-Mode 1310-nm VCSELs up to 115 C," *IEEE Photonic. Tech. L.*, vol. 12, pp. 1595-1597, 2000.

[91] Y. Ohiso, H. Okamoto, R. Iga, K. Kishi, and C. Amano, "Single Transverse Mode Operation of 1.55-μm Buried Heterostructure Vertical-Cavity Surface-Emitting Lasers," *IEEE Photonic. Tech. L.*, vol. 14, pp. 738-740, 2002.

[92] K. Panajotov, B. Ryvkin, J. Danckaert, M. Peeters, H. Thienpont, and I. Veretennicoff, "Polarization switching in VCSEL's due to thermal lensing," *IEEE Photonic. Tech. L.*, vol. 10, pp. 6-8, 1998.

[93] A. B. Golovin, S. V. Shiyanovskii, and O. D. Lavrentovich, "Fast switching dual-frequency liquid crystal optical retarder, driven by an amplitude and frequency modulated voltage," *Appl. Phys. Lett.*, vol. 83, p. 3864 2003.

[94] M. Mohammadimasoudi, J. Beeckman, J. Shin, K. Lee, and K. Neyts, "Widely tunable chiral nematic liquid crystal optical filter with microsecond switching time," *Opt. Express*, vol. 22, pp. 19098-19107, 2014.

[95] D. Goldstein. (2003). *Polarized Light*.

[96] S. Chandrasekhar. (1960). *Radiative Transfer*.

[97] R. C. Jones, "A new calculus for the treatment of optical systems I-III," *J. Opt. Soc. Amer.*, vol. 31, pp. 488-503, 1941.

[98] R. C. Jones, "A new calculus for the treatment of optical systems IV," *J. Opt. Soc. Amer.*, vol. 32, pp. 486-493, 1942.

[99] R. C. Jones, "A new calculus for the treatment of optical systems V-VI," *J. Opt. Soc. Amer.*, vol. 37, pp. 107-112, 1947.

[100] R. C. Jones, "A new calculus for the treatment of optical systems VII," *J. Opt. Soc. Amer.*, vol. 38, pp. 671-685, 1948.

[101] R. C. Jones, "A new calculus for the treatment of optical systems VIII," *J. Opt. Soc. Amer.*, vol. 46, pp. 126-131, 1956.